Monte Carlo Simulations of Spin Transport in Semiconductor Devices

Prifysgol Abertawe
Swansea University

College of Science

Department of Physics
Swansea University

This dissertation is submitted for the degree of
PhD

Benjamin Thorpe

August 3, 2018

Dedication

I would like to dedicate this thesis to my loving parents

Declaration

This thesis is the result of my own investigations, except where otherwise stated. Other sources are acknowledged by footnotes giving explicit references and a bibliography is appended. This work has not previously been accepted in substance for any degree and is not being concurrently submitted in candidature for any degree and I hereby give consent for my thesis, if accepted, to be available for photocopying and for inter-library loan, and for the title and summary to be made available to outside organisations.

Signed ..... (candidate)

Date .....

Acknowledgements

I would like to acknowledge and thank my supervisors Sophie Schirmer and Karol Kalna along with Frank Langbien from Cardiff University for all their help and support to enable me to complete this PhD thesis. I also want to acknowledge the Sêr Cymru National Research Network for Advanced Engineering and Materials for providing funding in enable my research.

Abstract

In recent years the search for ever smaller and more power efficient electronics has made it necessary to embrace the quantum nature of electrons. Spintronics is a relatively new branch of engineering which hopes to capitalise on spin as a useful quantum property of electrons to work in tandem with (or potentially replace) electrostatic charge in the operation of nanoscale semiconductor devices.

This work focuses on the simulation of a promising new type of device known as the spin field effect transistor (spin-FET) [1, 2, 3]. These devices are similar in structure and function to more conventional Metal-Oxide Field Effect Transistors (MOSFET). The crucial difference, however, is the use of the electron spin either alongside or instead of charge transport, with the ultimate aim of improving both the bandwidth and power efficiency when compared with conventional devices.

To this end, we have modified an advanced ensemble Monte Carlo device simulator to include the spin as a separate degree of freedom of the electrons by using a Bloch equation model, with a spin-orbit interaction Hamiltonian to account for Dresselhaus and Rashba couplings. We then simulated electron spin transport in a realistic 25 nm gate length $In_{0.7}Ga_{0.3}As$ MOSFET and finally analysed how the spin transport was affected by the gate voltage, the source-drain voltage, lattice temperature, compressive strain and channel length.

Contents

List of Figures

List of Tables

1 Introduction

1.1 Motivation

It is well known to most students of both physics and many areas of engineering that all elementary particles possess an intriguing purely quantum mechanical property known as spin. It is an observable quantity with no classical analogue that is associated with the angular momentum of a particle as it rotates about its axis. Being a quantum phenomenon however this mental picture only explains half the story as it cannot account for the fact that the spin only takes on discrete values (i.e. its quantised) or that many particles (including electrons) are considered as point sources and as such have no radius to rotate around. However, we will leave the peculiar quantum nature of the spin to textbooks. [10, 11, 12].

Spin, however, as an observable (which in principle can be easily measured) has gained considerable interest in recent years with the advent of Spintronics, a relatively new branch of engineering which hopes to capitalise on spin as a useful property of electrons to work in tandem with (or potentially replace) electrostatic charge in the operation of nanoscale semiconductor devices. Indeed much has already been achieved in this area with spin properties such as; Tunnel magnetoresistance, being commonly used in high-speed computer memory and giant magnetoresistance, being the basis of operation for all magnetic hard drives.

Recently, however, attention has turned to a new type of device known as the spin field effect transistor (spin-FET) which are among the most promising spin-based semiconductor devices and are considered a future candidate for high-performance digital computing with ultra-low energy needs. [1, 2, 3]. These devices are similar in structure and function to more conventional Metal-Oxide Field Effect Transistors (MOSFET) and High Electron Mobility Transistors (HEMT) but with the crucial difference being the use of electron spin either alongside or instead of charge transport as part of the device operation.

In the past drift-diffusion models have been invaluable tools to investigate SpinFET devices [13]. However, these kinds of simulation are not useful for more complex device architectures commonly found in transistors (doping, heterostructures, gates etc.) and as such cannot give us an accurate picture as to the behaviour of spins in a nanoscale device under realistic working conditions.

To this end, we have applied finite-element quantum-corrected ensemble Monte Carlo simulations [7, 14] to an InGaAs field effect transistor to investigate spin and charge transport

with realistic device geometries, doping profiles, bandstructure and scattering and a self-consistent Poisson solver to solve for the electric field at each point on a grid across the device structure. This simulator, which has been experimentally verified was adapted to include the electron spin as a separate degree of freedom using a density matrix approach, the method for which is detailed in Section 5. The simulator was used to investigate gate and drain voltage dependence on spin transport (see Chapter 5), including the discovery of polarization recovery effects reminiscent of magnetization refocussing [15].

The simulator was then augmented to investigate the effect of material strain on spin transport by incorporating the effect of strain on the band energies and effective masses and spin-orbit coupling parameters (see Chapter 6). The results suggest that the device could operate as a room-temperature nanoscale strain sensor [15] Finally, the effect of temperature and device geometry are studied with a view to help optimise the channel and gate length and determine the best operating temperatures (see Chapters 6 and 7).

This approach while not entirely original [16, 17, 18] builds significantly on previous works in that we use the Poisson equation to solve for the electric field at each point in the device structure. This adds significantly to both the computation time and complexity compared to previous works, which make use of a constant electric field across the entire channel. However, our approach is generally considered to be a more realistic and robust way of simulating complicated structures found inside real transistors and we appear to see interesting effects (e.g. spin recovery) which have not been reported previously.

To put the work in this thesis into context, we present a brief overview of various proposed spinFET designs as well as the challenges associated with them, before we delve into the details on theoretical foundations of the simulator in Chapters 2-4 and present the results in Chapters 5-7.

1.2 Spin Transistors

1.2.1 The Datta-Dass Transistor

Datta and Das proposed the first true SPINFET in 1990 [1]. Their original design involved the use of an InAlAs/InGaAs quantum well to create a 2-dimensional electron gas (2DEG) that would be used as the channel for a transistor with a gate contact above and ferromagnetic source/drain contacts at either end (see Fig 1). The source would inject spin polarised

carriers into the channel while the drain would act as a spin detector by preferentially allowing the transmission of spins whose magnetic moment aligns with that of the drain.

This injection and detection were assumed to be 100% efficient for the sake of simplicity. Thus, the source injects only electrons with magnetic moments parallel to the field of the contact (with no spin flips occurring due to scattering at the interface), and the drain only transmits elections with magnetic moments parallel to the electric field of the contact (thus acting as a perfect spin filter).

Using a simple ballistic transport model, they argued that a voltage applied to the gate electrode would result in coherent rotation of the spins due to Rashba spin-orbit coupling as they pass through the electric field produced by the gate thus the source-drain current in this FET-like structure could be modulated by varying the voltage applied.

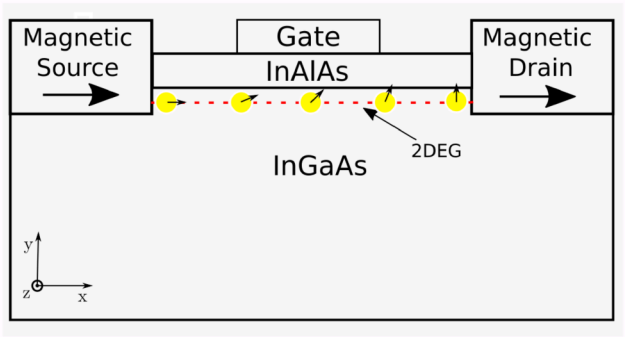

Figure 1: Schematic for Datta-Das Spin-FET. The yellow circles represent electrons flowing down the 2D channel formed by the quantum well at the InAlAs/InGaAs interface whilst the black arrows point in the direction of the magnetisation.

However, the gate control of spin transport along the channel was soon recognised as the major challenge, and a striped-channel high electron mobility transistor (HEMT) design with a quasi-1D channel was proposed by Bournel et al. [18]. Using ensemble Monte Carlo calculations, the electron transport was simulated for an InGaAs quantum well, and it was demonstrated that reducing the width of the 2D channel helped to minimise spin dephasing [17, 19, 20]. This is because for a 2DEG in the $x-z$ plane the spin precession Ω_R vector is given by [20]:

$$\Omega_R = \frac{2\alpha_{46}E_y}{\hbar}(-k_z u_x + k_x u_z) \tag{1}$$

where: α_{46} is the material dependent Rashba constant, E_y is the electric field due to the gate and $u_{x,z}$ is a unitary vector along $x(z)$ axis, with $\boldsymbol{k} = k_x u_x + k_z u_z$. Thus if the electrons have freedom in both the x and z directions the scattering will randomise the direction of Ω_R (due

to its dependence on $\boldsymbol{k}$) as the spin orientation of each electron becomes progressively less coherent (for more information see Section 2.4.2 on the D'yakonov-Perel mechanism). This effect, however, can be reduced by decreasing the channel width in the z-plane (resulting in a so-called quantum wire) thus, in turn, reducing the magnitude of the wave vector component k_z.

This design, however, can create a significant drawback. As noted by Bandyopadhyay and Cahay[21] while a quantum wire does reduce the spin scatting compared with a quantum well it also reduces the maximum conductance down to $e^2/\hbar$ per spin according to the Landauer formulae[22]. Whereas for a quantum well this would be $Ne^2/\hbar$ where N is the number of transverse sub-bands in the well. Thus, designs based on quantum wells could still be used for applications where gain or bandwidth are more critical than leakage current due to spin scattering.

The next big step in the design process came independently from both Schliemann et al. [13] and Cartoixà et al [23] who both extended the Datta-Das design to include spin-orbit coupling due to bulk inversion asymmetry (so-called Dresselhaus coupling) with the intention of creating an alternative SPINFET based on Rashba and Dresselhaus "tuning" (see Section 1.2.2 for more details). The coupling was included via an additional term to the Hamiltonian $H_D = \beta(k_x\sigma_x - k_y\sigma_y)$ where β is a material dependent parameter.

The Dresselhaus coupling was then included in the Datta-Dass design by MinShen et al. [16] who used ensemble Monte Carlo simulations to predict spin coherence and transconductance effects in the 2D quantum confined channel of a heterostructure III-V HEMT assuming one sub-band approximation [16]. However, the simulations were not self-consistently coupled with the Poisson equation. Thus the results are valid only at low applied electric field [16].

The Datta-Dass transistor also has a major limitation, the spin injection/detection efficiency, a problem which the majority of work in the last decade has been devoted to solving.

1.2.2 Datta-Das alternatives

Over the last decade, there have been several attempts to modify (and even replace entirely) the Datta-Das design to overcome some of the difficulties in its practical implementation. These have ranged from simple modifications to account for materials with different spin properties to devices which achieve the same objective but have a vastly different mode of

operation. This section will cover the notable work in this area.

Dresselhaus Tuned Devices - The Non-Ballistic SPINFET: As mentioned in Section 1.2.1 both Schliemann et al. [13] and Cartoixà et al. [23] suggested the use of Rashba tuning as a method of improving the Datta-Das design. The basic premise of this device is to tune the Rashba interaction via the use of a gate such that it has the same strength as the Dresselhaus interaction which is independent of the applied gate voltage and depends only on the material of the channel. In this configuration, the spin-orbit coupling loses its wave vector dependence, and thus momentum scatting will not change the Bloch vector as the electrons travel down the channel.

A transistor-like action can be achieved by simply injecting spin polarised carriers at the source if the Dresselhaus and Rashba interactions are balanced, then the polarisation of the current at the drain will be the same as that injected at the source. However, if we then de-tune the interaction, the polarisation will decrease to zero as the spins relax in the channel leading to no polarisation being detected at the drain. This design does come with a significant caveat however in that the minimum (off) current for such a device would be half of the maximum (on) current [21] making such devices unsuitable for low energy applications. This was further compounded by simulation data by Safir et al. [24] which suggested that the on-off conductance ratio would only be around 15-20% for a real device.

Dresselhaus split gate designs: Bandyopadhyay and Cahay proposed another alternative design to the Datta-Das Transistor in 2004 [4]. This was an alteration that would make use of the Dresselhaus interaction instead of Rashba via the use of a spilt top gate. The basic device consisted of a 1-dimensional channel between a ferromagnetic source and drain contact into which polarised spins were injected in the same manner as the original Datta-Das device. The main difference, however, was that the gate was split into two independent halves as shown in Figure 2.

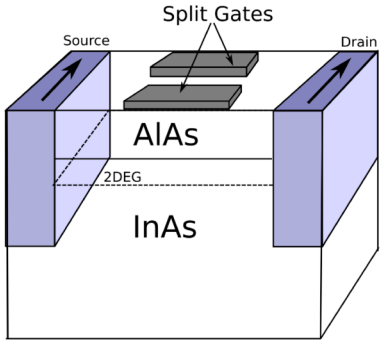

Figure 2: Schematic of Spin-FET proposed by [4] based on Dresselhaus interaction.

Assuming the potential profile in the y-direction is a square well grown in the [110] direction and the potential profile in the z-direction is parabolic (since confinement in this direction is enforced by split gates the curvature of which (ω) can be tuned by varying the applied voltage on the split gates).

Since the channel is strictly 1D (it was assumed that only the lowest sub-band was occupied) and the quantum well is symmetric, there is no Rashba interaction in the absence of a channel magnetic field [4, 10]. However, spin relaxation will still occur due to the pseudo-magnetic field created by the Dresselhaus interaction, the strength of which depends on the channel width in the z-direction $W_z = \sqrt{\frac{\hbar}{2m^*\omega}}$ which can be controlled via the applied voltage on the split gates.

Thus the electron spins precess around this field as they move along the channel and the precession angle ϕ is given by [10]

$$\phi = \frac{4m^*\alpha_{42}L}{\hbar^2}\left[\frac{m^*\omega}{2\hbar} - \left(\frac{\pi}{W_y}\right)^2\right] \tag{2}$$

where L is the channel length, α_{42} is a material dependent parameter associated with the strength of the Dresselhaus interaction, and W_y is the channel width in the y-direction.

Therefore, the amount of rotation can be controlled by the voltage applied to the split gates and thus transistor action similar to that of the original Datta-Dass design can be realised (i.e. the channel conductance will change depending on the direction of the spin current when compared to the field of the ferromagnetic drain).

The Spin Hall Transistor: Another alternative to the Datta-Das design proposed by Wunderlich et Al. in 2010 [6] the device is based on a phenomenon known as the Spin

Injection Hall Effect. If we take a solid subjected to a magnetic field B in the $+z$ direction and we apply an electric field E in the x direction, electrons will flow with a velocity v_{drift} in the direction of the electric field (see Figure 3). However, the presence of the magnetic field will mean that the electrons will also experience a Lorentz force in the $+y$ direction given by $ev_{drift}B_z$. This means that if we take a thin slice of material with thickness L in the y direction a detectable voltage will be generated between the surfaces at $y = L$ and $y = 0$ due to the charge imbalance created by the magnetic field, this effect was first observed in 1879 and is known as the Hall effect [25].

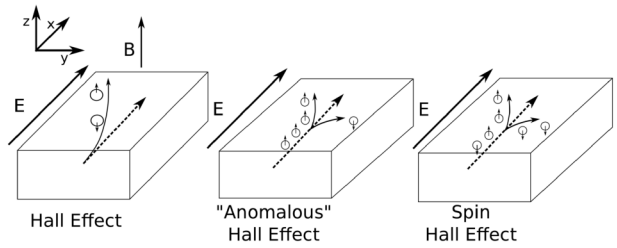

Figure 3: Diagram to show: Hall Effect (left), Anomalous Hall Effect (centre) and spin Hall effect (right).

If we now consider a ferromagnetic material a similar effect can also be observed without an external magnetic field, this is known as the anomalous Hall effect [26]. This voltage arises because the bandstructure and scattering events are spin dependent, thus if an electron has its spin polarised in the $+z$ direction it will be scattered in $+y$ direction, while electrons with spin polarised in the $-z$ will scatter in the $-y$ direction. Since the material is ferromagnetic there is an imbalance in the populations of spins thus more electrons will be scattered in one direction compared to the other leading to the creation of a charge imbalance without any applied magnetic field.

The spin Hall effect is a logical extension of this principle that was first proposed by Hirsch in 1999 [27]. The idea is that the direction of the spin influences the motion of the electrons perpendicular to an applied field. Thus we should see electrons with opposing spins travel in opposite directions perpendicular to the current flow, and for a non-magnetic material, we should observe a spin splitting in the direction perpendicular to the current flow. This is known as the spin Hall effect and has been experimentally demonstrated in a 2 µm thick InGaAs film [28] and an AlGaAs 2DEG [29].

It was then demonstrated by Wunderlich et al. [5] that the spin Hall effect could be used as a means to detect spin polarised current in a semiconductor. This was achieved by taking

voltage measurements transverse to the direction of current flowing through a 2DEG channel. If the current is polarised, a Hall voltage will be detected due to the charge imbalance created by the spin polarisation (with the magnitude of the voltage being dependant on the degree of polarisation). They then went on to experimentally demonstrate this effect in a planar two dimensional electron-hole gas (2DEG–2DHG) photo-diode consisting of a p-n junction, the p-side of which is formed by 2 vertically stacked AlGaAs/GaAs heterojunctions (with p-type doping at the top and n-type doping at the bottom) separated by a 90 nm layer of intrinsic GaAs (see Figure 4).

This allows the formation of a 2-dimensional hole gas (2DHG) at the p-type heterojunction. For the *n*-side the *p*-type top layer is removed and thus a 2DEG forms at the n-type heterojunction. This device is non-conductive in the dark at zero or reverse bias, owing to charge depletion of the p–n junction. However, it becomes conductive when irradiated with light of sufficient wavelength to allow the electrons (or holes) to overcome the potential barrier. By using circularly polarised light a spin current was induced across the p-n junction, with the degree of polarisation being controlled by both the bias across the p-n junction and by the position and focus of the laser spot. The polarisation of the current was then detected using so-called hall bars etched into the substrate transverse to the 2DEG/2DHG channel (see Figure 4), with the variation in voltage being proportional to the purity of the spin current.

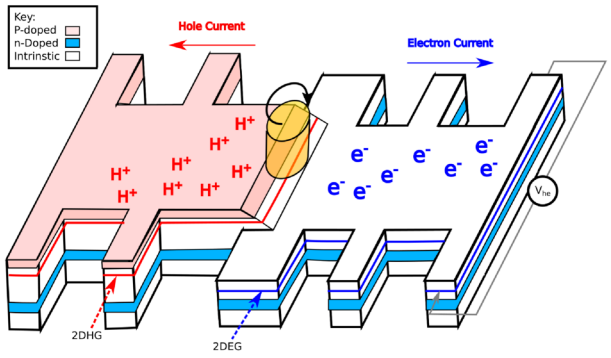

Figure 4: Schematic of (2DEG–2DHG) photo-diode used to demonstrate spin detection using the spin hall effect. Adapted from reference [5] .

The spin hall transistor comprises of the same p-n photo junction this time; however, two lateral Hall bars spaced 2 µm apart were etched into the n-type side of the device, and a gate was placed on top of the of the 2DEG channel between the two hall crosses (see Figure 5). Spins were injected into the 2DEG using circularly polarised light, and the spin precession

caused by the electric field was measured via the change in voltage across the hall bars.

At a large reverse bias, ($V_G = -0.5\,\mathrm{V}$) the Hall signals disappeared since the diffusion of spin-polarised electrons from the injection region toward the detecting Hall cross was blocked by the repulsive potential of the gate electrode. However, by slowly increasing the gate bias they observed a non-linear hall voltage dependence. This dependence suggests that the intermediate gate electric field modified the spin precession of the injected electrons and therefore the local spin polarisation at the detecting Hall cross, analogous to the operation of the original Datta-Das Transistor.

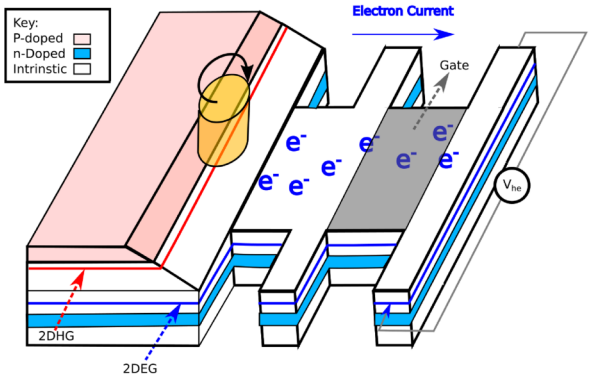

Figure 5: Schematic of Spin-Hall Transistor adapted from [6].

1.3 Overview

This document is split up into the following sections:

- **Section 1:** Introduces the project and its aims.
- **Sections 2-4:** Contain relevant background reading on spin dynamics, $\boldsymbol{k} \cdot \boldsymbol{p}$ band structure calculations and the Monte Carlo method.
- **Sections 5-7:** Details the method used to adapt the pre-existing finite element ensemble Monte Carlo simulation for spin transport and contains discussion and analysis of all the obtained results for the simulation of an $In_{0.3}Ga_{0.7}As$ spinFET.
- **Section 8:** presents conclusions and potential ideas for future work.

2 Representations of spin states

2.1 The Bloch Sphere

When measured the spin angular momentum can take one of two values $\pm\frac{\hbar}{2}$ thus electron spin can be thought of as existing in one of two states commonly refereed to as "up" and "down", the classical picture of which is that of the electron being a small bar magnet spinning either clockwise or anti-clockwise with the magnetic moment pointing towards the north or south pole respectively. However this picture breaks down due to quantum mechanics since the electron does not exist in two distinct states but instead as superposition of the two states $|\psi\rangle$ given by Equation (3)[30, 31].

$$|\psi\rangle = a\,|\uparrow\rangle + b\,|\downarrow\rangle\,, \tag{3}$$

where $|\uparrow\rangle$ and $|\downarrow\rangle$ represent the up and down states respectively whilst a and b are complex numbers for which the absolute value squared represents the probability the spin angular momentum is aligned with the up or down state, respectively, and are defined such that $|a^2| + |b^2| = 1$. A good visual way to represent $|\psi\rangle$ is to look at it as a unit vector bounded by a sphere (see figure 6). This vector can point in any direction defined by elevation and azimuth angles θ and ϕ such that:

$$|\psi\rangle = \cos\left(\frac{\theta}{2}\right)|\uparrow\rangle + e^{i\phi}\sin\left(\frac{\theta}{2}\right)|\downarrow\rangle \tag{4}$$

with $0 \leq \theta \leq \pi$ and $0 \leq \phi \leq 2\pi$.

This representation is known as the Bloch sphere and is a good way to visualise the quantum state $|\psi\rangle$ of a single spin. We note however that as a consequence of how the Bloch sphere is defined orthogonal quantum states (i.e., arbitrary states $|a\rangle$ and $|b\rangle$ for which $\langle a|b\rangle = 0$) appear on opposite points of the sphere (rather than being drawn at right angles). Thus in this representation the "up" state $|\uparrow\rangle$ lies at the north pole (see figure 6) and the "down" state $|\downarrow\rangle$ is at the south pole with the superposition states represented by every other point on the sphere. [30] To obtain the expectation value of the spin we need an operator (with eigenvalues of $\pm\frac{\hbar}{2}$) to operate on the states $|\uparrow\rangle$ and $|\downarrow\rangle$. Such an operator was proposed by Pauli and is given by $\boldsymbol{S} = \frac{\hbar}{2}\boldsymbol{\sigma}$. Where $\boldsymbol{\sigma}$ represents the three 2×2 Pauli matrices σ_x, σ_y

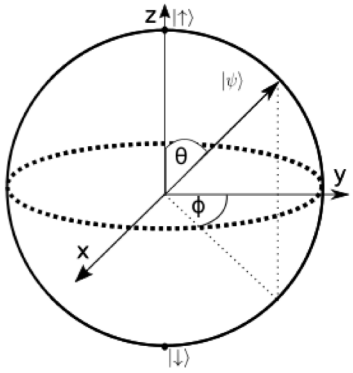

Figure 6: Diagram of Bloch Sphere.

and σ_z given by Equations (5) a-c.[11]

$$\sigma_x = \begin{pmatrix} 0 & 1 \\ 1 & 0 \end{pmatrix}, \tag{5a}$$

$$\sigma_y = \begin{pmatrix} 0 & -i \\ i & 0 \end{pmatrix}, \tag{5b}$$

$$\sigma_z = \begin{pmatrix} 1 & 0 \\ 0 & -1 \end{pmatrix}. \tag{5c}$$

Thus the result of any measurement of the spin component along an arbitrary axis defined by the unit vector $\boldsymbol{n}$ will be given by the eigenvalues of $\boldsymbol{S} \cdot \boldsymbol{n}$. These can be easily calculated by using the following equality for the Pauli spin matrices

$$(\boldsymbol{\sigma} \cdot \boldsymbol{a})(\boldsymbol{\sigma} \cdot \boldsymbol{b}) = i\boldsymbol{\sigma} \cdot (\boldsymbol{a} \times \boldsymbol{b}) + \boldsymbol{a} \cdot \boldsymbol{b} I,$$

where I is the 2×2 identity matrix and $\boldsymbol{a}$ and $\boldsymbol{b}$ are arbitrary 3 dimensional vectors. However, since $\boldsymbol{n}$ is a unit vector this reduces to

$$(\boldsymbol{\sigma} \cdot \boldsymbol{n})^2 = I,$$

which has eigenvalues of ± 1 regardless of the direction of $\boldsymbol{n}$. Thus, the eigenvalues of $\boldsymbol{S} \cdot \boldsymbol{n}$ will be $\pm \frac{\hbar}{2}$ regardless of the direction of $\boldsymbol{n}$.

Therefore, any point on the surface of the Bloch sphere will still give experimental values for the spin angular momentum of $\pm \frac{\hbar}{2}$ with the vector $\boldsymbol{S} \cdot \boldsymbol{n}$ being known as the Bloch vector.

2.2 Density Matrices and the representation of ensembles

To represent an ensemble of spin states a useful concept is an operator known as the density matrix which allows us to perform calculations for a collection of spins with an initial statistical distribution across the Bloch sphere and track their time evolution [31, 10]. We start with the state $|\psi\rangle$ given by Equation (3) however instead of representing a single electron we now use $|\psi\rangle$ to represent an ensemble of spins. This representation is known as a pure state since we know the spin of each electron in the system is either in the up or down state, with probabilities $|a|^2$ and $|b|^2$ respectively. (i.e the spin magnetic moment points parallel or anti-parallel to the unit vector $\boldsymbol{n}$, with a probability of $|a|^2$ or $|b|^2$ respectively).

The density matrix ρ for this system is given by the outer product:

$$\rho = |\psi\rangle\langle\psi| = \begin{pmatrix} a \\ b \end{pmatrix} \begin{pmatrix} a^* & b^* \end{pmatrix} = \begin{pmatrix} aa^* & ab^* \\ ba^* & bb^* \end{pmatrix} = \begin{pmatrix} |a|^2 & ab^* \\ ba^* & |b|^2 \end{pmatrix}. \tag{6}$$

The diagonal elements are the probabilities of being in each state whilst the off diagonal terms represents the capability of different components of a state to interfere with each other this is often referred to as the coherence. ρ has the following interesting properties which are true for all density matrices:

- It's hermitian (i.e. $\rho = \rho^\dagger$),
- It is a positive operator meaning $\langle u|\rho|u\rangle \geq 0$ for any state vector $|u\rangle$,
- $\mathrm{Tr}(\rho) = 1$ (since the sum of all probabilities is 1),
- The expectation value of an operator A can be shown to be $\langle A\rangle = \mathrm{Tr}(\rho A)$.

However real quantum systems are seldom found in pure states, often we consider systems that are a statistical mixture of many different states. In our case, each electron in our ensemble might well be in a different state. Thus for an ensemble of N electrons we have $|\psi_N\rangle$ state vectors, we can however still use the density matrix by simply using a few extra steps:

1. Construct density matrices for each state in the ensemble
2. Multiply each matrix by the probability of that state being in the ensemble
3. Sum over all the possible states.

Thus for a mixed state the density matrix for the entire system is given by:

$$\rho = \sum_{i=1}^{N} P_i \left|\psi_i\right\rangle\!\left\langle\psi_i\right| \tag{7}$$

Where P_i is the probability that an electron in the ensemble is found in the state $|\psi_i\rangle$.

Since we can in principle construct a density matrix from any set of basis states, the matrix representation is not unique thus we need a system to determine if the ensemble is in a mixed or pure state. Fortunately, for a pure state, it can easily be shown that $\rho^2 = \rho$ by using the definition of ρ in Equation (6) thus:

$$\rho^2 = \left(|\psi\rangle\langle\psi|\right)^2 = |\psi\rangle \langle\psi|\psi\rangle \langle\psi| = |\psi\rangle\langle\psi| = \rho \tag{8}$$

and since $\mathrm{Tr}(\rho) = 1 \rightarrow \mathrm{Tr}(\rho^2) = 1$. This is not, however, the case for a mixed state thus we can use this fact to construct a definite test for the purity of our system. Whereby if $\mathrm{Tr}(\rho^2) = 1$ we have a pure state and if $\mathrm{Tr}(\rho^2) < 1$ we have a mixed state.

Finally, we can tie the density matrix back to the Bloch sphere with following theorem[10]:

Theorem 1 *Any* 2×2 *matrix* M *can be decomposed into products of the 3 Pauli matrices and the* 2×2 *identity matrix* I *as follows:*

$$M = \begin{pmatrix} m_{11} & m_{12} \\ m_{21} & m_{22} \end{pmatrix}$$

$$M = \frac{m_{11} + m_{22}}{2} I + \frac{m_{11} - m_{22}}{2}\sigma_z + \frac{m_{12} + m_{21}}{2}\sigma_x + \frac{m_{12} - m_{21}}{2}\sigma_y \tag{9}$$

So if we define a general density matrix ρ as:

$$\rho = \begin{pmatrix} a + b & c - id \\ c + id & a - b \end{pmatrix} \tag{10}$$

Where a,b,c and d are real numbers, using theorem 1 we obtain:

$$\rho = aI + c\sigma_x + d\sigma_y + b\sigma_z \tag{11}$$

and since we know that $\mathrm{Tr}(\rho) = 1$ we have $2a = 1$ thus we can write:

$$\rho = \tfrac{1}{2}(I + 2c\sigma_x + 2d\sigma_y + 2b\sigma_z) \tag{12}$$

However we also know from our density matrix rules the expectation value of an operator A is given by $\langle A\rangle = \mathrm{Tr}(\rho A)$ therefore:

$$\langle\sigma_x\rangle = \mathrm{Tr}(\rho\sigma_x) = 2c \tag{13a}$$

$$\langle\sigma_y\rangle = \mathrm{Tr}(\rho\sigma_y) = 2d \tag{13b}$$

$$\langle\sigma_z\rangle = \mathrm{Tr}(\rho\sigma_z) = 2b \tag{13c}$$

and ρ can be written as:

$$\rho = \tfrac{1}{2}(I + \boldsymbol{V}\cdot\boldsymbol{\sigma}) \tag{14}$$

Where $\boldsymbol{V}$ is the Bloch vector of the system represented by the density matrix ρ and is given by $\boldsymbol{V} = (\langle\sigma_x\rangle, \langle\sigma_y\rangle, \langle\sigma_z\rangle)$.

The magnitude of $\boldsymbol{V}$ can be used as another test of the system's purity since we recall that for any density matrix $\mathrm{Tr}(\rho^2) \leq 1$

$$\rho^2 = \left(\tfrac{1}{2}(I + \boldsymbol{S}\cdot\boldsymbol{\sigma})\right)^2 = \frac{1}{4}\begin{pmatrix} (\langle\sigma_z\rangle + 1)^2 + \langle\sigma_x\rangle^2 + \langle\sigma_y\rangle^2 & 2\langle\sigma_x\rangle - 2i\langle\sigma_y\rangle \\ 2\langle\sigma_x\rangle + 2i\langle\sigma_y\rangle & (\langle\sigma_z\rangle - 1)^2 + \langle\sigma_x\rangle^2 + \langle\sigma_y\rangle^2 \end{pmatrix}$$

$$\mathrm{Tr}(\rho^2) = \frac{1}{4}\Big((\langle\sigma_z\rangle + 1)^2 + (\langle\sigma_z\rangle - 1)^2 + 2\langle\sigma_x\rangle^2 + 2\langle\sigma_y\rangle^2\Big) = \frac{1}{2}\Big(1 + \|\boldsymbol{V}\|\Big) \leq 1 \tag{15}$$

For a pure state therefore the Bloch vector $\boldsymbol{V}$ must have a length of 1 and (much like the single particle case) can be represented by a point on the surface of the Bloch sphere. However for a mixed case we recall $\mathrm{Tr}(\rho) < 1$ therefore $\boldsymbol{V}$ must have a length less than 1 and Bloch vector will represent a point inside the sphere.

2.2.1 Completely mixed states

In our discussion of both pure and mixed states we have so far omitted to account for the extreme opposite of a pure state the so called completely mixed state. This is a perfectly even statical distribution of N states which cover all possible values. Whilst in practice this type of mixed state is difficult to achieve exactly, when dealing with large ensembles of electrons in random distributions of spin states it is entirely possible for the density matrix of the system to approach this kind of state.

The density matrix for such a state is in principle relatively easy to find since the probability for the system to be in each given state is identical. Thus the density matrix will be a constant multiple of the identity matrix. So for a state space of n dimensions:

$$\rho = \frac{1}{n}I \tag{16}$$

and since $I^2 = I$ and $\mathrm{Tr}(I) = n$ we have:

$$\rho^2 = \frac{1}{n^2} I$$
$$\mathrm{Tr}(\rho^2) = \frac{1}{n}$$

For the case of electron spin $n = 2$ thus the lower bound of our purity test will be $1/2$ whilst the upper bound will be 1 (i.e. a pure state). Finally, using Equation (15) we can see that Bloch vector for a completely mixed state must be zero. Physical this makes perfect sense since the individual magnetic moments of the electrons in the ensemble will point in a different direction such that there will be no net magnetic moment.

2.2.2 Time evolution

For a pure state the time evolution of ρ is relatively easy to obtain by using the definition of ρ given by Equation (6)

$$\frac{\mathrm{d}\rho}{\mathrm{d}t} = \frac{\mathrm{d}}{\mathrm{d}t}\big(|\psi\rangle\langle\psi| \big) = \left(\left(\frac{\mathrm{d}}{\mathrm{d}t} |\psi\rangle \right) \langle\psi| + |\psi\rangle \left(\frac{\mathrm{d}}{\mathrm{d}t} \langle\psi| \right) \right) \tag{17}$$

and since the state $|\psi\rangle$ satisfies the time-dependant Schrödinger Equation [11, 32] we have:

$$i\hbar \frac{\mathrm{d}}{\mathrm{d}t} |\psi\rangle = H |\psi\rangle$$
$$\frac{\mathrm{d}\rho}{\mathrm{d}t} = -\frac{i}{\hbar}\big(H |\psi\rangle\langle\psi| - |\psi\rangle\langle\psi| H \big) = -\frac{i}{\hbar}[H, \rho] \tag{18}$$

We can similarly derive the time evolution of a mixed state as:

$$\frac{\mathrm{d}\rho}{\mathrm{d}t} = \frac{\mathrm{d}}{\mathrm{d}t}\left(\sum_j p_j |\psi_j\rangle\langle\psi_j| \right) = \sum_j p_j \left(\left(\frac{\mathrm{d}}{\mathrm{d}t} |\psi_j\rangle \right) \langle\psi_j| + |\psi_j\rangle \left(\frac{\mathrm{d}}{\mathrm{d}t} \langle\psi_j| \right) \right)$$
$$= -\frac{i}{\hbar} \sum_j p_j \big(H |\psi_j\rangle\langle\psi_j| - |\psi_j\rangle\langle\psi_j| H \big) = -\frac{i}{\hbar}[H, \rho]$$

Thus equation (18) applies to both pure and mixed states and is known as the Von Neumann equation [33]

Now we know from basic quantum mechanics[11] that the sate of a system $|\psi\rangle$ at time t_1 is related to its state at time t_2 by a unitary operator U which depends only on t_1 and t_2.

$$|\psi(t_2)\rangle = U(t_1, t_2) |\psi(t_1)\rangle$$

For our system we can therefore say:

$$|\psi_j(t)\rangle = U(t)\,|\psi_j(0)\rangle$$
$$\langle\psi_j(t)| = \langle\psi_j(0)|\,U^\dagger(t)$$

and hence:

$$\rho(t) = \sum_j p_j U(t)\,|\psi_j(0)\rangle\,\langle\psi_j(0)|\,U^\dagger(t) = U(t)\rho(0)U^\dagger(t) \tag{19}$$

So we can now calculate how the length of the Bloch vector changes with time as:

$$\mathrm{Tr}(\rho^2(t)) = U(t)\rho^2(0)U^\dagger(t) = U(t)\rho(0)\rho(0)U^\dagger(t)$$

and since by definition $U(t)U^\dagger(t) = 1$

$$\mathrm{Tr}(\rho^2(t)) = \mathrm{Tr}(\rho^2(0)) \tag{20}$$

and therefore the time evolution preserves the length of the Bloch vector and it moves inside the Bloch ball staying at a fixed distance from the centre. In reality, however, the magnetisation will decay due to interactions with the environment this is characterised by the so called Bloch equations which are the subject of the next section.

2.3 Spin relaxation and the Bloch Equations

Using Equations (18) and (14) we can obtain the equation of motion for the Bloch vector as:

$$\begin{aligned}\frac{\mathrm{d}v_j}{\mathrm{d}t} = \frac{\mathrm{d}}{\mathrm{d}t}\mathrm{Tr}(\rho\sigma_j) = \mathrm{Tr}\left(\sigma_j\frac{\mathrm{d}}{\mathrm{d}t}\rho\right) &= -\frac{i}{\hbar}\mathrm{Tr}\big(\sigma_j[H,\rho]\big) \\ &= -\frac{i}{2\hbar}\mathrm{Tr}\big(\sigma_j[H, I + \boldsymbol{V}\cdot\boldsymbol{\sigma}]\big)\end{aligned} \tag{21}$$

In order to understand the spin relaxation it is helpful to look at the time dependence of the individual components of v_j (v_x, v_y and v_z). For a spin 1/2 particle in a magnetic field orientated in an arbitrary direction we can calculate the component v_j of equation (21) in the following way.

The Hamiltonian H for the system, where the gyromagnetic factor γ is given by:

$$H = -\gamma(\boldsymbol{S}\cdot\boldsymbol{B}) = -\gamma\frac{\hbar}{2}(\boldsymbol{\sigma}\cdot\boldsymbol{B}) \tag{22}$$

Substituting this into equation (21) gives:

$$\begin{aligned}\frac{\mathrm{d}v_j}{\mathrm{d}t} &= -\frac{i}{2\hbar}\mathrm{Tr}\Big(\langle\sigma_j\rangle\big[-\gamma\tfrac{\hbar}{2}(\boldsymbol{\sigma}\cdot\boldsymbol{B}),(1+\boldsymbol{V}\cdot\boldsymbol{\sigma})\big]\Big)\\ &= -\frac{i\gamma}{4}\mathrm{Tr}\Big(\sigma_j(\boldsymbol{\sigma}\cdot\boldsymbol{B})(1+\boldsymbol{V}\cdot\boldsymbol{\sigma})-\sigma_j(1+\boldsymbol{V}\cdot\boldsymbol{\sigma})(\boldsymbol{\sigma}\cdot\boldsymbol{B})\Big)\end{aligned} \tag{23}$$

We can then expand out the two dot products and re-group terms to obtain:

$$\begin{aligned}\frac{\mathrm{d}v_j}{\mathrm{d}t} &= \frac{i\gamma}{4}\mathrm{Tr}\big(\sigma_j\sigma_x\sigma_y(B_xv_y-v_xB_y)+\sigma_j\sigma_x\sigma_z(B_xv_z-v_xB_z)+\sigma_j\sigma_y\sigma_x(B_yv_x-v_yB_x)\big)\\ &+\frac{i\gamma}{4}\mathrm{Tr}\big(\sigma_j\sigma_y\sigma_z(B_yv_z-v_yB_z)+\sigma_j\sigma_z\sigma_x(B_zv_x-v_zB_x)+\sigma_j\sigma_z\sigma_y(B_zv_y-v_zB_y)\big)\end{aligned} \tag{24}$$

Focusing on the x-component first we have:

$$\begin{aligned}\frac{\mathrm{d}v_x}{\mathrm{d}t} &= \frac{i\gamma}{4}\mathrm{Tr}(\sigma_x\sigma_x\sigma_y(B_xv_y-v_xB_y)+\sigma_x\sigma_x\sigma_z(B_xv_z-v_xB_z)+\sigma_x\sigma_y\sigma_x(B_yv_x-v_yB_x))\\ &+\frac{i\gamma}{4}\mathrm{Tr}(\sigma_x\sigma_y\sigma_z(B_yv_z-v_yB_z)+\sigma_x\sigma_z\sigma_x(B_zv_x-v_zB_x)+\sigma_x\sigma_z\sigma_y(B_zv_y-v_zB_y))\end{aligned} \tag{25}$$

and since $\sigma_x^2=1$ this simplifies to:

$$\begin{aligned}\frac{\mathrm{d}v_x}{\mathrm{d}t} &= \frac{i\gamma}{4}\mathrm{Tr}(\sigma_y(B_xv_y-v_xB_y)+\sigma_z(B_xv_z-v_xB_z)+\sigma_y(B_yv_x-v_yB_x))\\ &+\frac{i\gamma}{4}\mathrm{Tr}(\sigma_x\sigma_y\sigma_z(B_yv_z-v_yB_z)+\sigma_z(B_zv_x-v_zB_x)+\sigma_x\sigma_z\sigma_y(B_zv_y-v_zB_y))\end{aligned} \tag{26}$$

Now since for any A and C, $\mathrm{Tr}(AC)=C\mathrm{Tr}(A)$ [34] Equation (26) can be further simplified thanks to the fact that $\mathrm{Tr}(\sigma_x)=\mathrm{Tr}(\sigma_y)=\mathrm{Tr}(\sigma_z)=0$ thus:

$$\frac{\mathrm{d}v_x}{\mathrm{d}t} = \frac{i\gamma}{4}\mathrm{Tr}(\sigma_x\sigma_y\sigma_z(B_yv_z-v_yB_z)+\sigma_x\sigma_z\sigma_y(B_zv_y-v_zB_y)) \tag{27}$$

$$= \frac{i\gamma}{4}(B_yv_z-v_yB_z)\mathrm{Tr}(\sigma_x\sigma_y\sigma_z-\sigma_x\sigma_z\sigma_y) \tag{28}$$

Finally since $\sigma_x\sigma_y\sigma_z=iI$ and $\sigma_x\sigma_z\sigma_y=-iI$ we obtain:

$$\frac{\mathrm{d}v_x}{\mathrm{d}t} = -\gamma(B_yv_z-v_yB_z) \tag{29a}$$

and following a similar procedure for the y and z components we have.

$$\frac{\mathrm{d}v_y}{\mathrm{d}t} = -\gamma(B_zv_x-v_zB_x) \tag{29b}$$

$$\frac{\mathrm{d}v_z}{\mathrm{d}t} = -\gamma(B_xv_y-v_xB_y) \tag{29c}$$

Using Equations (29a)-(29c) we can begin to construct a more realistic model for the time evolution of the Bloch vector. Fortunately, Bloch proposed such a modification [35] by way of describing the interaction of spins with the environment using parameters known as the longitudinal (T_1) and transverse (T_2) relaxation times. If we then take an ensemble of spins at $t = 0$ and subject them to a constant magnetic field B_0 along the z-axis. Equations (29a)-(29c) become:

$$\frac{\mathrm{d}v_x}{\mathrm{d}t} = \gamma(B_0 v_y) \tag{30a}$$

$$\frac{\mathrm{d}v_y}{\mathrm{d}t} = -\gamma(B_0 v_x) \tag{30b}$$

$$\frac{\mathrm{d}v_z}{\mathrm{d}t} = 0 \tag{30c}$$

Thus the Bloch vector will rotate on a cone centered around the z-axis with Larmor frequency $\omega = \gamma B_0$. This procession is equivalent to the NMR system studied by Bloch [35] in which he and his collaborators recorded a nuclear induction signal through the generation of a small current in their receiver coil due to the net magnetisation from the ensemble of nuclei processing around B_0. However, the recorded signal decayed and was dependant on the material used and the rate of change of the applied magnetic field.

Bloch surmised that the decay in the signal was due to the interaction of the spins with both the environment and each other. The two types of interaction were given time constants T_1 and T_2. T_1 is the time taken for the z-component of the magnetisation to return to some equilibrium value v_{z0} which is determined by Boltzmann statistics (or more accurately the time taken to for v_z to grow from 0 to $(1 - \frac{1}{e}) \approxeq 63\%$ of its final value[35]). This type of relaxation is usually associated with each nucleus slowly losing energy to the environment and thus returning from an excited state to thermodynamic equilibrium. The time T_2 is the time taken for the x and y components of the magnetisation to decay due to interactions between the individual spins in the ensemble (again this is more accurately defined by Bloch to be the time taken for the magnetisation to decay to a value of $\frac{1}{e} \approxeq 37\%$ of the initial value[35]).

Thus we can modify equations (29a)-(29c) to give

$$\frac{\mathrm{d}v_x}{\mathrm{d}t} = -\gamma(B_y v_z - v_y B_z) - \frac{v_x}{T_2} \tag{31a}$$

$$\frac{\mathrm{d}v_y}{\mathrm{d}t} = -\gamma(B_z v_x - v_z B_x) - \frac{v_y}{T_2} \tag{31b}$$

$$\frac{\mathrm{d}v_z}{\mathrm{d}t} = -\gamma(B_x v_y - v_x B_y) - \frac{v_z - v_{z0}}{T_1} \tag{31c}$$

Where v_{z0} is the thermodynamic equilibrium magnetization.

Thus we now have a way to track how the Bloch vector (and hence average magnetisation of the ensemble) varies with time.

2.4 Spin-Orbit coupling in semiconductors

The main mechanism that gives rise to spin relaxation (and by extension the spin relaxation times T_1 and T_2) is spin-orbit interaction. This means electrons will interact with the positively charged atomic nucleus as they orbit. This interaction can be determined using two different approaches depending if the electron is moving at relativistic speeds or not [36, 37, 38]. For the relativistic case, a magnetic field is said to be generated in the electron's frame of reference as it orbits the nucleus. This field will have a flux density given by:

$$\boldsymbol{B} = \frac{\boldsymbol{\varepsilon} \times \boldsymbol{v}}{c^2 \gamma_{rel}}, \tag{32}$$

where: $\boldsymbol{\varepsilon}$ represents the electric field, $\boldsymbol{v}$ is the orbital velocity of the electron and c is the speed of light in a vacuum and $\gamma_{rel} = \sqrt{1 - \frac{\boldsymbol{v}^2}{c^2}}$.

However as pointed out by an article published in Nature [39] we need to adapt Equation (32) with a factor of $(g-1)/2$ where g is the Landé g-factor (which is equal to 2 in a vacuum) since the normal Lorentz transform is inexact since the electron is constantly changing direction as it accelerates. Thus we now have:

$$\boldsymbol{B} = \frac{\boldsymbol{\varepsilon} \times \boldsymbol{v}}{2c^2 \gamma_{rel}} \tag{33}$$

Since the spinning electron has a magnetic moment $\boldsymbol{\mu_e}$ [40, 10] the energy of the interaction with $\boldsymbol{B}$ is given by

$$E = -\boldsymbol{\mu_e} \cdot \boldsymbol{B} \tag{34}$$

Using the gyromagnetic ratio g_0 to relate the magnetic moment to the angular momentum $\boldsymbol{S}$ as $\boldsymbol{\mu_e} = -g_0 \mu_B \boldsymbol{S}$ (where μ_B is the Bohr magneton) Equation (34) becomes:

$$E = g_0 \mu_B \boldsymbol{S} \cdot \boldsymbol{B} \tag{35}$$

Thus using equation (32) we obtain:

$$E = g_0 \mu_B \frac{\boldsymbol{\varepsilon} \times \boldsymbol{v}}{2c^2 \gamma_{rel}} \cdot \boldsymbol{S} \tag{36}$$

and since $\boldsymbol{S} = \frac{1}{2}\boldsymbol{\sigma}$ and $\mu_B = \frac{e\hbar}{2m}$

$$E_{relativistic} = \frac{g_0 e\hbar}{4m}\frac{\boldsymbol{\varepsilon} \times \boldsymbol{v}}{c^2\gamma_{rel}} \cdot \boldsymbol{\sigma} \tag{37}$$

For the non relativistic case we take a different approach [38]. If we observe the orbit from the point of view of the electron we would perceive the electron to be stationary and the nucleus to be moving around the electron at a distance $\boldsymbol{r}$ with a velocity $\boldsymbol{v}_{orbit}$. Thus we can apply Biot Savart's law to calculate the flux density as:

$$\boldsymbol{B} = Ze\frac{\boldsymbol{r} \times \boldsymbol{v_{orbit}}}{4\pi\epsilon_0 c^2 r^3}, \tag{38}$$

where ϵ_0 is the permittivity of free space and $+Ze$ is the charge of the nucleus.

Since $\frac{Ze\boldsymbol{r}}{4\pi\epsilon_0 c^2 r^3} = \boldsymbol{\varepsilon}$ we obtain

$$\boldsymbol{B} = \frac{\boldsymbol{\varepsilon} \times \boldsymbol{v_{orbit}}}{c^2} \tag{39}$$

using which we can follow the same procedure as the relativistic case (i.e. using Equation (35)) to obtain an expression for the energy.

$$E_{nonrel} = g_0\mu_B\frac{\boldsymbol{\varepsilon} \times \boldsymbol{v}}{c^2} \cdot \boldsymbol{S} = \frac{g_0 e\hbar}{2m}\frac{\boldsymbol{\varepsilon} \times \boldsymbol{v}}{c^2} \cdot \boldsymbol{\sigma} \tag{40}$$

Which is equivalent to Equation (37) just without the relativistic correction to the velocity or the Thomas factor of 1/2.

Finally using Equation (37) the Hamiltonian for the spin orbit interaction of a free electron in a vacuum is given by:

$$H_{so} = -\frac{e\hbar}{4m^2c^2\gamma_{rel}}(\boldsymbol{\nabla}V \times \boldsymbol{p}) \cdot \boldsymbol{\sigma} \approx -\frac{e\hbar}{4m^2c^2}(\boldsymbol{\nabla}V \times \boldsymbol{p}) \cdot \boldsymbol{\sigma} \tag{41}$$

where V is the electric potential and $\boldsymbol{p}$ is the momentum operator.

This single atom case, however, does not extend to electrons in crystal lattices since, due to shielding effects, electrons in the conduction band do not experience any strong nuclear attraction. Even so, internal effects within the lattice can still produce similar types of spin-orbit interaction to that of Equation (41). For conduction electrons the three primary mechanisms for spin relaxation are known as The Elliott–Yafet (EY), D'yakonov–Perel (DP), and Bir–Aronov–Pikus (BAP) mechanisms[41] (see figure 7.)

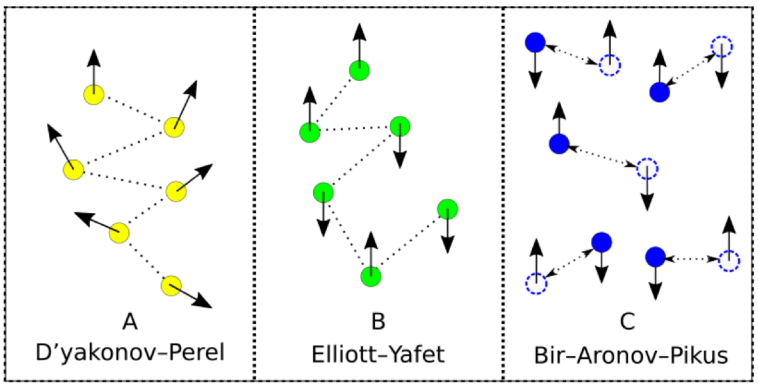

Figure 7: Diagram to show the various mechanisms of spin relaxation in semiconductors. **A. The D'yakonov-Perel Mechanism:** The electron spins precess around magnetic fields caused by the breaking of symmetry, as the electrons undergo scattering the field changes direction and hence the magnetic moment of the electron aligns with the new field. Since each electron "sees" a different field, the individual magnetic moments precess at different rates and hence spread out randomly in space resulting in the net magnetisation decaying to zero. **B. The Elliott-Yafet Mechanism:** The periodic spin-orbit interaction due to the lattice causes the spin "up/down" Bloch states to contain small spin-down/up amplitude this means there is a small probability a scattering event can flip the spin from an up to a down-state (or vice versa). **C. The Bir-Arnov-Pikus mechanism:** Exchange interactions between electrons and holes cause the electron spins to precess along an effective magnetic field determined by hole spins. This field is extremely localised and randomly changes due to hole relaxation hence we see a similar spin relaxation effect to that of DP.

2.4.1 The Elliott-Yafet Mechanism

The Elliot-Yafet mechanism was first proposed by Elliott in 1954 [42] and is considered the dominant relaxation method in elemental semiconductors (e.g. Si)[43]. It works on the principle that in a crystal lattice the Bloch states are not true eigenstates. The periodic spin-orbit interaction means the "up" state contains a small down amplitude b (and vice versa). Normally this is not a problem since the spin-orbit coupling δ_{so} is small compared to the bandwidth Δ_E and so can be treated as a perturbation with b being of the order $\frac{\delta_{so}}{\Delta_E}$ and thus since b is small we can still label the states "up" and "down" according to their largest spin component. Elliott also noted that the amplitude b is dependant on the wave vector $\boldsymbol{k}$ thus any non-magnetic scattering events that change the value of $\boldsymbol{k}$ by a significant amount (e.g. Impurities, acoustic phonon, device boundaries etc.) All have a probability of causing the spin to flip from an "up" to a "down" state (or vice versa) with spin flips being favoured by scattering events that cause larger changes in $\boldsymbol{k}$ (such as acoustic phonons that scatter through large angles). Elliott then went on to build on the work of Overhauser who did similar work on spin-orbit interaction with impurities in metals[44] to calculate a spin relaxation rate $\frac{1}{T_{EY}}$ which is directly proportional to the momentum relaxation rate $\frac{1}{T_m}$. With the relationship between the two being defined as[42]:

$$\frac{T_m}{T_{EY}} \propto \frac{\Delta_0}{E_g}, \tag{42}$$

where: Δ_0 is the spin-orbit splitting of the valence band and E_g is the band-gap.

Yafet then later showed [45] that this relationship was temperature independent (baring the weak temperature dependence of Δ_0 and E_g) and thus T_m and T_{so} have the same temperature dependence of $1/T_{so} \propto T$ for temperatures above the Debye temperature T_D and $1/T_{so} \propto T^5$ below that This was then later demonstrated experimentally for metals by Monod and Beuneu [46].

2.4.2 The D'yakonov-Perel Mechanism

The D'yakonov-Perel mechanism is considered the dominant cause of spin relaxation in III-V and II-IV materials. It is caused by spin-orbit coupling with electric fields generated due to the breaking of inversion symmetry of the lattice. This symmetry breaking can be grouped into two mechanisms: Structural (SIA: often referred to as Rashba coupling) and Bulk inversion Asymmetry (BIA: also called Dresselhaus coupling). The former arises

from the electric field generated by gradients in the internal potential energy (such as band discontinuities in Heterostructures) or external fields applied via the use of gates. The latter occurs if the crystal lattice itself is not symmetric as is the case with III-V semiconductors such as GaAs in which the constituent atoms create dipoles as they are repeated throughout the lattice.

D'yakonov and Perel first studied these effects in 1971 [47] where they investigated electron spin orientation using circularly polarised light. They posited that relaxation occurs because the electric fields caused by the symmetry breaking are k-dependent so when the spins encounter these fields they will begin to process around them until a momentum change occurs due to scattering. This will change the direction and orientation of the field at which point the precession will start again but along a different axis.

Thus if we consider the Bloch vector for an ensemble of electrons drifting through the lattice, with spins that are initially all polarised in the same direction and the individual electron velocities do not change with time (i.e. the electrons don't undergo any form of scattering). We can see that the k-dependant field $B(\boldsymbol{k})$ is the same for all the electrons. Thus the spins will precess around the field at the same frequency, and after an arbitrary time, t will still be pointing in the same direction. Hence the magnitude of the Bloch vector will be unchanged, and no spin relaxation will occur. However if the electrons do undergo scattering, after time t the individual spins will all be pointing in random directions due to each one experiencing different changes in $\boldsymbol{k}$. This will cause them to process at random angles along all three axes while the Bloch vector (and by extension the net magnetisation) will decay to zero as the individual spins in the ensemble spread out across the Bloch sphere.

To account for the both of these mechanisms, we will need to compute a 14×14 Hamiltonian for the system using the $\boldsymbol{k} \cdot \boldsymbol{p}$ method to calculate the band structure in the vicinity of a known point in the Brillouin zone. In our case, we can easily incorporate the effects of spin-orbit coupling (and eventually strain) into these calculations and thus investigate the impact of spin relaxation on an electron in a crystal lattice. This method is discussed in detail in section 3.

2.4.3 The Bir-Arnov-Pikus mechanism

The Bir-Arnov-Pikus mechanism is a form of spin relaxation that occurs in systems with large concentrations of holes (e.g. heavily doped semiconductors) and is associated with a

spin-dependent exchange interaction between electrons and holes. Bir, Aronov, and Pikus first investigated by this [48] (after whom the effect is named), and posited that if there is a large concentration of holes the electrons will generally be in proximity to a hole thus the wave functions will overlap and an exchange interaction will occur. This interaction causes the electron spins to "see" the hole spins as a pseudo-magnetic field and they will begin to process about this field. However, hole spins change at a much faster rate than electron spin precession. Thus the magnetic field associated with the hole spin will change after a random time, after which the electron spin will precess around the new magnetic field, this causes spin relaxation in manner analogues to that of D'yakonov-Perel whereby the Bloch vector will slowly shrink as the electron spins diverge from one another and spread across the Bloch sphere.

The rate at which this occurs τ_{BAP}^{-1} is proportional to the hole relaxation time and was estimated for bulk semiconductors by reference [49] to be:

$$\frac{1}{\tau_{BAP}} = \frac{2a_B^3}{\tau_0 v_B}\left(\frac{2E_{cb}}{m^*}\right)^{1/2}\left(n_f|\psi(0)|^2 + \frac{5}{3}n_b\right), \tag{43}$$

where n_a and n_b are the concentrations of free and bound holes respectively, E_{cb} is the energy of an electron in the conduction band and

$$a_B = \left(\frac{m_0}{\mu}\right)\epsilon_r a_0 \qquad v_B = \frac{\hbar}{\mu a_B}$$
$$\tau_0 = \frac{64E_B\hbar}{3\pi\Delta_x^2} \qquad E_B = \frac{\hbar^2}{2\mu a_B^2}$$
$$|\psi(0)|^2 = \tfrac{2\pi}{\kappa}\left(1 - e^{-\frac{2\pi}{\kappa}}\right)^{-1} \qquad \kappa = \sqrt{E/E_B}$$

.

2.5 Overview

In this chapter we have presented the theoretical basis for modelling spin and spin transport using the Bloch equation and the main mechanisms for spin orbit coupling in semiconductors. In the next chapter we will cover electronic bandstructure calculations in bulk semiconductors using the $\boldsymbol{k}\cdot\boldsymbol{p}$ method.

3 Bandstructure Calculations: The *k.p* method

Electronic bandstructure calculations are useful for understanding many kinds of physical phenomenon associated with semiconductors. One such procedure for conducting these calculations is known as the $\boldsymbol{k} \cdot \boldsymbol{p}$ method and is a powerful technique for evaluating band structures of both bulk semiconductors and heterostructures. Starting with a point in $\boldsymbol{k}$-space $\boldsymbol{k}_0$ for which the eigenvalues and eigenfunctions are known exactly, the basic technique involves calculating the band dispersion away from $\boldsymbol{k}_0$, through the use of non-degenerate perturbation theory. The precise position in $\boldsymbol{k}$-space of $\boldsymbol{k}_0$ is arbitrary. However, it is usual to take a point of high symmetry such as the Γ or X point to exploit the symmetry when dealing with momentum matrix elements (see Figure 8).

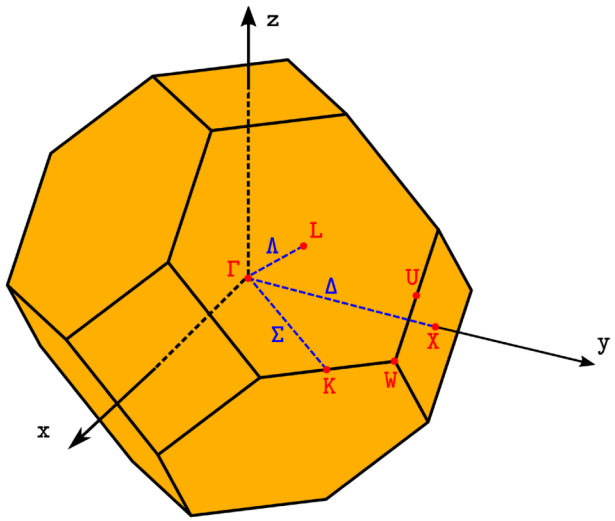

Figure 8: Diagram to show the first Brillouin zone for an FCC lattice. The point Γ is located is located at the centre of the Brillouin zone (i.e. $k_x = k_y = k_z = 0$), the capital letters: X ,K ,L ,U and W (shown in red) indicate the points of high symmetry and the remaining Greek letters: Δ, Σ and Λ (shown in blue) denote lines of high symmetry.

We start with the general Schrödinger equation for an electron in a 3D crystal with spin orbit coupling:

$$H\psi(\boldsymbol{r}) = \left(\frac{\boldsymbol{p}^2}{2m_0} + G(\boldsymbol{r}) + \frac{\hbar}{4m_0^2c^2}(\boldsymbol{\nabla} V \times \boldsymbol{p} \cdot \boldsymbol{\sigma}) \right) \psi(\boldsymbol{r}) = E\psi(\boldsymbol{r}) \tag{44}$$

Where $\boldsymbol{p} = -i\hbar\boldsymbol{\nabla}$, V is the crystal potential and $G(\boldsymbol{r})$ is the periodic potential of the lattice and obeys $G(\boldsymbol{r}) = G(\boldsymbol{r} + \boldsymbol{R})$ for all vectors $\boldsymbol{R}$ of the direct lattice. We can now use Bloch's

Theorem to re-write equation (44) as[50]

$$\left(\frac{\boldsymbol{p}^2}{2m_0}+G(\boldsymbol{r})+\frac{\hbar}{4m_0^2c^2}\big(\boldsymbol{\nabla}V\times\boldsymbol{p}\big)\cdot\boldsymbol{\sigma}+\frac{\hbar}{m_0}\boldsymbol{k}\cdot\boldsymbol{p}+\frac{\hbar^2k^2}{2m_0}+\frac{\hbar}{4m_0^2c^2}\big(\boldsymbol{\nabla}V\times\boldsymbol{k}\big)\cdot\boldsymbol{\sigma}\right)u_{nk}(\boldsymbol{r})=Eu_{nk}(\boldsymbol{r}) \quad (45)$$

The term $\frac{\hbar}{4m_0^2c^2}\big(\boldsymbol{\nabla}V\times\boldsymbol{k}\big)\cdot\boldsymbol{\sigma}$ is a $\boldsymbol{k}$-dependent spin-orbit interaction, which is small compared with the other terms because the crystal momentum $\boldsymbol{k}$ is small compared with $\boldsymbol{p}$ thus this term is often neglected and equation (45) can be simplified to:

$$Hu_{nk}(\boldsymbol{r})\approx\left(\frac{\boldsymbol{p}^2}{2m_0}+G(\boldsymbol{r})+\frac{\hbar}{4m_0^2c^2}\big(\boldsymbol{\nabla}V\times\boldsymbol{p}\big)\cdot\boldsymbol{\sigma}+\frac{\hbar}{m_0}\boldsymbol{k}\cdot\boldsymbol{p}+\frac{\hbar^2k^2}{2m_0}\right)u_{nk}(\boldsymbol{r})=Eu_{nk}(\boldsymbol{r}) \quad (46)$$

In order to solve equation (46) we need to make use of perturbation theory, we assume that the solution to the Schrödinger equation is known for a particular potential with Hamiltonian H_0 and we have obtained the eigenfunctions $|n\rangle$ and eigenvalues ε_n^0 of n bands such that

$$H_0\,|n\rangle=\varepsilon_n^0\,|n\rangle$$

We now take a new Hamiltonian H which is close to our original Hamiltonian H_0 but differs by a small amount W thus $H=H_0+W$. We can apply this approach to equation (46) by noting that our Hamiltonian has two parts one that is k-dependant and one that is not.

$$Hu_{nk}(\boldsymbol{r})\approx\Bigg(\underbrace{\frac{\boldsymbol{p}^2}{2m_0}+G(\boldsymbol{r})+\frac{\hbar}{4m_0^2c^2}\big(\boldsymbol{\nabla}V\times\boldsymbol{p}\big)\cdot\boldsymbol{\sigma}}_{H_0}+\underbrace{\frac{\hbar}{m_0}\boldsymbol{k}\cdot\boldsymbol{p}+\frac{\hbar^2k^2}{2m_0}}_{W(k)}\Bigg)u_{nk}(\boldsymbol{r})=Eu_{nk}(\boldsymbol{r})$$

Thus we can take the k-dependant part $W(\boldsymbol{k})$ as our perturbation and using some simple results from none degenerate perturbation theory [51, 31] we can approximate the eigenvalues ε_n and eigenfunctions $|\psi\rangle$ to second order as:

$$\varepsilon_n\approx\varepsilon_n^0+\Delta\varepsilon_n^1+\Delta\varepsilon_n^2 \quad (47)$$

$$|\psi\rangle\approx|n\rangle+\sum_{m\neq n}\frac{\langle n|W|m\rangle}{\varepsilon_n-\varepsilon_m}\,|m\rangle \quad (48)$$

Where $\Delta\varepsilon_n^1$ and $\Delta\varepsilon_n^2$ are the first and second order corrections to the energy given by:

$$\Delta\varepsilon_n^1\approx\ \langle n|W|n\rangle \quad (49a)$$

$$\Delta\varepsilon_n^2\approx\frac{|\,\langle n|W|m\rangle|^2}{\varepsilon_n^0-\varepsilon_m^0} \quad (49b)$$

At this point, we note that these perturbation corrections rely on diagonal matrix elements and thus the interaction of each band with every other band in the system. As we in principle would need to include an infinite number of bands (which is computationally impractical at best) we need a way to reduce the number of bands and parameters required for the calculation. Fortunately, two factors work in our favour:

1. The influence of remote bands is weak and scales proportionally with distance. Thus we can neglect many of the highest conduction and lowest valence bands without losing too much in the way of accuracy.

2. Due to orbital symmetries many of the inter-band interactions are equal to zero with only a small number leading to non-zero values, this drastically reduces the number of inter-band matrix elements required for computation.

Thus in our system, we will initially consider the so-called Kane model [52]. This consists of 4 bands (doubling to 8 with the inclusion off spin) the lowest conduction band and the three highest valance bands. The so-called heavy hole, light hole and split off bands (see Figure 9). We will later extend this model to include two higher lying conduction bands and the effects of mechanical strain (giving a total of 14 bands with the inclusion of spin see Figure 11). However for now to continue, we need to take a brief diversion to cover the symmetry properties of the included bands.

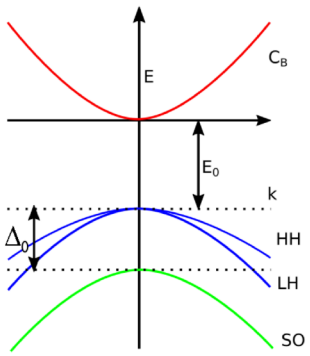

Figure 9: Diagram of III-V semiconductior bands near Γ point used in the Kane model.

3.1 Symmetry properties of Eigenfunctions

The bands in semiconductors originate from the overlap of the atomic orbitals categorising the outermost atomic shells which consist of sp^3 hybridisation states and the bands they form are described by combinations of these p and s-like states.

For a direct band-gap semiconductor (e.g. GaAs) at the Γ point the conduction band has an s-like symmetry, whilst the 3 valance bands take their symmetry from linear combinations of the three orthogonal p orbitals p_x, p_y, and p_z (see Figure 10).

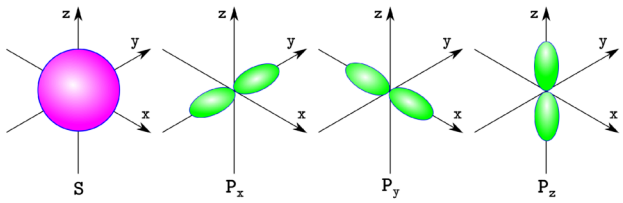

Figure 10: Diagram to show the shapes and symmetries of the sp^3 orbitals. The S orbital is spherical and hence symmetric in along all three axes whilst the three p-type orbitals are anti-symmetric along the direction of orientation.

If we look at the shape of these atomic orbitals, we can get a better understanding of the symmetries involved. Figure 10 shows the shapes of the four different possible orbitals. The s orbital is spherical and therefore symmetric about all three axes the three p orbitals, however, are anti-symmetric along their axis of orientation. This is useful if we consider the momentum matrix element between Bloch functions from s-like states (u_s) and p-like states (u_i where $i = x, y, z$) from which we can gain four key pieces of information:

1. $\langle u_s|u_i\rangle = 0$ which arises from the fact the p orbitals are all odd functions along their respective axis whilst the s orbital is even along all 3 axis, thus the interaction produces an odd function which vanishes when integrated over all space.

2. $\langle u_s|\boldsymbol{p}|u_i\rangle = \langle u_s|p_i|u_i\rangle = P$ since the momentum operator is given by $\boldsymbol{p} = -i\hbar(\frac{\partial X}{\partial x} + \frac{\partial Y}{\partial y} + \frac{\partial Z}{\partial z})$ which along any axis makes odd functions even, since it is the derivative of that function. Thus the operator does not vanish but is instead defined as the constant P (the value of which is material dependant can be obtained by fitting to experimental data).

3. $\langle u_s|p_i|u_j\rangle = 0$ for $j \neq i$ this is an extension of point 2

4. $\langle u_s \uparrow|\boldsymbol{p}|u_i \downarrow\rangle = \langle u_s \downarrow|\boldsymbol{p}|u_i \uparrow\rangle = 0$ since opposite spin states do not interact.

The exact combinations of orbitals we use to form our bands depend upon the basis we choose. However the spin-orbit interaction is non-zero and mixes the spin states $|\sigma\rangle$ so if we were to simply use the Bloch functions we have already defined ($|v\sigma\rangle$ where $v = u_s, u_x, u_y, u_z$ and $\sigma = \uparrow, \downarrow$) the Hamiltonian at $k = 0$ will contain off-diagonal terms which will make the calculations much more involved. Thus for convenience, we will use the same so-called "intelligent" basis used by Kane[52]. In this basis, Kane deliberately chose combinations of orbitals such that the total angular momentum $J = L + \sigma$ at the Γ point will be diagonal and thus the Hamiltonian H_0 will be diagonal allowing us to solve it exactly.

For our s-like state u_s $L = 0 \rightarrow J = 1/2$ and for the three p-like states u_x, u_y and u_z: $L = 1 \rightarrow J = 3/2$ or $1/2$. Thus our conduction band (u_c) and three valence band states (u_{HH}, u_{LH}, and u_{SO}) may be written as the following simple linear combinations of our Bloch functions. [53, 8, 50].

$$u_c \uparrow = |u_s \uparrow\rangle \, , u_c \downarrow = |u_s \downarrow\rangle \tag{50a}$$

$$u_{HH} \uparrow = -\tfrac{1}{\sqrt{2}}(|u_x \uparrow\rangle + i\,|u_y \uparrow\rangle) \tag{50b}$$

$$u_{HH} \downarrow = \tfrac{1}{\sqrt{2}}(|u_x \downarrow\rangle - i\,|u_y \downarrow\rangle) \tag{50c}$$

$$u_{LH} \uparrow = -\tfrac{1}{\sqrt{6}}(|u_x \uparrow\rangle + i\,|u_y \uparrow\rangle - 2\,|u_z \downarrow\rangle) \tag{50d}$$

$$u_{LH} \downarrow = \tfrac{1}{\sqrt{6}}(|u_x \downarrow\rangle + i\,|u_y \downarrow\rangle - 2\,|u_z \uparrow\rangle) \tag{50e}$$

$$u_{SO} \uparrow = -\tfrac{1}{\sqrt{3}}(|u_x \uparrow\rangle + i\,|u_y \uparrow\rangle + |u_z \uparrow\rangle) \tag{50f}$$

$$u_{SO} \downarrow = \tfrac{1}{\sqrt{3}}(|u_x \downarrow\rangle + i\,|u_y \downarrow\rangle + |u_z \downarrow\rangle) \tag{50g}$$

Finally we must consider the band energies at Γ point in our case we will take the energy at the bottom of the conduction band to be 0, this means the degenerate heavy and light hole bands will have energy $E_v = -E_0$ where E_0 is the direct band gap of the material and the split-off band will have energy $E_{so} = -E_0 - \Delta_0$ (see Figure 9). These can all be determined experimentally and thus can be used as input parameters alongside P. Using this information, we can now construct the Hamiltonian for the system

$$H_{8\times 8} = \begin{pmatrix} H_c & H_{cv} \\ H_{vc} & H_v \end{pmatrix} \tag{51}$$

where H_c, H_v and H_{cv} are matrix blocks the explicit form of which can be found in Appendix A.

Finally using equations (47) to (49) we can now calculate the n^{th} eigenvalue of equation (46) as:

$$\varepsilon_n(k) = \frac{\hbar^2 k^2}{2m_0^2} + \frac{\hbar^2}{m_0^2} \sum_{m \neq n} \frac{|\langle u_n(0,r)|\boldsymbol{k}\cdot\boldsymbol{p}|u_m(0,r)\rangle|^2}{\varepsilon_n(0) - \varepsilon_m(0)} \tag{52}$$

Thus we can compute the eigenvalues corresponding to the conduction and valence band

dispersions as:

$$\varepsilon_c(k) = \frac{\hbar^2 k^2}{2m_0} + \frac{k^2 P^2}{3}\frac{(3E_0+2\Delta)}{E_0(E_0+\Delta)} = \frac{\hbar^2 k^2}{2m_c^*} \tag{53a}$$

$$\varepsilon_{HH}(k) = -E_0 + \frac{\hbar^2 k^2}{2m_0} \tag{53b}$$

$$\varepsilon_{LH}(k) = -E_0 + \frac{\hbar^2 k^2}{2m_0} - \frac{2k^2 P^2}{3E_0} = -E_0 - \frac{\hbar^2 k^2}{2m_{LH}^*} \tag{53c}$$

$$\varepsilon_{so}(k) = -E_0 - \Delta + \frac{\hbar^2 k^2}{2m_0} - \frac{k^2 P^2}{3E_0+\Delta} = -\ E_0 - \Delta - \frac{\hbar^2 k^2}{2m_{so}^*} \tag{53d}$$

It should be noted however that this model gives an incorrect band dispersion for the heavy holes as experimental measurements show it should curve downwards, analogous to that of the light hole but with an effective mass of $m_h^* h$ (see Figure 9). This anomaly can be overcome by the inclusion of coupling with distant bands we can do this by following the method laid out by Pfeffer and Zawadzki [54] in which they adapted the 8×8 Kane model to include two additional conduction bands, one doubly and the other quadruply degenerate making a total of 6 extra bands with spin (the so called extended Kane model[8, 53]). Alongside this, they modified the valance band part of the Hamiltonian to include the effects of even more distant bands using a method developed by Luttinger and Kohn [55] which makes use of the Löwdin perturbation method[53] (also called Löwdin partitioning) to include far band effects using so called Luttinger parameters.

3.2 The extended Kane Model

To extend our existing Hamiltonian (and hence increase the accuracy of our calculations) we can include the effects of two additional conduction bands. To do this, we'll introduce some new notation borrowed from group theory [8]. Thus the lowest conduction band doublet is denoted as Γ_{6c}, the heavy/light hole quadruplet is Γ_{8v}, and the split off doublet is Γ_{7v}. The two new bands will be denoted as the doublet Γ_{7c}, which has energy minimum E_1 and the quadruplet Γ_{8c} which has its minimum at $E_1 + \Delta_1$ (see Figure 11).

These bands have p-like symmetry similar to that of the valence bands. Thus we can extend our "intelligent" basis using the Bloch functions u'_x, u'_y and u'_z to obtain similar basis functions and energies which are given in table 1. Finally in addition to P we have 3 new non-zero matrix elements:

1. $\frac{i\hbar}{m_0}\langle u_s|\boldsymbol{p}|u'_i\rangle = \frac{i\hbar}{m_0}\langle u_s|p'_i|u'_i\rangle = P_1$
2. $\frac{\hbar}{m_0}\langle u_x|p_y|u'_z\rangle = -\frac{\hbar}{m_0}\langle u'_x|p_y|u_z\rangle = Q$
   along with all other equivalent combinations e.g: $\langle u_y|p_x|u'_z\rangle$

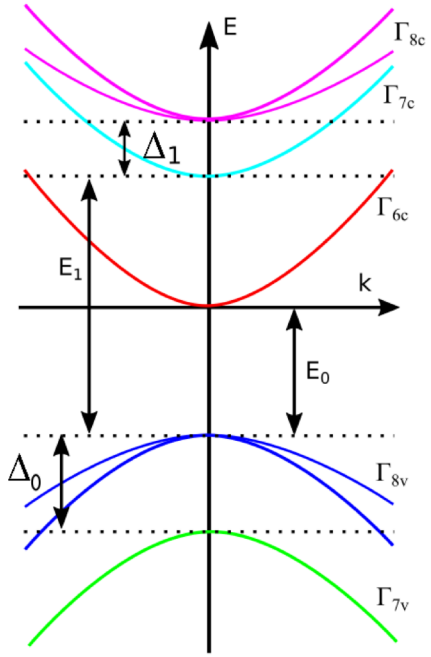

Figure 11: Diagram of III-V semiconductor bands near Γ point used in the extended Kane model.

3. $\frac{3\hbar}{4m_0^2c^2}\langle u_x|[\boldsymbol{\nabla V_0}\times\boldsymbol{p}]_y|u'_z\rangle = -\frac{3\hbar}{4m_0^2c^2}\langle u'_x|[\boldsymbol{\nabla V_0}\times\boldsymbol{p}]_y|u_z\rangle = \Delta^-$
and again with all other equivalent combinations e.g: $\frac{3\hbar}{4m_0^2c^2}\langle u_y|[\boldsymbol{\nabla V_0}\times\boldsymbol{p}]_x|u'_z\rangle$

Once again these are material dependant and have been determined by fitting to experimental data thus we can use them as inputs into the calculations in the same manner as P and the energies at the Γ point.

Thus we can build a 14×14 Hamiltonian for the system

$$H_{14\times14} = \begin{pmatrix} H_c & H_{cv} & H_{cc'} \\ H_{vc} & H_v & H_{vc'} \\ H_{c'c} & H_{c'v} & H_{c'} \end{pmatrix}$$

where H_c, H_v and H_{cv} are the same matrix blocks used in the original 8×8 Kane model which in addition to $H_{c'}$, $H_{v'c}$ and $H_{cc'}$ are again given explicitly in Appendix A.

3.3 The Luttinger-Kohn Method

The final part of the method laid out by Pfeffer and Zawadzki [54] involves the inclusion of the so called Luttinger Hamiltonian for the valence bands. This is a modification to the $\boldsymbol{k}\cdot\boldsymbol{p}$

Band	Basis function	Energy
Γ_{6c}	$\|u_c\uparrow\rangle$	0
	$\|u_c\downarrow\rangle$	0
Γ_{8v}	$-\frac{1}{2}\|(u_x+iu_y)\uparrow\rangle$	$-E_0$
	$\frac{1}{2}\|(u_x+iu_y)\downarrow\rangle$	$-E_0$
	$\sqrt{\frac{2}{3}}\|u_z\uparrow\rangle-\frac{1}{\sqrt{6}}\|(u_x+iu_y)\downarrow\rangle$	$-E_0$
	$\sqrt{\frac{2}{3}}\|u_z\downarrow\rangle+\frac{1}{\sqrt{6}}\|(u_x+iu_y)\uparrow\rangle$	$-E_0$
Γ_{7v}	$-\frac{1}{\sqrt{3}}\|u_z\uparrow\rangle-\frac{1}{\sqrt{3}}\|(u_x+iu_y)\downarrow\rangle$	$-(E_0+\Delta_0)$
	$\frac{1}{\sqrt{3}}\|u_z\downarrow\rangle-\frac{1}{\sqrt{3}}\|(u_x+iu_y)\uparrow\rangle$	$-(E_0+\Delta_0)$
Γ_{8c}	$-\frac{1}{2}\left\|(u'_x+iu'_y)\uparrow\right\rangle$	$E_1-E_0+\Delta_1$
	$\frac{1}{2}\left\|(u'_x+iu'_y)\downarrow\right\rangle$	$E_1-E_0+\Delta_1$
	$\sqrt{\frac{2}{3}}\|u'_z\uparrow\rangle-\frac{1}{\sqrt{6}}\left\|(u'_x+iu'_y)\downarrow\right\rangle$	$E_1-E_0+\Delta_1$
	$\sqrt{\frac{2}{3}}\|u'_z\downarrow\rangle+\frac{1}{\sqrt{6}}\left\|(u'_x+iu'_y)\uparrow\right\rangle$	$E_1-E_0+\Delta_1$
Γ_{7c}	$-\frac{1}{\sqrt{3}}\|u'_z\uparrow\rangle-\frac{1}{\sqrt{3}}\left\|(u'_x+iu'_y)\downarrow\right\rangle$	E_1-E_0
	$\frac{1}{\sqrt{3}}\|u'_z\downarrow\rangle-\frac{1}{\sqrt{3}}\left\|(u'_x+iu'_y)\uparrow\right\rangle$	E_1-E_0

Table 1: Basis functions/energies for 14-band $\boldsymbol{k}\cdot\boldsymbol{p}$ model [8]

Hamiltonian and involves a different approach to the problem of interactions with far bands. Instead of ignoring the effects of far bands Luttinger proposed separating out the bands of interest (in our case the 6 valence bands) in order to treat them exactly whilst treating the interactions with all other bands as a perturbation.

Thus in the intelligent basis used in table 1 we can replace the 6×6 matrix H_v with the 6×6 Luttinger-Kohn Hamiltonian given by:[55, 56, 57]

$$H_{LK}=-\begin{pmatrix} P+Q & -S & R & 0 & -\frac{S}{\sqrt{2}} & \sqrt{2}R \\ -S^+ & P-Q & 0 & R & -\sqrt{2}Q & \sqrt{\frac{3}{2}}S \\ R^+ & 0 & P-Q & S & \sqrt{\frac{3}{2}}S^+ & \sqrt{2}Q \\ 0 & R^+ & S^+ & P+Q & -\sqrt{2}R^+ & -\frac{S^+}{\sqrt{2}} \\ -\frac{S^+}{\sqrt{2}} & -\sqrt{2}Q^+ & \sqrt{\frac{3}{2}}S & -\sqrt{2}R & P+\Delta_{so} & 0 \\ \sqrt{2}R^+ & \sqrt{\frac{3}{2}}S^+ & \sqrt{2}Q^+ & -\frac{S^+}{\sqrt{2}} & 0 & P+\Delta_{so} \end{pmatrix} \tag{54}$$

Where

$$P = \frac{\hbar^2\gamma_1^L}{2m_0}(k_x^2 + k_y^2 + k_z^2)$$
$$Q = \frac{\hbar^2\gamma_2^L}{2m_0}(k_x^2 + k_y^2 - 2k_z^2)$$
$$R = \frac{\hbar^2}{2m_0}[-\sqrt{3}\gamma_2^L(k_x^2 + k_y^2) + 2i\sqrt{3}\gamma_3^L k_x k_y]$$
$$S = \frac{\hbar^2\gamma_3^L}{m_0}\sqrt{3}(k_x - ik_y)k_z$$

The constants γ_1^L, γ_2^L and γ_3^L are know as Luttinger parameters and can be expressed using momentum matrix elements as:

$$-\frac{\hbar^2}{2m_0}\gamma_1^L = \frac{1}{3}(L + 2M)$$
$$-\frac{\hbar^2}{2m_0}\gamma_2^L = \frac{1}{6}(L - M)$$
$$-\frac{\hbar^2}{2m_0}\gamma_3^L = \frac{N}{6}$$

where

$$L = \frac{\hbar^2}{2m_0} + \frac{\hbar^2}{m_0^2}\sum_j \frac{|\langle u_x|P_x|u_j\rangle|^2}{E_p - E_j}$$
$$M = \frac{\hbar^2}{2m_0} + \frac{\hbar^2}{m_0^2}\sum_j \frac{|\langle u_x|P_y|u_j\rangle|^2}{E_p - E_j}$$
$$N = \frac{\hbar^2}{2m_0}\sum_j \frac{\langle u_x|P_x|u_j\rangle\langle u_j|P_x|u_y\rangle + \langle u_x|P_y|u_j\rangle\langle u_j|P_x|u_y\rangle}{E_p - E_j}$$
$$E_p = \frac{2m_0}{\hbar^2}\boldsymbol{p}^2$$

In practice, however, the Luttinger parameters have been experimentally determined for a number of materials using cyclotron resonance [58]. Thus they are used as inputs in the same manner as the band energies (E_0, E_1, Δ_0 and Δ_1) and Kane parameters (P, P_1, Q and Δ^-) from the previous sections. There is however one more modification required to adapt the 14×14 extended Kane Hamiltonian. Due to the explicit inclusion of the 8 condition bands in the Hamiltonian we will need to modify the Luttinger parameters using Equations (58)a-c[54, 53].

$$\gamma_1 = \gamma_1^L + \frac{2m_0}{\hbar^2}\frac{P^2}{3E_0} - \frac{2m_0}{\hbar^2}\frac{Q^2}{3(E_1)} - \frac{2m_0}{\hbar^2}\frac{Q^2}{3(E_1+\Delta_1)} \tag{58a}$$
$$\gamma_2 = \gamma_2^L + \frac{2m_0}{\hbar^2}\frac{P^2}{6E_0} + \frac{2m_0}{\hbar^2}\frac{P^2}{6(E_1)} \tag{58b}$$
$$\gamma_3 = \gamma_3^L + \frac{2m_0}{\hbar^2}\frac{P^2}{6E_0} - \frac{2m_0}{\hbar^2}\frac{5Q^2}{9E_1} \tag{58c}$$

3.4 Adaptation for Semiconductor Hetrostructures

Thus far we have only dealt with the case of bulk material. However, the $\boldsymbol{k}\cdot\boldsymbol{p}$ method has been shown to be easily adapted to nanoscale Heterostructures such as quantum wells using the envelope function approximation (EFA). This can be seen as a generalisation of the $\boldsymbol{k}\cdot\boldsymbol{p}$ method in which we have electric or magnetic fields that are slowly varying on the length scale of the semiconductor lattice. Figure 12 shows a simple quantum well consisting of two lattice-matched materials A and B grown in the [001] direction (z-direction) with an external electric field $V_{ext}(z)$ oriented in the direction of the well. The band energies E_0, E_1, Δ_0 and Δ_1 and Luttinger parameters will now be position dependent and behave like step functions as we move from one material to another. We will also have a position-dependent potential $V(z) = V_{ext}(z) + E_c(z)$ where E_c is the position-dependent band edge profile forming the QW in the conduction band. The general Schrödinger equation for this system is given by:

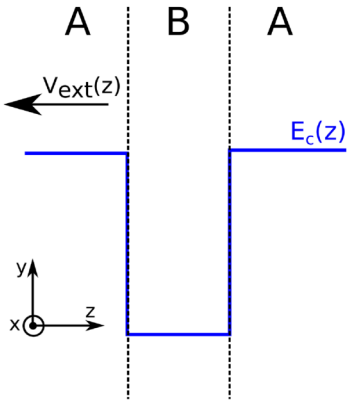

Figure 12: Diagram of quantum well formed in the conduction band of a heterojunction between two lattice matched materials A and B.

$$H\psi(r) = \left(\frac{i\hbar\boldsymbol{\nabla}^2}{2m_0} + U(r) + \frac{\hbar}{4m_0^2c^2}[\boldsymbol{\nabla}V \times \boldsymbol{p}\cdot\boldsymbol{\sigma}] + V(z)\right)\psi(r) = E\psi(r) \tag{59}$$

where $\boldsymbol{p} = -i\hbar\boldsymbol{\nabla}$ and $U(r)$ is the periodic potential of the lattice and obeys $U(r) = U(r+R)$ for all vectors R of the direct lattice.

The Envelope function theory states that wavefunction in each material can be expanded on the periodic parts of the Bloch function as[50, 53]:

$$F_j(\boldsymbol{r}) = \sum_j F_j(\boldsymbol{r})u_{j0} \tag{60}$$

where: $\boldsymbol{r}$ is the position in real space, σ represents the spin eigenstates $(\uparrow, \downarrow)$, $F_j(\boldsymbol{r})$ are slowly varying envelope functions, u_{j0} are the periodic part of the Bloch functions at $\boldsymbol{k} = 0$ and j is an index that runs across all included bands.

For our case though, we have a wavefunction in each material A and B thus

$$\psi_A(\boldsymbol{r}) = \sum_j F_j^A(\boldsymbol{r}) u_{j0}^A$$
$$\psi_B(\boldsymbol{r}) = \sum_j F_j^B(\boldsymbol{r}) u_{j0}^B$$

However since the periodic Bloch functions are assumed to be the same in each material (i.e. $u_{j0}^A = u_{j0}^B$) the heterostructure wavefunction can be written as:

$$\psi_{A,B}(\boldsymbol{r}) = \sum_j F_j^{A,B}(\boldsymbol{r}) u_{j0} \tag{61}$$

we can make a further observation that if $u_{j0}^A = u_{j0}^B$ is true the inter-band matrix element p_x from $\langle S| \, p_x \, |X\rangle$ must be the same in both materials and if we also assume the lattice constants of the two materials are the same thus the envelope is invariant under translation in the layer $(x - y)$ plane thus it can be re-written as:

$$F_j^A(\boldsymbol{r}) = F_j^A(\boldsymbol{r}_\perp, z) = \tfrac{1}{\sqrt{S}} \exp(i\boldsymbol{k}_\perp \cdot \boldsymbol{r}_\perp) \chi_j^A(z) \tag{62}$$
$$F_j^B(\boldsymbol{r}) = F_j^B(\boldsymbol{r}_\perp, z) = \tfrac{1}{\sqrt{S}} \exp(i\boldsymbol{k}_\perp \cdot \boldsymbol{r}_\perp) \chi_j^B(z) \tag{63}$$
$$F_j^{A,B}(\boldsymbol{r}) = F_j^{A,B}(\boldsymbol{r}_\perp, z) = \tfrac{1}{\sqrt{S}} \exp(i\boldsymbol{k}_\perp \cdot \boldsymbol{r}_\perp) \chi_j^{A,B}(z) \tag{64}$$

Where S is the sampled area and $\boldsymbol{k}_\perp = (k_x, k_y)$ and is assumed to be the same in both layers A and B.

By substituting equation (61) into 59 multiplying the left hand side by u_{j0}^* and integrating over one unit cell (of volume Ω) we obtain the eigenvalue problem:

$$\sum_j \left(\left[\varepsilon_{0j} - E + \tfrac{\boldsymbol{p}_z}{2m_0} + \tfrac{\hbar^2 k_\parallel^2}{2m_0} \right] \delta_{jj'} + \frac{1}{m_0} \left(\boldsymbol{p}_z + \tfrac{\hbar k_\parallel}{m_0} \right) \cdot \pi_{jj'} \right) \chi_j^{A,B}(z) = 0 \tag{65}$$

where: ε_{0j} is the band edge energy at the Γ point for the j^{th} band, $\delta_{jj'}$ is the Kronecker delta and

$$\pi_{jj'} = \frac{1}{\Omega} \int_\Omega u_{j'}^*(r) \left[\boldsymbol{p} + \tfrac{\hbar\sigma \times \boldsymbol{\nabla} V(r)}{4m_0 c^2} \right] u_j(r) d^3 r \approx \boldsymbol{p}_{jj'}$$

Finally, in order to solve for the 14 envelope functions $\chi_j(r)$ and (ultimately calculate the band structure for the quantum well) we need the 14×14 system Hamiltonian. Bastard

showed, [59] that if we assume the envelope functions are continuous at the A-B interface the system Hamiltonian can be found by making a few small changes from the bulk $\boldsymbol{k}\cdot\boldsymbol{p}$ Hamiltonian given by equation (3.2) these are [50, 53, 60]:

1. The addition of the potential $V(z)$ on the diagonal
2. The substitution of $k_z \to -i\frac{\partial}{\partial z}$.

Thus we have all the information we need to obtain the 14 coupled differential equations needed to calculate the 14 wave-functions and thus the bandstructure for the system.

3.5 Calculation of Rashba and Dresselhaus constants

Finally, we would like to estimate the constants associated with the D'yakonov-Perel mechanism for spin-orbit coupling, i.e. The so-called Dresselhaus and Rashba material dependent constants associated with bulk and structural inversion asymmetry respectively (see section 2.4.2 for more information).

We start with an asymmetric quantum well with the growth direction z taken as the [001] crystallographic direction similar to the example used in the previous section. The Hamiltonian corresponding to the conduction band can be approximated as the following[8]:

$$\tilde{H}_c = H_c - H_{ur}(H_{lr} - E)^{-1}H_{ll} \tag{66}$$

where

$$H_{ur} = \begin{pmatrix} H_{cc}^T & H_{cc'}^T \end{pmatrix}$$
$$H_{ll} = \begin{pmatrix} H_{cv} & H_{cc'} \end{pmatrix}$$
$$H_{lr} = \begin{pmatrix} H_v & H_{vc'} \\ H_{c'c} & H_{c'} \end{pmatrix}$$

with all other matrix blocks having the same definitions given in Equation (3.2).

The matrix inversion $(H_{lr} - E)^{-1}$ can be simplified by making the decomposition $(H_c - E) = A - D$, where A is a matrix with diagonal elements equal to the those of $H_{lr} - E$ and D is a matrix whose off-diagonal elements are equal to those of $H_{lr} - E$. Thus, $H_c - E = A(1_{12\times 12} - A^{-1}D)$ and therefore:

$$(H_{lr} - E)^{-1} = (1_{12\times 12} - A^{-1}D)^{-1}A^{-1} \approx \left[(1_{12\times 12} - A^{-1}D)^{-1}(A^{-1}D)^2 + (A^{-1}D)^3 \dots\right]A^{-1}$$

Thus keeping the expansion up to second order we obtain:

$$(H_{lr} - E)^{-1} \approx A^{-1} + A^{-1}DA - 1 + (A^{-1}D)^2 A^{-1} \tag{67}$$

where:

$$A = \begin{pmatrix} H_v - E & 0 \\ 0 & H_{c'} - E \end{pmatrix} \quad \text{and} \quad D = -\begin{pmatrix} 0 & H_{vc'} \\ H_{c'v} & 0 \end{pmatrix}$$

Finally, using equations (66) and (67) we obtain the approximate Hamiltonian for the two conduction bands

$$\tilde{H}_c = -\frac{\hbar^2}{2}\frac{\partial}{\partial z}\left[\frac{1}{m^*(z,E)}\frac{\partial}{\partial z}\right] + \frac{\hbar^2 k_\parallel^2}{2m^*(z,E)} + V(z) + H_{BR} + H_D + H'_D \tag{68}$$

where

$$\frac{1}{m^*(z,E)} = \frac{1}{m_0} + \frac{2P^2}{3\hbar^2}\left(\frac{2}{E_v(z)-E} + \frac{1}{E_{so}(z)-E}\right) - \frac{2P_1^2}{3\hbar^2}\left[\frac{1}{E_{c'}(z)-E} + \frac{2}{G_{c'}(z)-E}\right] - \frac{8P_1 P\Delta^-}{9\hbar^2}\left[\frac{1}{E_{c'}(z)E_{so}(z)-E} - \frac{1}{E_v(z)G_{c'}(z)-E}\right]$$

with

$$E_v(z) = E_c(z) - E_0(z) + V_{ext}(z), \qquad E_{so}(z) = E_v(z) - \Delta_0(z)$$
$$E_{c'}(z) = E_c(z) + [E_1(z) - E_c(z)], \qquad G_{c'}(z) = E_{c'}(z) + \Delta_1(z)$$

The terms H_{BR} and H_D correspond to the Rashba and Dresselhaus spin orbit interactions and are given by:

$$H_{BR} = \alpha_{BR}(z)(k_x\sigma_y - k_y\sigma_x) \tag{69}$$

$$H_D = (k_x\sigma_x - k_y\sigma_y)\frac{\partial}{\partial z}\left(\gamma(z)\frac{\partial}{\partial z}\right) \tag{70}$$

$$H'_D = i(k_y^2 - k_x^2)\sigma_z\left[\frac{1}{2}\frac{\mathrm{d}\gamma(z)}{\mathrm{d}z} + \gamma(z)\frac{\mathrm{d}}{\mathrm{d}z}\right] + \gamma(z)(k_y\sigma_x - k_x\sigma_y)k_x k_y \tag{71}$$

with the material dependant spin orbit coupling parameters α_{BR} and γ being given by:

$$\alpha_{BR}(z) = \frac{\mathrm{d}\beta(z)}{\mathrm{d}z}$$

$$\beta(z) = \frac{P^2}{3}\left(\frac{1}{E_v(z)-E} - \frac{1}{E_{so}(z)-E}\right) + \frac{P_1^2}{3}\left(\frac{1}{G_{c'}(z)-E} - \frac{1}{E_{c'}(z)-E}\right) + \frac{2PP_1\Delta^-}{9}\left(\frac{1}{E_v(z)G_{c'}(z)-E} + \frac{2}{E_{c'}(z)E_{so}-E}\right)$$

$$\gamma(z) = \frac{4P_1PQ}{3}\left(\frac{1}{E_v(z)E_{c'}(z)-E} - \frac{1}{E_{so}(z)G_{c'}(z)-E}\right)+ \frac{4Q\Delta^-}{9}\left[\frac{P_1^2}{E_{c'}(z)G_{c'}(z)-E}\left(\frac{1}{E_v(z)-E} + \frac{2}{E_{so}(z)-E}\right) - \frac{P^2}{E_v(z)E_{so}(z)-E}\left(\frac{2}{E_{c'}(z)-E} + \frac{1}{G_{c'}(z)-E}\right)\right]$$

These can then be further simplified by noting that a general function of the form $\frac{1}{x-y} - \frac{1}{x-y-z}$ can be approximated as the following series

$$\frac{1}{x-y} - \frac{1}{x-y-z} = \sum_{n=0}^{n=\infty}\left(\frac{1}{(y+z)^n} - \frac{1}{y^n}\right)x^n$$

Therefore by remembering the definitions (and dependence on V_{ext}) of E_v and E_{so}, and taking the zero of energy to be the bottom of the conduction band (i.e. $E_c = 0$) we can express the equations for α_{BR} and γ to first order as

$$\begin{aligned}\alpha_{br}(z) = \frac{1}{3}\left[\frac{P^2}{(E_0+\Delta_0)^2} - \frac{P^2}{E_0^2} + \frac{P_1^2}{E_1^2} - \frac{P_1^2}{(E_1+\Delta_1)^2}\right]\frac{\mathrm{d}V_{ext}}{\mathrm{d}z} \\ -\frac{2P_1P\Delta^-}{9}\left[\frac{1}{E_1(E_1+\Delta_1)^2} - \frac{1}{E_0^2(E_1+\Delta_1)} - \frac{2}{E_1(E_0+\Delta_0)^2} + \frac{2}{E_1^2(E_0+\Delta_0)}\right]\frac{\mathrm{d}V_{ext}}{\mathrm{d}z}\end{aligned} \tag{72}$$

$$\begin{aligned}\gamma(z) = \frac{4PP_1Q}{3}\left[\frac{1}{E_0E_1} - \frac{1}{(E_0+\Delta_0)(E_1+\Delta_1)}\right] - \frac{4P^2Q\Delta^-}{9E_0(E_0+\Delta_0)}\left[\frac{2}{E_1} + \frac{1}{E_1+\Delta_1}\right] \\ -\frac{4P_1^2Q\Delta^-}{9E_1(E_1+\Delta_1)}\left[\frac{1}{E_0} + \frac{2}{E_1+\Delta_0}\right]\end{aligned} \tag{73}$$

3.6 Overview

In this chapter we have presented the mathematics of the $\boldsymbol{k}\cdot\boldsymbol{p}$ technique for calculating electronic bandstructures in bulk semiconductors, its adaptation for semiconductor heterostructures and the calculation of Rashba and Dresselhaus spin orbit coupling coefficients α_{br} and γ used in the density matrix model for the spin-orbit coupling. In the next chapter will cover the details of the Monte Carlo technique for device simulations.

4 Monte Carlo Simulations

The Monte Carlo method is a powerful simulation tool based on selections random numbers. The initial method is generally attributed to the work of Fermi and Von Neumann during the Manhattan project in which the technique was used in connection with neutron scattering. The procedure itself, however, is quite universal and was adopted in the late 1960's for use in semiconductor transport simulations [61]. The basic technique involves tracking the random motion of an ensemble of electrons as they move through a material; under the influence of an electric (or magnetic) field, and can be used to examine the effects of random scattering events, doping, material boundaries, heterojunctions and gates on the electron transport.

4.1 The Ensemble Monte Carlo Method

The basic principle of the ensemble Monte Carlo method for electron transport is to simulate the motion of an ensemble of carriers in momentum space. We will start by considering the motion of just one electron in an electric field over a time step τ. First the "free flight" time *tau* is determined using a random number generator. The electron is then allowed to drift in the field for this period after which it undergoes some scattering event, due to interactions with phonon's, ionised impurities etc. (see section 4.3). This whole process is then repeated until the total time t is greater than some time t_{max} at which point the simulation is halted (see figure 13a). The time τ is dependent upon the total scattering rate $\Gamma_T(E_k) = \sum_{j=1}^{N} \Gamma_j(E_k)$ where j is an integer subscript to denote the scattering mechanism, thus for N possible mechanisms we have $j = 1, 2, 3, \ldots, N$. Thus the probability of an electron travelling for a time τ and then being scattered $P(\tau)$ is[62]

$$P(\tau) = \Gamma_T(E_k) \exp\left(- \int_0^{\tau} \Gamma_T(E_k) dt \right). \tag{74}$$

Therefore, to determine τ for a given $P(\tau)$ using a random number r_1 we need to evaluate this integral, however, this is far from easy due to the complex forms that the various scattering mechanisms take. To simplify this problem and allow for an analytical solution to equation (74) we can employ a so-called "self-scattering" mechanism[62, 61]. This involves imputing a virtual scattering event which does not change the $\boldsymbol{k}$-vector of the electron but has a scattering rate Γ_0 such that the new total scattering rate Γ becomes constant, i.e. $\Gamma_0 = \Gamma - \sum_{j=1}^{N} \Gamma_j(E_k)$ and thus:

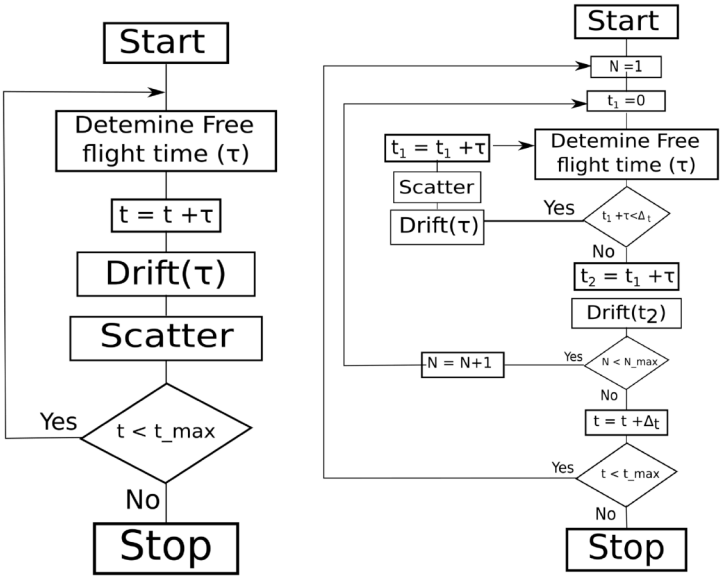

(a) Single particle method (b) Ensemble method

Figure 13: Flow charts to show the basic single particle and ensemble Monte Carlo method

$$P(\tau) = \Gamma e^{-\Gamma\tau} \tag{75}$$

The time τ can then be easily determined using a random number r_1 as:

$$\tau = -\frac{\ln(r_1)}{\Gamma} \tag{76}$$

In practice, it is important to consider the precise value of Γ since if it is too small, we will obtain a negative value for Γ_0 within the energy range of interest. However, if it is too large, we lose computational efficiency as we would be wasting CPU time self-scattering. Thus Γ is usually taken to be slightly larger than the largest value possible of $\Gamma_T(E_k)$[62].

Now that we have the case for a single particle the extension to an ensemble is fairly straightforward the main alteration to the method is that we now have to run the scatter and drift process over all the particles in the ensemble during a time step Δ_t. However, since the free flight time for each particle is determined at random, each electron has the potential to scatter more than once during each time step. Thus we begin by defining the time left in the time step as t_1 (which is initially $t_1 = 0$). For each particle N in the ensemble τ is determined and the value $\tau + t_1$ is compared to Δ_t. If this is less than Δ_t, then the process continues as before, whereby the electron drifts for time τ then scatters. At the end of the

scattering, however, the value of τ is added to t_1, and then τ is re-calculated for the next cycle. If however $\tau + t_1$ is greater than Δ_t the electron is allowed to drift for the remaining time $t_2 = \Delta_t - t_1$ after which the process moves to the next particle in the ensemble. Figure 13b shows a flowchart of the ensemble method which is repeated for each particle and for each time step until a time $t = t_{max}$ is reached.

Now that we have the basic method we will need to develop the free flight and scattering processes in more detail which will be the subject of the next two sub-sections.

4.2 Electron transport in a semiconductor crystal lattice

We recall from section 3 that for electrons in a periodic crystal lattice we can re-write the general Schrödinger equation using Bloch's Theorem as:

$$Hu_{nk}(r) \approx \left(\frac{\boldsymbol{p}^2}{2m_0} + U(\boldsymbol{r}) + \frac{\hbar}{4m_0^2c^2}\big[\boldsymbol{\nabla V} \times \boldsymbol{p}\big] \cdot \boldsymbol{\sigma} + \frac{\hbar}{m_0}\boldsymbol{k} \cdot \boldsymbol{p} + \frac{\hbar^2 k^2}{2m_0} \right) u_{nk}(r) = E u_{nk}(r), \quad (77)$$

where $\boldsymbol{p} = -i\hbar\boldsymbol{\nabla}$ and $U(r)$ is the periodic potential of the lattice and obeys
$U(\boldsymbol{r}) = U(\boldsymbol{r} + \boldsymbol{R})$ for all vectors $\boldsymbol{R}$ of the direct lattice.

This equation leads to the formation of energy bands with a characteristic separation of energy E_g between the lowest conduction band minima and the highest valence band maxima. For electron transport, however, only the region near the conduction band minima (and by extension the valence band maxima) needs to be considered to capture the necessary physics of the system. As such it is common to approximate the band dispersion $\varepsilon(\boldsymbol{k})$ using a quadratic function of $\boldsymbol{k}$ [61, 62]. For conduction band minima at the Γ point ($\boldsymbol{k} = 0$):

$$\varepsilon(\boldsymbol{k}) = \frac{\hbar^2 k^2}{2m^*} \quad (78)$$

where m^* is the effective mass given by:

$$\frac{1}{m^*} = \frac{1}{\hbar^2}\frac{\partial^2 \varepsilon(\boldsymbol{k})}{\partial \boldsymbol{k}^2}$$

For conduction band minima lying on the Λ or Δ lines

$$\varepsilon(\boldsymbol{k}) = \frac{\hbar}{2}\big(\frac{k_l^2}{2m_l^*} + \frac{k_t^2}{2m_t^*}\big) \quad (79)$$

where k_t and k_l represent the longitudinal and transverse components of $\boldsymbol{k}$ with respect to the valley direction whilst m_l^* and m_t^* are the longitudinal and transverse components of the effective mass.

For the valance bands, a similar procedure can be adopted for the light and heavy hole bands (the split-off band is not usually considered because of its energy separation and comparatively small density of states [61])

$$\varepsilon(\boldsymbol{k}) = \frac{\hbar}{2m_0}(Ak^2 \pm [B^2k^4 + C^2(k_x^2k_y^2 + k_y^2k_z^2 + k_z^2k_x^2)]^{1/2}) \tag{80}$$

where m_0 is the electron mass, $\pm$ represents the heavy and light hole bands respectively and the coefficients A, B and C are parameters determined from experimental data.

Aside: non-parabolic approximations For particularly high electric fields the carrier energy may be far from the band edge in which case we will need to switch to a non-parabolic approximation for $\varepsilon(k)$ which is given by [62]:

$$\varepsilon(\boldsymbol{k}) = \frac{\sqrt{1+4\alpha\gamma(\boldsymbol{k})}-1}{2\alpha} \tag{81}$$

where $\gamma(k) = \frac{\hbar^2k^2}{2m^*}$ and α is a material dependant constant given by $\alpha = \frac{1}{E_g}\left(1 - \frac{m^*}{m_0}\right)^2$

These dispersion relationships show us that electrons in a crystal behave just like free electrons only with the electron mass being replaced by the effective mass m^* and $\hbar\boldsymbol{k}$ playing the role of momentum (this is often referred to as the crystal momentum). Thus as long as the potential energy 'felt' by the electrons is slowly varying when compared to the crystal potential, we are able to ignore quantum effects such as tunnelling and we can use classical equations of motion to describe the electrons as they travel through the crystal.

If we take the total energy of the system $H = E_k + U$, where E_k and U are the kinetic and potential energies respectively. We can adapt this equation by making the kinetic energy $\boldsymbol{k}$-dependant and setting the potential as the conduction band minimum $E_c(\boldsymbol{r})$ given by:

$$E_c(\boldsymbol{r}) = E_{vac} - \chi(\boldsymbol{r}) - eV(\boldsymbol{r})$$

Where E_{vac} is the vacuum level $\chi(r)$ is the electron affinity and $V(r)$ is the electrostatic potential.

The equations of motion can thus be easily constructed as[62]:

$$\frac{\mathrm{d}\boldsymbol{k}}{\mathrm{d}t} = -\frac{1}{\hbar}\boldsymbol{\nabla}H \tag{82}$$

$$\frac{\mathrm{d}\boldsymbol{r}}{\mathrm{d}t} = \frac{1}{\hbar}\boldsymbol{\nabla}_k H \tag{83}$$

where $\boldsymbol{\nabla}$ and $\boldsymbol{\nabla}_k$ are the gradient operator for real and k-space respectively.

Thus for a conduction band minima at the gamma point (see equation (78)) the group velocity is given by:

$$\boldsymbol{v_g} = \frac{\hbar \boldsymbol{k}}{m^*} \tag{84}$$

and for minima along Λ or Δ (see equation (79)) we have:

$$\boldsymbol{v_g} = \frac{\hbar \boldsymbol{k_l}}{m_l^*} + \frac{\hbar \boldsymbol{k_t}}{m_t^*} \tag{85}$$

assuming the electron is travelling through a constant electric field $\boldsymbol{E}$ the work done $\delta\epsilon$ by the field in time interval δt is:

$$\delta\epsilon = -e\boldsymbol{E}\boldsymbol{v_g}\delta t$$

We now note that

$$\delta\epsilon = \frac{\mathrm{d}\epsilon}{\mathrm{d}k}\delta = \hbar \boldsymbol{v_g}\delta k$$

Thus we have

$$\delta k = -\left(\frac{e\boldsymbol{E}}{\hbar}\right)\delta t$$

which we can re-write in terms of the external force F as

$$\hbar\frac{\mathrm{d}\boldsymbol{k}}{\mathrm{d}t} = -e\boldsymbol{E} = \boldsymbol{F} \tag{86}$$

we can also include the effects of the Lorentz force from a constant weak magnetic field $\boldsymbol{B}$ as [51, 61, 62]

$$\hbar\frac{\mathrm{d}\boldsymbol{k}}{\mathrm{d}t} = -e(\boldsymbol{E} + \boldsymbol{v_g} \times \boldsymbol{B}) \tag{87}$$

4.3 Carrier Scattering: Basic Theory

Electron Scattering is important to consider when simulating electron transport though a semiconductor crystal lattice. The various scattering processes involved can a have a marked effect on the electron dynamics as the ensemble moves across the lattice. Thus in order to achieve a realistic device simulation that matches experimental observation the importance of scattering cannot be ignored. There are several different mechanisms by which scattering can occur (the physical origins of which will be discussed latter in this section). Quantum mechanically however, all forms of electron scattering can by regarded as a small perturbation H' to the electron Hamiltonian H_0 the effects of which can be accounted for using time dependant perturbation theory.

To derive the fist order approximation for transition the probability $P(\boldsymbol{k}, \boldsymbol{k'})$ between initial and final eigenstates $\boldsymbol{k}$ and $\boldsymbol{k'}$ due to a perturbation H', we must first introduce a real dimensionless parameter λ such that the time dependant Schödinger equation for the system can be re-written as [62]:

$$i\hbar\frac{\partial\psi(\boldsymbol{r},t)}{\partial t} = (H_0 + \lambda H')\psi(\boldsymbol{r},t) \tag{88}$$

If we now assume that the unperturbed Hamiltonian operator H_0 is simple and has a known solution given by:

$$H_0\psi_k = E_k\psi_k$$

where E_k are the eigenvalues with corresponding eigenfunctions ψ_k. We can re-write the time dependant solution as:

$$\psi_k^0(\boldsymbol{r},t) = \psi_k e^{-iE_kt/\hbar}$$

and since ψ_k^0 is a complete orthonormal set, we can express $\psi(r,t)$ as a linear combination of ψ_k^0, with coefficient $C_k(t)$ such that:

$$\psi(\boldsymbol{r},t) = \sum_{\boldsymbol{k}} C_k(t)\psi_k^0(\boldsymbol{r},t) = C_k(t)e^{-iE_kt/\hbar}$$

Substituting this into equation (88) gives:

$$i\hbar\sum_{\boldsymbol{k}}\frac{\partial C_k(t)}{\partial t}\psi_k(\boldsymbol{r})e^{-iE_kt/\hbar} = \lambda\sum_{\boldsymbol{k}} H'C_k(t)\psi_k(\boldsymbol{r})e^{-iE_kt/\hbar}$$

Finally multiplying both sides by $\psi_k^*(\boldsymbol{r})e^{iE_{k'}t/\hbar}$ and integrating over $\boldsymbol{r}$ gives us:

$$i\hbar\sum_{\boldsymbol{k}}\frac{\partial C_{k'}(t)}{\partial t} = \lambda\sum_{\boldsymbol{k}}\langle\boldsymbol{k'}|H'|\boldsymbol{k}\rangle\, C_k(t)e^{i[E'_k-E_k]t/\hbar} \tag{89}$$

To approximate the coefficient $C_k(t)$ we use a power series in λ[62]

$$C_k(t) = C_k^0 + \lambda C_k^1(t) + \lambda^2 C_k^2(t)\ldots$$

substituting this approximation up to second order into Equation (89) gives

$$i\hbar\left(\frac{\partial C_{k'}^0}{\partial t} + \lambda\frac{\partial C_{k'}^1(t)}{\partial t} + \lambda^2\frac{\partial C_{k'}^2(t)}{\partial t}\right) = \sum_{\boldsymbol{k}}\langle\boldsymbol{k'}|H'|\boldsymbol{k}\rangle\, e^{i[E'_k-E_k]t/\hbar}(\lambda C_k^0 + \lambda^2 C_k^1(t) + \lambda^3 C_k^2(t))$$

If we equate powers of λ on both sides we find

$$i\hbar\frac{\partial C^0_{k'}}{\partial t} = 0 \tag{90a}$$

$$i\hbar\frac{\partial C^1_{k'}(t)}{\partial t} = \sum_{\boldsymbol{k}} \langle \boldsymbol{k'}|H'|\boldsymbol{k}\rangle\, C^0_k e^{i[E'_k - E_k]t/\hbar} \tag{90b}$$

$$i\hbar\frac{\partial C^2_{k'}(t)}{\partial t} = \sum_{\boldsymbol{k}} \langle \boldsymbol{k'}|H'|\boldsymbol{k}\rangle\, C^1_k(t) e^{i[E'_k - E_k]t/\hbar} \tag{90c}$$

$$\vdots$$

From this we can see that the zero-order approximation of $C_k(t)$ (C^0_k) is constant in time and thus we can easily evaluate $C_k(t)$ to first order using using equation (90b). If we now consider the initial condition at $t = 0$ that all except one C^0_k are zero i.e. the electron is in a definite perturbed eigenstate k_i at $t = 0$ we have

$$C_{k'}(0) = C^0_{k_i} = 1$$
$$C_{k'}(0) = C^0_k = 0 \qquad (\boldsymbol{k} \neq \boldsymbol{k_i})$$

and

$$i\hbar\frac{\partial C_{k'}(t)}{\partial t} = \langle \boldsymbol{k'}|H'|\boldsymbol{k_i}\rangle\, e^{i(E_{k'} - E_{k_i})t/\hbar} \tag{91}$$

We now assume that H' depends harmonically on the time as

$$H'(t) = H' e^{\pm i\omega t}$$

(this is considered a valid assumption since even if it is not directly a harmonic dependence, it may be harmonic for one Fourier component of a more general function of time, see reference [62] for more details.)

Substituting this into equation (91) gives

$$i\hbar\frac{\partial C_{k'}(t)}{\partial t} = \langle \boldsymbol{k'}|H'|\boldsymbol{k_i}\rangle\, e^{i(E_{k'} - E_{k_i} \pm i\hbar\omega)t/\hbar}$$

Integration from 0 to t then gives

$$C_{k'}(t) = \frac{1}{i\hbar}\langle \boldsymbol{k'}|H'|\boldsymbol{k_i}\rangle \frac{e^{i(E_{k'} - E_{K_i} \pm \hbar\omega)t/\hbar} - 1}{i(E_{k'} - E_{k_i} \pm \hbar\omega)/\hbar} \tag{92}$$

This can then be re-written as

$$C_{k'}(t) = \frac{1}{i\hbar}\langle \boldsymbol{k'}|H'|\boldsymbol{k_i}\rangle\, e^{i\zeta t}\frac{\sin(\zeta t)}{\zeta t}t \tag{93}$$

where $\zeta = (E_{k'} - E_{k_i} \pm \hbar\omega)/2\hbar$.

Since probability of finding an electron with wave vector $\boldsymbol{k'}$ at time t is given by $|C_{k'}(t)|^2$ we can calculate the transition probability from a state $\boldsymbol{k_i}$ to $\boldsymbol{k'}$ per unit time (i.e. the transition rate) as

$$P(\boldsymbol{k_i}, \boldsymbol{k'}) = \frac{|C_{k'}(t)|^2}{t} = \frac{|\langle \boldsymbol{k'}|H'|\boldsymbol{k_i}\rangle|^2}{\hbar^2}\left[\frac{\sin(\zeta t)}{\zeta t}\right]^2 t \tag{94}$$

We now note that in the limit $t \to \infty$ the width of the function $[\frac{\sin(\zeta t)}{\zeta t}]^2$ becomes very small and can be approximated as a Dirac δ-function. Thus finally, using the identity

$$\int_{-\infty}^{\infty}\left[\frac{\sin(\zeta t)}{\zeta t}\right]^2 d\zeta = \frac{\pi}{t}$$

we can replace $[\frac{\sin(\zeta t)}{\zeta t}]^2$ by $\delta(\zeta)\pi/t$ and the transition rate can be written as

$$P(\boldsymbol{k}, \boldsymbol{k'}) = \frac{2\pi}{\hbar}|\langle \boldsymbol{k'}|H'|\boldsymbol{k_i}\rangle|^2\delta(E_{k'} - E_k \pm \hbar\omega) \tag{95}$$

For Monte Carlo calculations however we need the scattering rate Γ which can easily be found by integrating Equation (95) with respect to the final state $\boldsymbol{k'}$ to give

$$\Gamma(\boldsymbol{k}) = \frac{2\pi}{\hbar}\frac{\Omega}{(2\pi)^3}\int |\langle \boldsymbol{k'}|H'|\boldsymbol{k_i}\rangle|^2\delta(E_{k'} - E_k \pm \hbar\omega)d\boldsymbol{k'} \tag{96}$$

This is the well known Fermi Golden rule and is used in the Monte Carlo engine to calculate the probability that a scattering event has occurred during the time step δt. The precise from of H' is depends upon the scattering mechanism that is considered this will be the subject of the next section.

Aside: Form factor for non-parabolic approximations It should be noted that Equation (96) assumes the use of a parabolic band approximation. To adapt the equation for use with non-parabolic bands we need to introduce a overlap integral $G(\boldsymbol{k}, \boldsymbol{k'})$ (often called a form factor) into the matrix element $\langle \boldsymbol{k'}|H'|\boldsymbol{k_i}\rangle$ such that [61, 62],

$$\Gamma(\boldsymbol{k}) = \frac{2\pi}{\hbar}\frac{\Omega}{(2\pi)^3}\int |\langle \boldsymbol{k'}|H'|\boldsymbol{k_i}\rangle|^2|G(\boldsymbol{k}, \boldsymbol{k'})|^2\delta(E_{k'} - E_k \pm \hbar\omega)d\boldsymbol{k'} \tag{97}$$

for the parabolic case $G(\boldsymbol{k}, \boldsymbol{k'}) \approx 1$ and so is often neglected. For the non-parabolic case however, $|G(\boldsymbol{k}, \boldsymbol{k'})|^2$ can be approximated as [62, 61]

$$|G(\boldsymbol{k}, \boldsymbol{k'})|^2 = (a_{\boldsymbol{k}}a_{\boldsymbol{k'}} + b_{\boldsymbol{k}}b_{\boldsymbol{k'}}\cos(\theta))^2) \tag{98}$$

where θ is the angle between $\boldsymbol{k}$ and $\boldsymbol{k'}$ and $a_{\boldsymbol{k}}$ and $b_{\boldsymbol{k}}$ are given by

$$a_{\boldsymbol{k}} = \left[\frac{1+\alpha E(\boldsymbol{k})}{1+2\alpha E(\boldsymbol{k})}\right]^{1/2} \qquad \text{and} \qquad c_{\boldsymbol{k}} = \left[\frac{\alpha E(\boldsymbol{k})}{1+2\alpha E(\boldsymbol{k})}\right]^{1/2}$$

where α is the same material dependant constant used in Equation (81).

More information alongside a more detailed derivation for the overlap integral can be found in References [61] and [62] for the remainder of this work; however, we assume that all the scattering mechanisms use parabolic bands and thus $G(\boldsymbol{k}, \boldsymbol{k'})$ is neglected.

4.4 Scattering Mechanisms

We will now briefly discuss the physical origins of several common scattering mechanisms that are important for simulations of electron transport in semiconductors. These are:

- phonon scattering
- interactions with ionised impurities
- alloy scattering
- surface roughness

All of these interactions can be classified by there initial and final energies as either Intervalley; whereby the initial and final energy states lie in the same conduction band valley, or Intravalley where the initial and final states are in different valleys.

Phonon Scattering When considering the effects of scattering on the electron transport through a solid perhaps the most important interaction is that of electrons with Phonons. A phonon is simply put a quasi-particle that is associated with vibration in the crystal lattice. In a perfect crystal, each atom is joined to its neighbours in 3 dimensions by bonds in a repeating pattern. This system can be modelled as masses joined together by tiny springs.

As one atom gains energy from outside the system (usually from heat or sound waves), it vibrates, and this vibration travels down the chain of particles as a mechanical wave. These waves which travel throughout the crystal have a definite momentum and energy and thus can be divided into small packets which are discrete units (quantum) of vibrational mechanical energy. Therefore, we can treat these wave packets quantum mechanically as

particles called phonons (these are analogous to photons being particles/wave-packets that act as the quantum for electromagnetic energy).

Phonons can form two distinct types of vibrational modes known as optical and acoustic modes. Acoustic modes form when all N atoms vibrate in phase (similar to sound waves travelling through air hence the name) with the number of possible modes, equal to the number of vibrational degrees of freedom (see figure 14). Optical modes (which are named because in many crystalline materials such modes can be induced using infra-red radiation) form when atoms vibrate out of phase, with the number of possible modes being given by $D(N-1)$ where N is the number of atoms in the unit cell and D is the number of vibrational degrees of freedom (again see Figure 14).

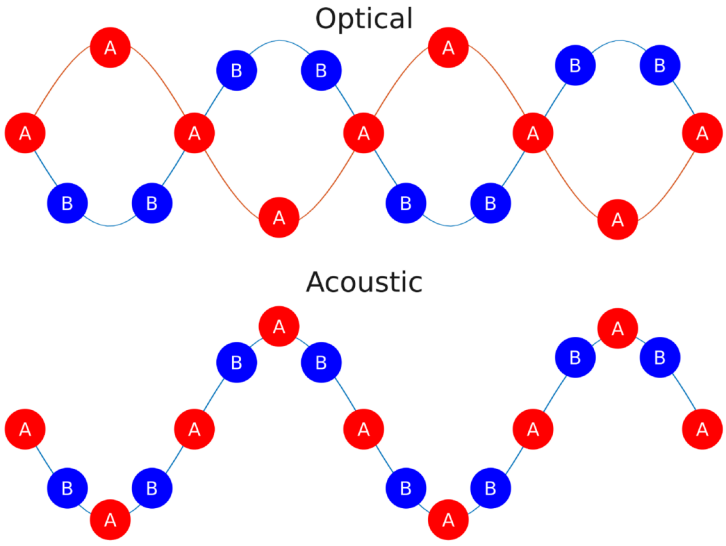

Figure 14: Diagram to show optical (top) and acoustic (bottom) phonon modes for a lattice consisting of two distinct atoms A and B.

We can describe these modes as collective oscillations of ions with the displacement U of an ion at a lattice site $\boldsymbol{R}$ being the superposition of these oscillations given by [62]:

$$U(R,t) = \sum_{\boldsymbol{q}} \left(\frac{\hbar}{2\rho\Omega\omega_q} \right)^{1/2} \hat{e_q}(a_q + a_{-q}^{+}) e^{i\boldsymbol{q}\cdot\boldsymbol{R}} \tag{99}$$

where: $\boldsymbol{q}$ is the phonon wave vector, ω_q is the angular frequency, ρ is the crystal density, Ω is the crystal volume and a_{-q}^{+} and a_q are the phonon creation and annihilation operators respectively. The unit vector $\hat{e_q}$ is used to define the polarisation direction of the phonon

whereby for an symmetric crystal we have for any given $\boldsymbol{q}$ one longitudinal mode ($\boldsymbol{q}$ is parallel to $\hat{e_q}$) and two transverse modes ($\boldsymbol{q}$ is perpendicular to $\hat{e_q}$).

If we now take a phonon moving through the crystal lattice, the small change in lattice constant will produce a small instantaneous change in the energy bands it is this change in energy that causes the electrons to scatter. The change in lattice spacing can be expressed by the induced strain in the lattice given by $\boldsymbol{\nabla} \cdot \boldsymbol{u}(\boldsymbol{r}, t)$ Thus we can write the interaction potential H' as:

$$H' = \Xi_d \boldsymbol{\nabla} \cdot \boldsymbol{u}(\boldsymbol{r}, t)$$

for acoustic phonons where Ξ_d is the acoustic deformation potential.

Since $\boldsymbol{\nabla} \cdot \boldsymbol{u}(\boldsymbol{r}, t)$ vanishes for transverse phonons we can substitute these into equation (99) to obtain:

$$H'_{acoustic} = \sum_{\boldsymbol{q}} i\Xi_d \boldsymbol{q} \left(\frac{\hbar}{2\rho\Omega\omega_q} \right)^{1/2} \hat{e_q}(a_q + a_{-q}^+) e^{i\boldsymbol{q}\cdot\boldsymbol{R}}. \tag{100}$$

The operators $a_q^+$and a_q satisfy the commutator relation $a_q a_q^+ - a_q^+ a_q = \delta_{qq}$. Therefore the Hamiltonian for the absorption or emission of a phonon can be expressed as [62]

$$H = \sum_{\boldsymbol{q}} \hbar\omega_q (a_q^+ a_q + \tfrac{1}{2})$$

and if we denote the eigenfunction of the initial state of the electron as $|c\rangle$ and the final state as $|c'\rangle$ we have $a_q^+ a_q |c\rangle = n_q |c\rangle$, where n_q is the number of phonons with mode q in state $|c\rangle$. which for a Bose-Einstein distribution at lattice temperature T_L is given by [62]

$$\langle n_q \rangle = \frac{1}{\exp(\hbar\omega_q / k_B T_L) - 1} \tag{101}$$

Thus we can obtain the energy eigenvalues as

$$\varepsilon_q = \hbar\omega_q (n_q + \tfrac{1}{2})$$

The matrix elements corresponding to the phonon emission and absorption processes are then given by:

$$\langle c' | a_q | c \rangle = \sqrt{n_q} \quad \text{- absorption} \tag{102}$$

$$\langle c' | a_q^+ | c \rangle = \sqrt{n_q + 1} \quad \text{- emission} \tag{103}$$

Therefore by using the golden rule given by Equation (95) we can obtain the probability per unit time of an electron transitioning from state $\boldsymbol{k}$ to $\boldsymbol{k'}$ due to interaction with a non-polar acoustic phonon as [62, 61]:

$$P_{acoustic}(\boldsymbol{k},\boldsymbol{k'}) = \frac{\pi\Xi_d^2 q^2}{\rho\omega_q\Omega}(n_q + \tfrac{1}{2} \pm \tfrac{1}{2})\delta(\boldsymbol{k'} - \boldsymbol{k} \pm \boldsymbol{q})\delta(E(\boldsymbol{k'}) - E(\boldsymbol{k}) \pm \hbar\omega_q) \tag{104}$$

The two delta functions in equation (104) ensure the conservation of both momentum and energy, since $E(\boldsymbol{k'}) = E(\boldsymbol{k}) \pm \hbar\omega_q$ and $\boldsymbol{k'} = \boldsymbol{k} + \boldsymbol{q}$.

If we now note that for a parabolic energy band the energy conservation can be expressed as $\frac{\hbar\boldsymbol{k'}^2}{2m^*} = \frac{\hbar\boldsymbol{k}^2}{2m^*} \pm \hbar\omega_q$ we can combine the two δ functions as follows

$$\delta(\boldsymbol{k'} - \boldsymbol{k} \pm \boldsymbol{q})\delta(E(\boldsymbol{k'}) - E(\boldsymbol{k}) \pm \hbar\omega_q) = \delta\left(\frac{\hbar\boldsymbol{q}^2}{2m^*} \pm \frac{\hbar\boldsymbol{k}\boldsymbol{q}\cos\theta'}{m^*} \pm \hbar\omega_q\right) \tag{105}$$

where θ' is the polar angle between $\boldsymbol{k}$ and $\boldsymbol{q}$ and

$$\cos\theta' = \frac{1}{2}\left(\pm\frac{\boldsymbol{q}}{\boldsymbol{k}} + \frac{\hbar\omega_q\boldsymbol{k}}{E(\boldsymbol{k})\boldsymbol{q}}\right) \tag{106}$$

We can further simplify this calculation by making the observation that at room temperature $\hbar\omega_q \ll k_BT$. Thus we can assume the phonon scattering to be elastic (i.e. $\hbar\omega_q = 0$) and we can approximate n_q from equation (101) as $n_q \approx \frac{k_BT_L}{\hbar\omega_q}$. Finally, we note that for long wavelength phonons $\omega_q/q = v_s$ where v_s is the velocity of sound in the semiconductor, thus we can rewrite equation (104) as

$$P_{acoustic}(\boldsymbol{k},\boldsymbol{k'}) = \frac{\pi\Xi_d^2 k_BT_L}{\hbar\rho v_s^2}\frac{\boldsymbol{k}}{E(\boldsymbol{k})\boldsymbol{q}}\delta\left(\frac{\boldsymbol{q}}{2\boldsymbol{k}} \pm \cos\theta'\right) \tag{107}$$

The scattering rate can then be evaluated by substituting equation (107) into 96 and integrating over $\boldsymbol{k'}$. However, it is much easier to integrate with respect to $\boldsymbol{q}$ in spherical polar coordinates thus we obtain

$$\begin{aligned}\Gamma(\boldsymbol{k})_{acoustic} &= \frac{\pi\Xi_d^2 k_BT_L}{8\pi^2\hbar\rho v_s^2}\frac{\boldsymbol{k}}{E(\boldsymbol{k})}\int\frac{1}{\boldsymbol{q}}\delta\left(\frac{\boldsymbol{q}}{2\boldsymbol{k}} \pm \cos\theta'\right)d\boldsymbol{q} \\ &= \frac{\pi\Xi_d^2 k_BT_L}{8\pi^2\hbar\rho v_s^2}\frac{\boldsymbol{k}}{E(\boldsymbol{k})}\int_{q_{min}}^{q_{max}}\int_{-1}^{1}\int_0^{2\pi}\delta\left(\frac{\boldsymbol{q}}{2\boldsymbol{k}} \pm \cos\theta'\right)d\phi d(\cos\theta')\boldsymbol{q}d\boldsymbol{q}\end{aligned} \tag{108}$$

integration over ϕ is straightforward as is that over $\cos\theta'$, due to the delta function. Thus all we need is the limits for the integration over $\boldsymbol{q}$ which are easily obtained since $\cos\theta'$ is limited to ±1 thus using equation (106) we can obtain

$$\boldsymbol{q}_{min} = 0$$
$$\boldsymbol{q}_{max} = 2\boldsymbol{k}$$

and thus we can finally obtain the scattering rate as

$$\Gamma(\boldsymbol{k})_{acoustic} = \frac{\pi \Xi_d^2 k_B T_L}{8\pi^2 \hbar \rho v_s^2} \frac{\boldsymbol{k}}{E(\boldsymbol{k})} 2\pi \int_{\boldsymbol{q}_{min}}^{\boldsymbol{q}_{max}} \boldsymbol{q} d\boldsymbol{q} = \frac{\pi \Xi_d^2 k_B T_L}{8\pi^2 \hbar \rho v_s^2} \frac{\boldsymbol{k}}{E(\boldsymbol{k})} 4\pi \boldsymbol{k}^2$$

and therefore

$$\Gamma(\boldsymbol{k})_{acoustic} = \frac{2\pi \Xi_d^2 k_B T_L}{\hbar \rho v_s^2} N(E(\boldsymbol{k})) \tag{109}$$

where $N(E(\boldsymbol{k}))$ is the electron density of states given by

$$N(E(\boldsymbol{k})) = \frac{(2m^*)^{3/2}\sqrt{E(\boldsymbol{k})}}{4\pi^2\hbar^3} \tag{110}$$

Optical Phonons For non-polar optical phonons an equation for $P_{optical}$ can be obtained in a similar manner to equation (104) with two notable differences:

1. The acoustic deformation potential Ξ_d is replaced with an optical deformation potential D_0.
2. The optical phonon energy is nearly constant as a function of $\boldsymbol{q}$ thus we can replace n_q and ω_q with constant values n_0 and ω_0 respectively.

Thus the probability per unit time for interaction with a non-polar optical phonon is given by:

$$P_{optical}(\boldsymbol{k}, \boldsymbol{k'}) = \frac{\pi D_0^2 q^2}{\rho \omega_0 \Omega} (n_0 + \tfrac{1}{2} \pm \tfrac{1}{2}) \delta(\boldsymbol{k'} - \boldsymbol{k} \pm \boldsymbol{q}) \delta(E(\boldsymbol{k'}) - E(\boldsymbol{k}) \pm \hbar\omega_0) \tag{111}$$

Like the acoustic case we can use equation (105) to once again combine the two δ functions. However we must note that unlike the acoustic phonons the phonon energy $\hbar\omega_0$ for the optical case is not less than $k_b T$ at room temperature thus optical phonons undergo inelastic scattering and the probability is given by

$$P_{optical}(\boldsymbol{k}, \boldsymbol{k'}) = \frac{\pi D_0^2 q^2}{\rho \omega_0 \Omega} (n_0 + \tfrac{1}{2} \pm \tfrac{1}{2}) \delta\left(\frac{\hbar \boldsymbol{q}^2}{2m^*} \pm \frac{\hbar \boldsymbol{k}\boldsymbol{q} \cos\theta'}{m^*} \pm \hbar\omega_q \right) \tag{112}$$

This can then be substituted into equation (96) and integrated with respect to $\boldsymbol{q}$ (similar to equation (107)) to obtain the scattering rate as

$$\begin{aligned}\Gamma(\boldsymbol{k})_{optical} &= \frac{D_0^2}{8\pi^2\rho\omega_0}(n_0+\tfrac{1}{2}\pm\tfrac{1}{2})\int\delta\left(\frac{\hbar\boldsymbol{q}^2}{2m^*}\pm\frac{\hbar\boldsymbol{k}\boldsymbol{q}\cos\theta'}{m^*}\pm\hbar\omega_q\right)d\boldsymbol{q}\\ &= \frac{D_0^2}{8\pi^2\rho\omega_0}(n_0+\tfrac{1}{2}\pm\tfrac{1}{2})\frac{\boldsymbol{k}}{E(\boldsymbol{k})}\int_{q_{min}}^{q_{max}}\int_{-1}^{1}\int_0^{2\pi}\tfrac{1}{\boldsymbol{q}}\delta\left(\tfrac{\boldsymbol{q}}{2\boldsymbol{k}}\pm\cos\theta'\pm\tfrac{\hbar\omega_0\boldsymbol{k}}{2\boldsymbol{q}E(\boldsymbol{k})}\right)d\phi d(\cos\theta')\boldsymbol{q}^2d\boldsymbol{q}\end{aligned} \tag{113}$$

the limits q_{min} and q_{max} can then be defined using the δ function as

$$\begin{aligned}q_{min} &= \boldsymbol{k}\left|1-\left(1\pm\tfrac{\hbar\omega_0}{E(\boldsymbol{k})}\right)^{1/2}\right|\\ q_{max} &= \boldsymbol{k}\left(1+\left(1\pm\tfrac{\hbar\omega_0}{E(\boldsymbol{k})}\right)^{1/2}\right)\end{aligned}$$

Thus we obtain

$$\Gamma(\boldsymbol{k})_{optical} = \tfrac{D_0^2}{8\pi^2\rho\omega_0}(n_0+\tfrac{1}{2}\pm\tfrac{1}{2})\tfrac{2\pi\boldsymbol{k}^3}{E(\boldsymbol{k})}\left(1\pm\tfrac{\hbar\omega_0}{E(\boldsymbol{k})}\right)^{1/2} = \tfrac{\pi D_0^2}{\rho\omega_0}(n_0+\tfrac{1}{2}\pm\tfrac{1}{2})N(E(\boldsymbol{k})\pm\hbar\omega_0) \tag{114}$$

where $N(E(\boldsymbol{k})\pm\hbar\omega_0)$ is once again the density of states given by equation (110).

Interactions with Polar Phonons When dealing with ionic semiconductors (e.g. GaAs, InP etc.) phonons can cause polarisation waves, which are created by the oscillating electric dipole as the vibrations move through the lattice. These types of phonons will strongly interact with electrons causing polar scattering and can either be acoustic or optical. Interactions with polarised acoustic phonons (often referred to as piezoelectric scattering) are important at low temperatures in very pure semiconductors. The interaction Hamiltonian H' can be written as

$$H' = \int\rho(r)\phi(r)dr \tag{115}$$

where ρ is the charge density, and ϕ is the electric potential associated with the polarisation of the crystal.

The electrostatic field produced by the plane wave is given by [63, 61]

$$E_i = \frac{-P_{ijk}e_{jk}}{\varepsilon} \tag{116}$$

where p_{ijk} is the appropriate component of the piezoelectric tensor, e_{jk} is the strain tensor and ε is the dielectric constant.

When this is used in the golden rule calculation (Equation (96)) the transition rate from state $\boldsymbol{k}$ to $\boldsymbol{k'}$ can be shown to be [61, 63]

$$P(\boldsymbol{k},\boldsymbol{k'}) = \frac{8\pi^2 e^2 p_0^2 K_B T}{\hbar V q^2 V_{so}^2 \varepsilon^2 \rho}\left(\frac{\boldsymbol{q}^2}{\boldsymbol{q}^2+\beta^2}\right)^2 z\delta[E(\boldsymbol{k'})-E(\boldsymbol{k})] \tag{117}$$

where V_{so} is the average sound velocity in the materiel, p_0 is an appropriate piezoelectric constant and β is the inverse screening length given by

$$\beta = \left(\frac{4\pi^2 e^2 n_e}{\varepsilon K_b T}\right)^{1/2}$$

where n_e is the free carrier concentration.

Equation 117 can then be integrated over all $\boldsymbol{k'}$ to give the scattering rate Γ_{piezo} as

$$\Gamma(\boldsymbol{k})_{piezo}(E\boldsymbol{k}) = \frac{\sqrt{m^*}e^2 p_0^2 K_b T}{\sqrt{8}\varepsilon^2\hbar^2\rho V_{so}^2} E(\boldsymbol{k})^{-1/2}\left(\log\left(1+\tfrac{8m^*E(\boldsymbol{k})}{\hbar^2\beta^2}\right) - \tfrac{1}{1+[\hbar^2\beta^2/8m^*E(\boldsymbol{k})]}\right) \tag{118}$$

For polar optical phonons the interaction with electrons is very strong and is dominant at room temperature in compound semiconductors [62]. The strength of the polar interaction is proportional to the dipole moment created by the displacement of positive and negative ions ($\boldsymbol{u}^+$ and $\boldsymbol{u}^-$ respectively). The relative displacement $\boldsymbol{u} = \boldsymbol{u}^+ - \boldsymbol{u}^-$ can be written as [62]

$$\boldsymbol{u}(\boldsymbol{r},t) = \sum_{\boldsymbol{q}}\left(\frac{\hbar}{2NM\omega_0}\right)^{1/2} e_{\boldsymbol{q}}(a_{\boldsymbol{q}} + a_{\boldsymbol{q}}^{\pm})e^{i\boldsymbol{q}\cdot r} \tag{119}$$

where N is the number of pair ions and M is the reduced mass of the positive and negative ions (with $1/M = 1/M_+ + 1/M_-$). The polarisation P due to the relative displacement is then given by:

$$\boldsymbol{P} = \frac{e^* N}{\Omega}\boldsymbol{u}$$

where e^* is the effective charge given by [63]

$$e^* = \left(\frac{\Omega M}{N}\right)^{1/2}\omega_0\epsilon_{opt}\left(\frac{1}{\epsilon_{opt}} - \frac{1}{\epsilon_s}\right)^{1/2}$$

with ϵ_{opt} being the optical frequency range and ϵ_s the dielectric constant of the semiconductor.

The polarisation due to the displacement combines with the polarisation due to the ions themselves $\boldsymbol{P}_{ion}$ to create a dielectric displacement $\boldsymbol{D}$ given by

$$\boldsymbol{D} = \epsilon_0\boldsymbol{F} + \boldsymbol{P}_{ion} + \frac{e^* N}{\Omega}\boldsymbol{u}$$

where ϵ_0 is the dielectric constant of a vacuum and $\boldsymbol{F}$ is the electric field.

since $\boldsymbol{P}_{ion}$ is related to ϵ_{opt} as $\epsilon_{opt}F = \epsilon_0 F + \boldsymbol{P}_{ion}$ thus we can re-write $\boldsymbol{D}$ as

$$\boldsymbol{D} = \epsilon_{opt}\boldsymbol{F} + \frac{e^* N}{\Omega}\boldsymbol{u} \tag{120}$$

However D is expected to vary as $\boldsymbol{D} = D\boldsymbol{e}_q e^{i\boldsymbol{q}\cdot\boldsymbol{r}}$ and since $\boldsymbol{\nabla}\cdot\boldsymbol{D} = 0$ for polarised charges

$$i\boldsymbol{q}\cdot\boldsymbol{D} = 0$$

which implies that $\boldsymbol{D} = 0$ for non-zero $\boldsymbol{q}$. Thus substituting $\boldsymbol{D} = 0$ into equation (120) we obtain an expression for the electric field

$$\boldsymbol{F} = -\frac{Ne^*\boldsymbol{U}}{\Omega\epsilon_{opt}} \tag{121}$$

from here it is straightforward to find the electrostatic potential $\boldsymbol{\phi}(r)$ as

$$\boldsymbol{\phi}(r) = -\int \boldsymbol{F}dr = -i\frac{N}{\Omega}\frac{e^*}{q\epsilon_{opt}}\boldsymbol{u}(r)$$

and thus finally the perturbation Hamiltonian H' as

$$H' = -e\boldsymbol{\phi}(r) = \sum_{\boldsymbol{q}} i\frac{e}{q}\left(\frac{\hbar\omega_0}{2\epsilon_p\Omega}\right)^{1/2}(a_{\boldsymbol{q}} + a^{\pm}_{\boldsymbol{q}})e^{i\boldsymbol{q}\cdot r} \tag{122}$$

where $1/\epsilon_p = 1/\epsilon_{opt} - 1/\epsilon_s$.

This then allows us to calculate the scattering probability per unit time using equation (96) as [62, 61]

$$P(\boldsymbol{k},\boldsymbol{k'}) = \frac{\pi e^2\omega_0}{\epsilon_p\Omega}\frac{1}{q^2}[n(\omega_0) + 1/2 \mp 1/2]\delta(\boldsymbol{k'} - \boldsymbol{k} \mp \boldsymbol{q})\delta(E(\boldsymbol{k}) - E(\boldsymbol{k'}) \mp \hbar\omega_0) \tag{123}$$

and the scattering rate Γ_{popt} as[62]

$$\Gamma(\boldsymbol{k})_{popt} = \frac{e^2\omega_0}{8\pi\epsilon_p}\frac{\boldsymbol{k}}{E(\boldsymbol{k})}[n(\omega_0) + \tfrac{1}{2} \mp \tfrac{1}{2}]\ln\left(\frac{q_{min}}{q_{max}}\right) \tag{124}$$

where q_{min} and q_{max} are given by

$$q_{min} = \boldsymbol{k}\left|1 - \left(1 \pm \tfrac{\hbar\omega_0}{E(\boldsymbol{k})}\right)^{1/2}\right|$$
$$q_{max} = \boldsymbol{k}\left(1 + \left(1 \pm \tfrac{\hbar\omega_0}{E(\boldsymbol{k})}\right)^{1/2}\right)$$

Ionised Impurity Scattering electron scattering due to shallow donor impurities is often considered an elastic process since the mass of the impurity atom is much larger than that of the electron thus any change in energy that would occur during such an interaction is considered negligible. In order to derive the perturbation Hamiltonian H' (and ultimately the scattering probability $P(\boldsymbol{k}, \boldsymbol{k'})$ we will first consider the case of an electron that is scattered by a positively charged donor impurity in an n-type semiconductor. If the impurity has a net positive charge of Ze then the potential can be approximated as the bare coulomb potential given by:

$$V(r) = \frac{Ze}{4\pi\epsilon_0\epsilon_s r}$$

This however does not account for the effect of screening due to the presence of other electrons surrounding the donor. This was employed in the method developed by Brooks (and independently by Herring)[61, 62] in which he showed the screened potential $V'(r)$ can be expressed by

$$V'(r) = \frac{Ze}{4\pi\epsilon_0\epsilon_s r} e^{-r/\lambda_D} \tag{125}$$

where λ_D is known as the Debye length and is given by

$$\lambda_D = \sqrt{\frac{\epsilon_0\epsilon_s K_B T}{e^2 n_0}}$$

The perturbation Hamiltonian can then be written as

$$H' = eV'(r) = \frac{Ze^2}{4\pi\epsilon_0\epsilon_s r} e^{-r/\lambda_D} \tag{126}$$

and thus the matrix element can be obtained by

$$\begin{aligned}
\langle \boldsymbol{k'}|H'|\boldsymbol{k}\rangle &= \frac{1}{\Omega}\frac{Ze^2}{4\pi\epsilon_0\epsilon_s r}\int_\Omega e^{-i\boldsymbol{k'}\cdot\boldsymbol{r}}\frac{e^{-r/\lambda_D}}{r}e^{-i\boldsymbol{k}\cdot\boldsymbol{r}}d^3r \\
&= \int_0^\pi\int_0^\infty e^{-i\boldsymbol{k}\cdot\boldsymbol{r}}\left(\frac{e^{-r/\lambda_D}}{r}\right)r^2\sin(\theta_r)d\theta_r dr \\
&= \frac{e^2\lambda_D^2}{\Omega\epsilon_0\epsilon_s(1+\boldsymbol{K}^2\lambda_D^2)}
\end{aligned} \tag{127}$$

where $d^3r = 2\pi r^2\sin(\theta_r)d\theta_r dr$ and $\boldsymbol{K} = \boldsymbol{k'} - \boldsymbol{k}$ Thus using equation (96) the transition probability due to a single ionised impurity can be found as

$$P(\boldsymbol{k'}, \boldsymbol{k}) = \frac{2\pi}{\hbar}\left(\frac{Ze^2}{\Omega\epsilon_0\epsilon_s}\right)^2\frac{\delta(E_{k'} - E_k)\lambda_D^4}{(1+\boldsymbol{K}^2\lambda_D^2)^2} \tag{128}$$

Finally this can then be multiplied by the number of impurities $N_i\Omega$ in the crystal volume thus we have

$$P(\boldsymbol{k'}, \boldsymbol{k}) = \frac{2\pi}{\hbar}\frac{N_i Z^2 e^4}{\Omega\epsilon_0^2\epsilon_s^2}\frac{\delta(E_{k'} - E_k)\lambda_D^4}{(1+\boldsymbol{K}^2\lambda_D^2)^2} \tag{129}$$

The scattering rate $\Gamma_{ionised}$ can then be found by once again by integration over all $\boldsymbol{k'}$ to give

$$\Gamma(\boldsymbol{k})_{ionised} = \frac{2\pi N_i Z^2 e^4 N(E(\boldsymbol{k}))}{\hbar \epsilon_0^2 \lambda_D^2 (4\boldsymbol{k}^2 + \lambda_D^2)} \tag{130}$$

where $N(E(\boldsymbol{k}))$ is once again the density of states gievn by equation (110).

Alloy Scattering In alloys (GaAs, InP etc.) due to the random distribution of component atoms among the available lattice sites a new mechanism for carrier scattering is introduced. This alloy scattering occurs due to the change in potential as the carriers randomly encounter different atomic cores as they move across the lattice. The amount of scattering, therefore, depends on three factors. The alloy concentration x, the difference in potential between the two alloyed atoms D_{Alloy} (this potential can be fitted to experimental data, taken as a difference in electron affinities or as an electronegative difference) and the amount of disorder in the lattice (this is usually achieved with a constant d for which $d = 0$ is perfectly ordered and $d = 1$ is considered random). All of this was taken into account in a model developed by Harrison and Hauser [64, 65] in which they showed that the alloy scattering rate Γ_{Alloy} can be expressed as

$$\Gamma_{Alloy} = \frac{3\pi}{8\sqrt{2}} \frac{(m^*)^{3/2}}{\hbar^4} \Omega d D_{Alloy}^2 x(1-x)\sqrt{E} \tag{131}$$

where: Ω is the crystal unit cell, and g_{3D} is the $3D$ density of states.

Surface Roughness Scattering Surface roughness scattering (sometimes referred to as interface roughness scattering) is an elastic scattering process where electrons move in the vicinity of the surface of a material (or an imperfect interface between two different materials). Scattering occurs due to small local variations in the potential due to imperfections in the surface (or interface). This type of scattering often considered for 2-dimensional electron gasses where it can be induced due to the proximity of the heterostructure that creates the quantum well. It is also considered at low temperatures where its effects are comparatively stronger due to the reduced influence of phonons.

For a z-confined 2D heterostructure the "local" potential will fluctuate based on position in th $x - y$ plane. The commonly used expression for the resulting scattering rate [66, 67] assumes that the roughness has a Gaussian Fourier transform $\Delta_z(r)$ with height Δ and correlation length Λ and is isotropic across the x-y plane such that such that

$$\langle \Delta_z(r)\Delta_z(r')\rangle = \Delta^2 \exp\left(\frac{|r-r'|^2}{\Lambda^2}\right)$$

The perturbation H' due to a position shift Δ_z can then be expressed as

$$H' = V[z - \Delta_z(r)] - V(z) \approx -\Delta_z(r)\frac{\mathrm{d}V(z)}{\mathrm{d}z}$$

The 2D scattering matrix element F_{sr} can then be expressed as

$$F_{sr} = \langle k'|H'|k\rangle$$

This then leads to the scattering rate Γ_{SR} from equation (96) as

$$\Gamma_{SR} = \frac{m * \Delta^2\Lambda^2|F_{sr}|^2}{\hbar^3}\int_0^\pi d\theta e^{-(k'-k)\Lambda^2/4} \tag{132}$$

4.5 Device Simulations

Now that we have covered the basic method for bulk semiconductors we must turn our attention to how to adapt the Monte Carlo method for use with device simulations. In order to achieve this four additional factors must be taken into account.

1. The motion of carriers is spatially restricted to a device region, unlike the bulk case where the motion spreads in a vast region.
2. The carriers must be allowed to both enter and exit the simulation area through the device terminals.
3. The potential calculation must be done self-consistently through the solution of the Poisson equation with appropriate boundary conditions.
4. The boundary conditions applied to the carrier motion must also be consistent with the boundary condition applied to the Poisson equation.

To address point 1, we can use a surface boundary condition, whereby a boundary is set to be the edge of the simulation area such that when the particles are about to cross they are instead reflected into the device region. Point 2 can be addressed by not simulating the motion of all the particles but instead holding some particles outside the simulation using a reservoir. The surface boundaries can then be adapted in the region of the contacts to either allow carriers in the reservoir into the simulation area or allow carriers in the simulation area to exit back into the reservoir (see figure 15a). Finally to address points 3 and 4 we can use a finite element approach to solve the Poisson equation (the various detailed methods for which can be found in any good computational physics textbook see for example references

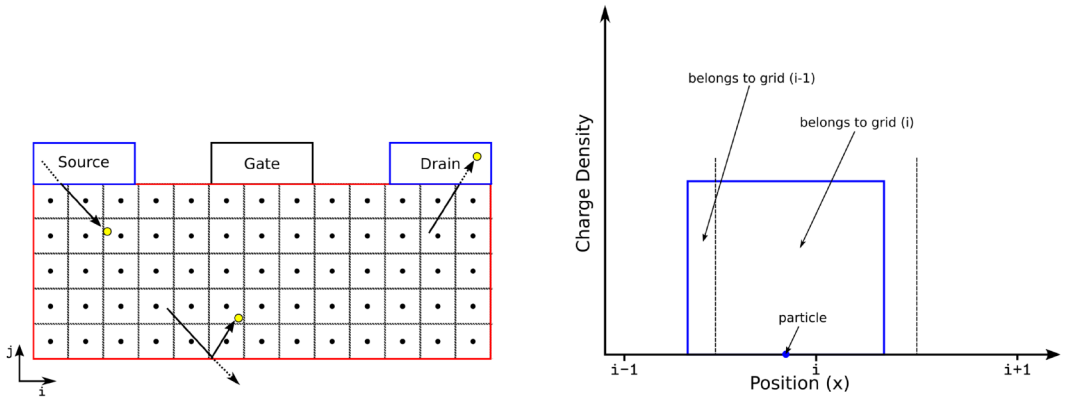

(a) (b)

Figure 15: (a) Diagram of an example grid for a basic transistor. Black dots indicate the 2D grid points (i, j) while the black dotted lines denote the cells surrounding each point which are used to approximate the charge density. The red lines indicate the position of the reflective boundaries while the blue lines represent the reservoirs for the source and drain terminals. (b) Diagram of the step function used to ascertain the charge density at each grid point for use in the Poisson solver. If the charge density associated with the superparticle spreads over a cell boundary, then it is counted as being at both grid points on the mesh.

[68, 61, 62]). To achieve this we need to define a grid of mesh points across the device each surrounded by a cell (see figure 15a) we can then obtain the charge density at each grid point by regarding each particle as a "super" particle.

In reality, the carrier density of a semiconductor is on the order of 10^6, but in practice, we are computationally limited to at most a few hundred thousand particles. Thus to approximate the charge density at each grid point, we must treat each particle as a cloud of charge that that is spread spatially such that the charge density is a step function of position (see figure 15b). By counting the number of particles inside each cell, we can then obtain the carrier density as:

$$n(i,j) = N(i,j)\frac{N_{pp}}{\Delta_x \Delta_y} \tag{133}$$

where $N(i,j)$ is the number of particles in the cell, around grid points i and j and N_{pp} is the number of particles that each "super" particle represents.

Therfore, we can now solve the Poisson equation for the potential ϕ at each grid point as:

$$\boldsymbol{\nabla}^2\phi(i,j) = -\frac{n(i,j)}{\varepsilon_s} \tag{134}$$

using dirichlet boundary conditions for the source-drain and gate contacts.

Thus we now have all the information we need to create a Monte Carlo method for electron transport in a semiconductor device. Fist we must define our device including: device geometry, doping profile, position of the terminals and structure of the semiconductor layers (if simulating a heterostructure). We then need to initialise or particles by calculating the initial particle distributions in real and $\boldsymbol{k}$-space and specifying the initial potential profile used fro the device. For the initial spacial distributions it is common to use a density profile based on the drift diffusion model that is computed in advance to save time.[62] The initial energy and $\boldsymbol{k}$-space distributions are usually then handled using either a Fermi-Dirac or Boltzmann distribution (depending on the Lattice temperature) and the magnitude of the $\boldsymbol{k}$-vector can then be found by re-arranging Equations (78) or (81). The direction of the $\boldsymbol{k}$-vector can then be determined randomly using spherical polar coordinates given by:

$$\begin{aligned} k_x &= |\boldsymbol{k}|\sin(\theta)\cos(\phi) \\ k_y &= |\boldsymbol{k}|\sin(\theta)\sin(\phi) \\ k_z &= |\boldsymbol{k}|\cos(\theta) \end{aligned}$$

with

$$\phi = 2\pi r_1$$
$$\cos(\theta) = 1 - 2r_2$$
$$\sin(\theta) = \sqrt{1 - \cos^2(\theta)}$$

where r_1 and r_2 are random numbers between 0 and 1.

The next step initially follows the ensemble Monte Carlo method whereby for each particle we perform successive cycles of free flight and scattering. The main difference, however, is that now after each free-flight we check to see if the particle has crossed a boundary and if so then either reflect the particle into the simulation area or remove the particle into the reservoir. After all the particles have moved to there new positions we then need to add a new routine to handle particles in the region surrounding the source and drain. This routine is essential for two reasons. The first reason is that if the particles can only leave the simulation and are not replaced, we will eventually run out of particles in the simulation area.

The second reason, however, is less apparent and stems from the fact that we are assuming the source and drain contacts to be ohmic. Ohmic contacts are usually modelled as charge-neutral areas that are always in thermal equilibrium even when current is flowing. Thus need to maintain charge neutrality in the vicinity of the source and drain, since the voltage drop in this area will be negligible, and hence no power is dissipated in this area. To achieve this, we need a routine that will keep the number of particles constant in the cells that correspond to the source and drain contacts.

Thus once all the particles have finished moving the number of particles in the contact regions needs updating by either removing or replacing particles (using a similar procedure to the initialisation) depending on the initial doping density in that region (that we defined in the initial set-up). The final step is then to calculate the charge density and solve the Poisson equation for the potential at each grid point. We then repeat the whole process starting at the free-flight and scattering until we reach the desired end time $t = t_{max}$ (see figure 16).

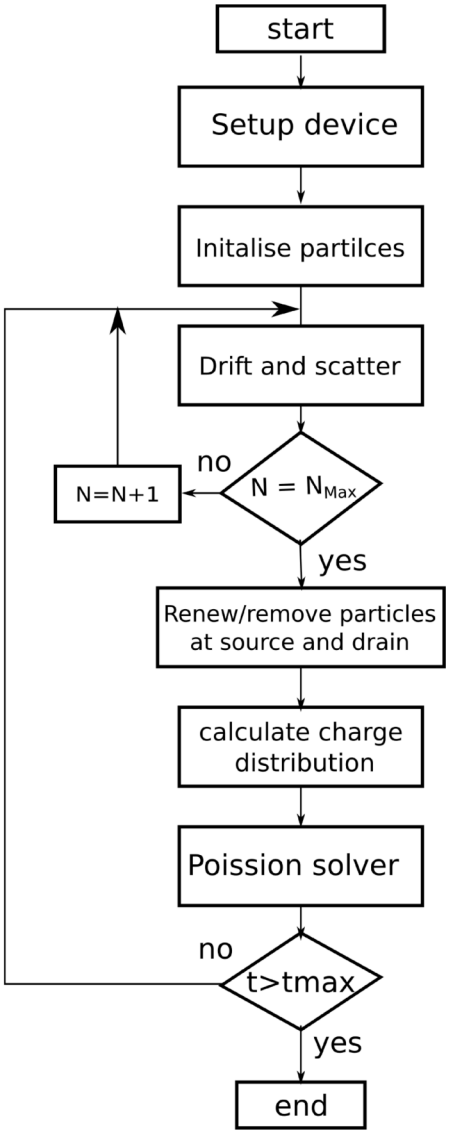

Figure 16: Flow chart to show the procedure for the device Monte Carlo simulation method.

4.6 Overview

In this chapter we have presented the fundamentals of the Monte Carlo method and the scattering processes that are important for the realistic semiconductor transport. The final few chapters we will now cover our application of all the techniques discussed thus far to the simulation of an InGaAs spin-FET.

5 Electron Spin in III-V Monte Carlo

5.1 Why III-V?

The use of III-V compound semiconductors for spintronic applications goes back to the earliest days of the field. Not only was the original Datta-Das Transistor based on a GaAs quantum well (see section 1.2) but also much of the early theoretical work on both spin transport and relaxation is based on these materials and the physics is by now well understood. The main reason for the this is that unlike more common Si, III-V materials (such as GaAs) have a direct band gap. This property makes them optically active and thus allows for highly efficient optical spin injection and detection through the use of circularly polarised light, as opposed to more problematic and inefficient electrical methods. This along with the observations of very long spin coherence times in bulk GaAs (on the order of 10's of ns [69]) has made GaAs based devices a top contender for use in spintronics (although Si has gained more ground in recent years due to advances in spin injection and lower device fabrication costs).

5.2 Simulation Method

The main method used in this work for studying the spin transport in InGasAs is an adaptation of the method laid out in [16]. This involved augmenting an existing ensemble III-V Monte Carlo simulation of a InGaAs MOSFET by including the electron spin as an additional degree of freedom. The simulator is an advanced 2D finite element III-V heterostructure Monte Carlo simulation tool, which was developed in-house and is self-consistently coupled with solutions to the Poisson equation that accounts for both long-range electron-electron interactions and quantum corrections using the effective quantum potential [7, 70].

The simulator uses an analytical band-structure with non-parabolic energy dispersion that accounts for the Γ, L and X conduction band valleys [71]. Furthermore, electron scattering was considered for: polar optical phonons, inter-valley and intra-valley optical phonons, non-polar optical phonons, acoustic phonons, interface roughness, interface phonons at the dielectric/semiconductor interface, and ionised impurity scattering using a static screening model. Finally, the alloy scattering, as well as strain effects on bandgap, electron effective mass, optical phonon deformation potential and energy were included in the device channel [70].

This device simulation tool was verified with experimental data for various devices, including measured I-V characteristics of a 120 nm gate length $In_{0.2}Ga_{0.8}As$ pseudomorphic [71], lattice matched metamorphic HEMT [72], and a 50 nm gate length $In_{0.7}Ga_{0.3}As$/InP HEMT [73].

The electron spin was accounted for using a spin density matrix $\rho(t)$ in addition to the $3D$ $\boldsymbol{k}$-space and $2D$ real space freedoms already present in the simulator. Since electrons are spin $\frac{1}{2}$ particles the density matrix is given by

$$\rho(t) = \begin{pmatrix} \rho_{\uparrow\uparrow}(t) & \rho_{\uparrow\downarrow}(t) \\ \rho_{\downarrow\uparrow}(t) & \rho_{\downarrow\downarrow}(t) \end{pmatrix} \tag{135}$$

where $\rho_{\uparrow\uparrow}$ $\rho_{\downarrow\downarrow}$ represent the probability finding an electron in the spin up or spin down state and $\rho_{\uparrow\downarrow}$ $\rho_{\downarrow\uparrow}$ represent the coherence. With $\rho_{\downarrow\uparrow}(t) = \rho_{\uparrow\downarrow}(t)^*$ and $\rho_{\uparrow\uparrow}(t) + \rho_{\downarrow\downarrow}(t) = 1$. The time evolution of a density matrix has already been discussed in section 2.2.2 and is governed by the Von Neumann equation $\frac{\mathrm{d}\rho(t)}{\mathrm{d}t} = -\frac{i}{\hbar}[H, \rho(t)]$ where H is the system Hamiltonian. Since the D'yakov-perrel mechanism is the main cause of spin relaxation in an InGaAs quantum well[17, 19, 16] the Hamiltonian contains two terms relating to the spin-orbit interaction.

1. The simplified Dresselhaus Hamiltonian $H_D = \gamma\langle k_y^2\rangle(k_z\sigma_z - k_x\sigma_x)$ which accounts for spin-orbit coupling as a result of bulk inversion asymmetry of the crystal in the limit $k_x^2, k_z^2 << \langle k_y^2\rangle$.
2. The Rashba Hamiltonian $H_R = \alpha_{br}(k_z\sigma_x - k_x\sigma_z)$ which accounts for spin-orbit coupling due to structural inversion asymmetry of the quantum well.

where x is taken to be the transport direction along the device channel, y is the growth direction of the quantum well, and the material dependent parameters α_{br} and γ are the so-called Rashba and Dresselhaus parameters respectfully.

The value of these parameters was estimated using $\boldsymbol{k}\cdot\boldsymbol{p}$ bandstructure calculations, details of which can be found in section 3. Using Kane parameters for GaAs and InAs obtained from a 40 band tight binding model by Jancu et al. [9] (which are in good agreement with reported experimental values, see for example [58]) we then estimated the Rashba and Dresselhaus parameters for $In_{0.3}Ga_{0.7}As$ using linear interpolation and equations (72) and (73) from section 3 the values for which are given in table 2. We must note at this stage, however, that α_{br} is dependant on the strength of the electric field in the y-direction F_y thus we have used the $\boldsymbol{k}\cdot\boldsymbol{p}$ calculations to obtain the field independent part of α_{br}, α_0 such that $\alpha_{br} = \alpha_0 F_y(\boldsymbol{r})$ where $\boldsymbol{r}$ is the position of the electron in the device.

parameter	InAs	GaAs	$In_{0.3}Ga_{0.7}As$
E_0 (ev)	0.418	1.519	1.107
E_1 (ev)	4.480	4.540	4.522
Δ_0 (ev)	0.380	0.341	0.353
Δ_1 (ev)	0.310	0.200	0.233
Δ^- (ev)	-0.050	-0.170	-0.134
P (evÅ)	9.010	9.880	9.619
P_1 (evÅ)	0.660	0.410	0.485
Q (evÅ)	7.720	8.680	8.392
α_0 ($\mathring{A}^2$)	122.525	4.819	7.600
γ (ev$\mathring{A}^3$)	48.578	24.368	22.959

Table 2: Band energies and Kane parameters obtained from reference [9] used in the calculation of α_0 and γ. Note: α_0 is the field independent part of α_{br} given by $\alpha_{br} = \alpha_0 F_y(\boldsymbol{r})$ where F_y is the electric field in the growth direction of the well (in our case along the y axis).

According to [16] during each Monte Carlo "free flight" τ the spin density matrix evolves as

$$\rho(t+\tau) = e^{-i(H_r+H_D)\frac{\tau}{\hbar}}\rho(t)e^{i(H_r+H_D)\frac{\tau}{\hbar}} \tag{136}$$

and using basic matrix algebra it can be shown that

$$e^{-i(H_r+H_D)\frac{\tau}{\hbar}} = \begin{pmatrix} \cos(|\alpha|\tau) & i\frac{\alpha}{|\alpha|}\sin(|\alpha|\tau) \\ i\frac{\alpha^*}{|\alpha|}\sin(|\alpha|\tau) & \cos(|\alpha|\tau) \end{pmatrix} \tag{137}$$

and the hermitian conjugate for the operator $e^{i(H_r+H_D)\frac{\tau}{\hbar}}$. Where

$$\alpha = \hbar^{-1}[(\alpha_{br}k_z - \gamma\langle k_y^2\rangle k_x) + i(\alpha_{br}k_x - \gamma\langle k_y^2\rangle k_z)]$$

As seen in section 2.1 the density matrix can be parametrised as a spin-polarisation (Bloch) vector $\boldsymbol{S} = (s_x, s_y, s_z)^T$ where $S_j = \mathrm{Tr}(\sigma_j\rho(t))$, $j = x, y, z$ and σ_j are the Pauli matrices. Thus using equation 137, we can show that the time evolution of the density matrix during each "free flight" causes a rotation of the spin Bloch vector, the angle and direction of which depend on the k-vector, i.e. momentum, of the electron.

For our simulations, we began with a 25 nm gate length $In_{0.3}Ga_{0.7}As$ MOSFET with a

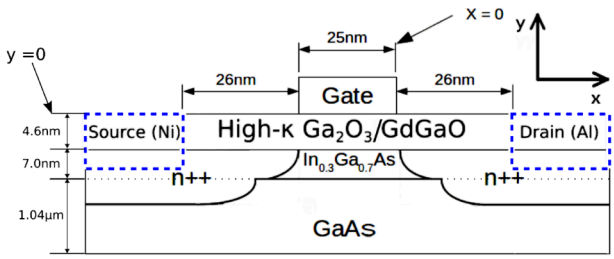

Figure 17: Cross section of the 25 nm gate length, n-channel $In_{0.3}Ga_{0.7}As$ MOSFET. The dielectric layer between the channel and the gate contact is grown on top of a Gallium Oxide/Gadolinium Gallium Oxide stack (Ga_2O_3/GdGaO) which is used to form a high-κ dielectric designed to reduce the leakage current [7]. The blue boxes indicate the position of the source and drain reservoirs used in the simulation.

spacer of 26 nm at room temperature (T = 300 K), a schematic diagram of which is shown in Figure 17.

The device consisted of a 7 nm thick $In_{0.3}Ga_{0.7}As$ channel grown on a 1.04 µm GaAs substrate with a thin 4.6 nm layer of Gallium Oxide/Gadolinium Gallium Oxide grown on top to act as a high-κ dielectric to separate the channel from the a gate contact (this is a common design used to reduce the leakage current in devices with short channels/gates and thus high electric fields in the region of the gate [7]). The structure has a background p-type doping of $1 \times 10^{18}\,\mathrm{cm}^{-3}$ and n-type doping in the source and drain (see regions marked n^{++} in Figure 17) which were Gaussian-like with a maximum of doping $2 \times 10^{19}\,\mathrm{cm}^{-3}$. Initially the spin states for all electrons in the device were chosen using two pseudo random numbers (R_1 and R_2) between 0 and 1. These were used to generate polar angles θ and ϕ with: $\theta = \pi R_1$ and $\phi = 2\pi R_2$, which in turn were used to calculate the Cartesian components for the magnetisation vector for each electron as:

$$S_x = \sin(\theta)\cos(\phi) \qquad S_y = \sin(\theta)\sin(\phi) \qquad S_z = \cos(\theta)$$

This ensured that each vector had a length of one and the states were spread evenly across the Bloch sphere such that there was no net magnetisation across the device. The spin injection was then handled by assuming the source was ferromagnetic such that all of the electrons that were injected into the channel had spin states aligned to either the x, y or z axis, depending upon the injection state being studied (i.e. The spin injection was assumed to be 100% efficient).

A simulated $I_D - V_D$ characteristic is given in Figure 18a this shows typical MOSFET

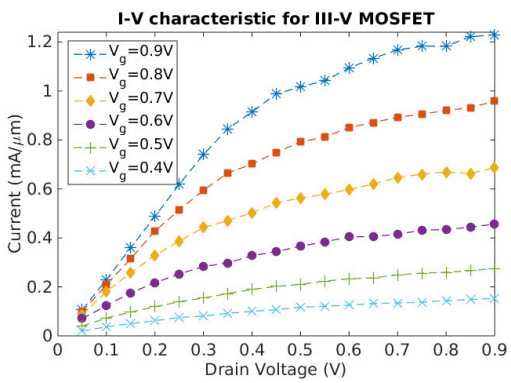

(a) I_D-V_D characteristic.

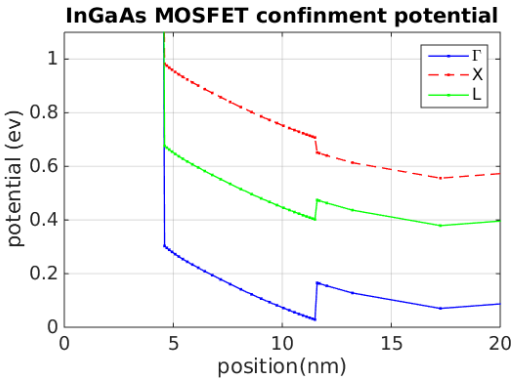

(b) Confinement potential showing the quantum well at the InGaAs/GaAs interface

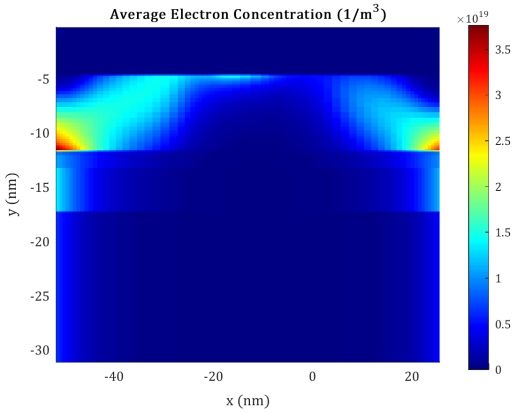

(c) Electron density across the device

Figure 18: Initial results for 25 nm gate length $In_{0.3}Ga_{0.7}As$ MOSFET.

behaviour whereby as the source-drain voltage increases we initially see a linear increase in current flow which eventually reaches saturation at which point further increasing V_D has no effect on the current flow through the channel. Figure 18b shows the confinement potential created by the GaAs/InGaAs heterostructure this forms a quantum well in the Γ conduction band which in turn leads to the formation of a 2-dimensional electron gas (2DEG) near the interface. This can also be seen in Figure 18c which contains a plot of the average electron density. As predicted the electrons are concentrated in a thin slice of the structure corresponding to the position of the quantum well between $y = -5$ and -12 nm (see Figure 18b) with the majority of the electrons being located at the bottom of the well at $y = -11.5$ nm.

A surface plot of the electric field across the device is shown in Figure 19a. The electric

field was calculated using a 2D a Poisson solver, approximating the charge density at each grid point using the "super-particle" method outlined in section 4.5. The plot shows that the field is highly non-linear and as expected is exceptionally high in the region of the source, drain and gate contacts, with fringe fields at the edges of the contacts on the order of $10^9\,\mathrm{V\,m^{-1}}$.

However, the vast majority of the electrons are found in the 2D channel at the bottom of the quantum well formed by the $In_{0.7}Ga_{0.3}/GaAs$ interface (located at $y = -11.5\,\mathrm{nm}$). Because the fringe fields are an order of magnitude higher than that in the channel ($\approx 10^7\,\mathrm{V\,m^{-1}}$) to view the electric field in the channel better, we have taken a thin slice across the device in the x-direction corresponding the centre the channel.

The electric field plotted against the position (x) in the slice is shown in Figure 19b. As expected much like the full surface plot the electric field rises and falls with the x-position of the contacts. From this, we can see that the field at the right-hand side of the source contact ($x = -52\,\mathrm{nm}$) initially slightly decreases but then begins to rise linearly as we move across the channel towards the left-hand side of the gate at $-26\,\mathrm{nm}$. As we move underneath the gate, the field fluctuates around $4.5 \times 10^7\,\mathrm{V\,m^{-1}}$ and before rising to a maximum value of $4.92 \times 10^7\,\mathrm{V\,m^{-1}}$ at the right-hand side of the gate. The field then rapidly decreases as we move past the gate contact to a minimum of $6.13 \times 10^6\,\mathrm{V\,m^{-1}}$ before finally rising to a final value of $3.40 \times 10^7\,\mathrm{V\,m^{-1}}$ as we approach the left-hand side of the drain at 26 nm.

Finally, Figure 19d shows the average velocity of the electrons in the x-direction (i.e. the direction of transport) with the position in the channel. As we move across the channel, the electrons begin to accelerate as they move from the source and pass underneath the gate. With the two main regions of acceleration corresponding to the two peaks in the x-component of the electric field (see Figure 19c). They reach maximum velocity at the right-hand side of the gate after which they sharply decelerate as they enter the right-hand side of the channel and head towards the drain.

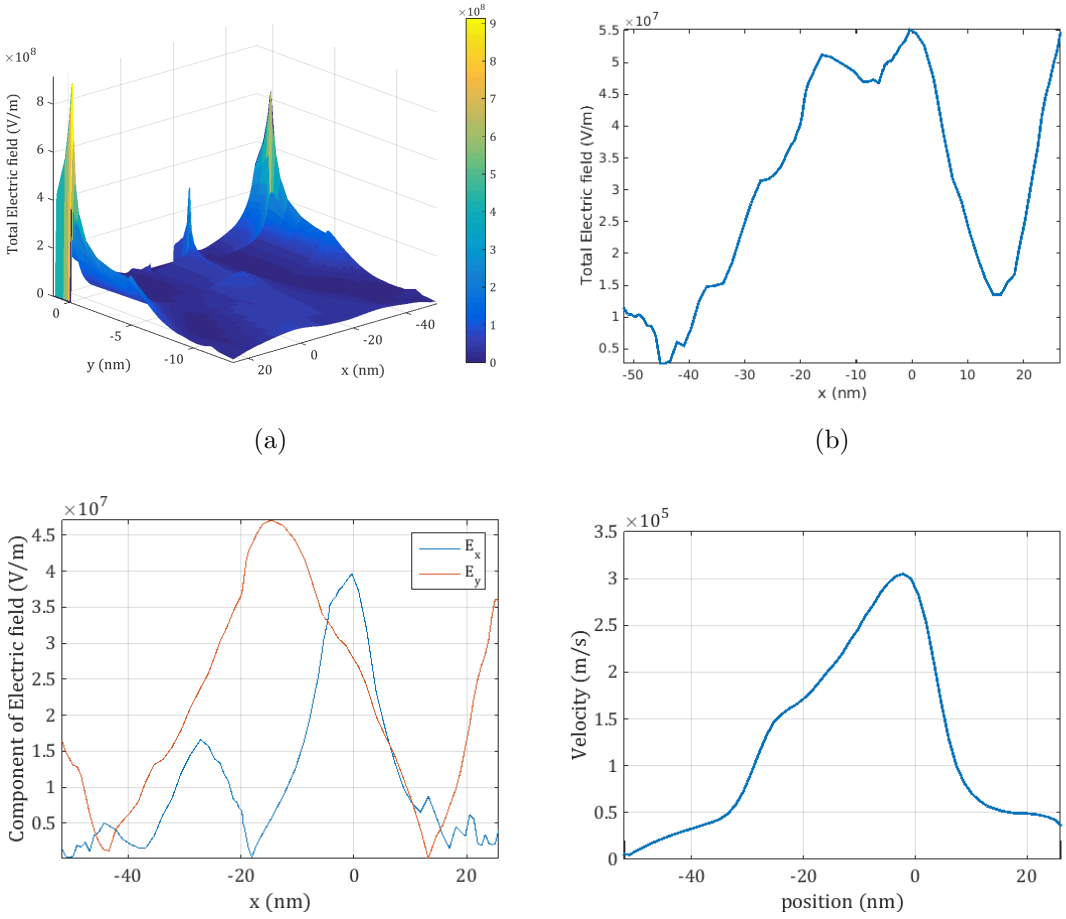

Figure 19: (a) Surface plot of the total electric field across the device structure. (b) Total electric field against position in the the centre of the device channel at $y = -11.5\,\text{nm}$. (c) x and y components of the electric field across the device channel. (d) average velocity in the x-direction of the electrons with the position in the channel.

5.3 Results

For our initial investigation we fixed the gate voltage (V_G) at 0.7 V and the drain voltage (V_D) at 0.5 V and ran the spin-transport simulator with 100 000 super-particles, for a total time of 10 ps in time steps of 1 fs. The electron spins in the device were initially randomly polarised such that there was no net magnetisation. For each time step, the average Bloch vector was calculated for the electrons contained in 100 evenly spaced slices across the channel. This entire process was then repeated for three different injected polarisations parallel to the x, y

and z axes.

Figure 20 show surface plots of the x, y and z components of the magnetization (S_x, S_y and S_z) for S_x injection in both position and time. From these we can see that the magnetization vector quickly reaches a steady state in around 2000 fs. Time slices taken at t =8 ps for each of the injection polarizations are given in Figure 21. For S_x injection as expected we see a high S_x polarization at the source (x =−52 nm) which decreases non-uniformly as we move across the channel towards the drain. The amount of decay fluctuates as we cross the gate (x =−26 nm to 0 nm) and then recovers slightly as we reach the drain (x =26 nm) leading to a net magnetization of $S = (0.43, 0.12, 0.01)$.

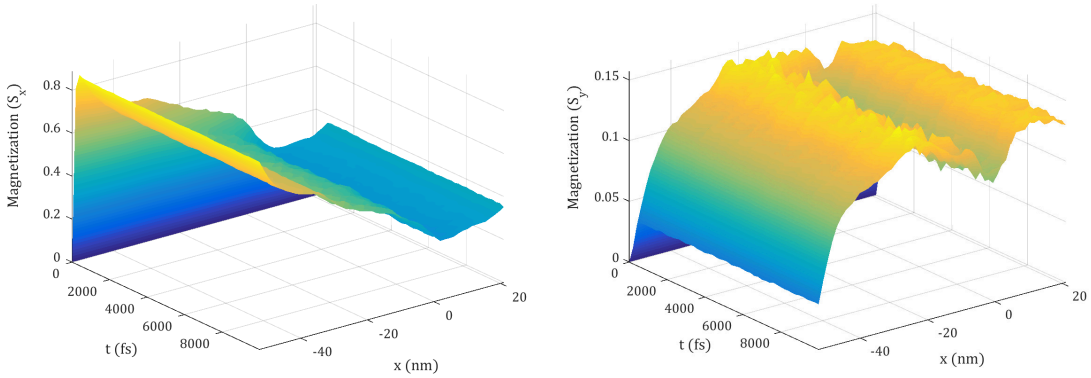

(a) x component

(b) y component

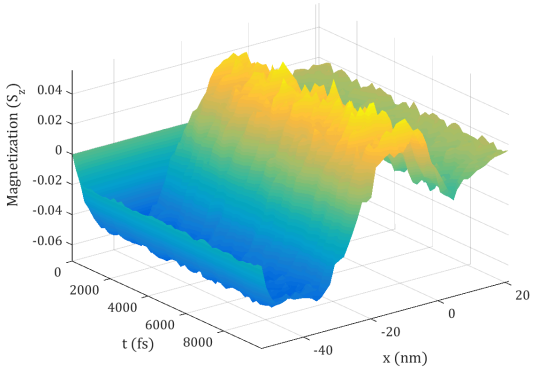

(c) z component

Figure 20: Surface plots in position and time of the x, y and z components of the magnetization for S_x injection.

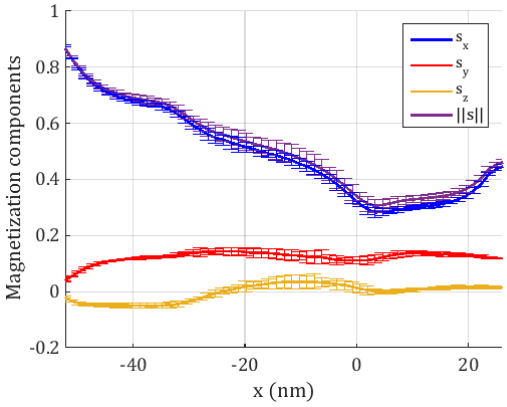

(a) S_x Injection

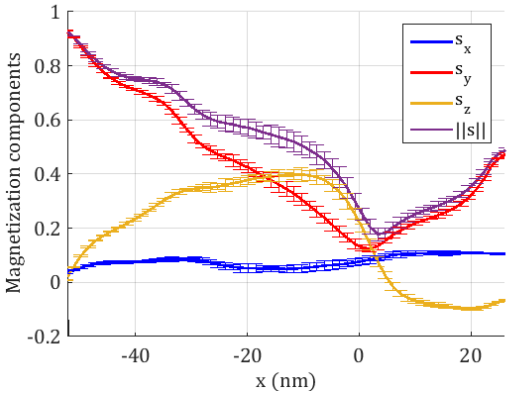

(b) S_y Injection

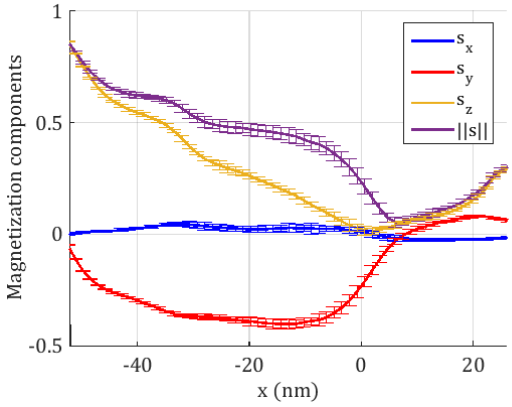

(c) S_z Injection

Figure 21: Time slice at 8 ps showing x, y and z components of the magnetization for S_x, S_y and S_z injection against position (x) in the device channel. The Error bars show the standard deviation in the mean over 10 simulation runs.

The case is much the same for both S_y and S_z injections with both showing similar non-uniform magnetisation decay followed by a recovery at the drain (with S_y injection leading to a more significant recovery when compared to S_x or S_z). We can also see from the behaviour of the vector components that as we move across the device, the Bloch vector undergoes a coherent rotation. This rotation can also be seen in Figure 21b where a marked rise in S_z accompanies the initial in decay in S_y.

Since there are no external magnetic fields, this rotation (and recovery) must be caused by spin-orbit coupling as the electrons travel through the channel. The strength of the spin-orbit coupling is in turn dependant upon the strength of the electric field due to the applied gate

and source-drain bias. The effect of these voltages on the strength of the Rashba coupling is straightforward to explain since the value of the Rashba parameter α_{br} is directly dependant on the strength of the electric field in the y-direction (see Equation (72) in section 3). A plot of the calculated value of α_{br} with the position in the 2D-channel can be seen in Figure 22. As expected α_{br} is highest in the region underneath the gate (Reaching a peak value of 39 meV Å) due to the high field in the y-direction underneath the gate. Thus we should see more of a rotation in this region of the channel due to the stronger Rashba coupling. However, we should also see an increase in the strength of both coupling mechanisms in this region due to the increased scattering in the presence of the higher electric field. This will indirectly control the strength of the spin-orbit coupling due to the more substantial increase in the random changes in the value of the $\boldsymbol{k}$-vector (which is the ultimate cause of D'yakanov-Perrel dephasing, see section 2.4.2).

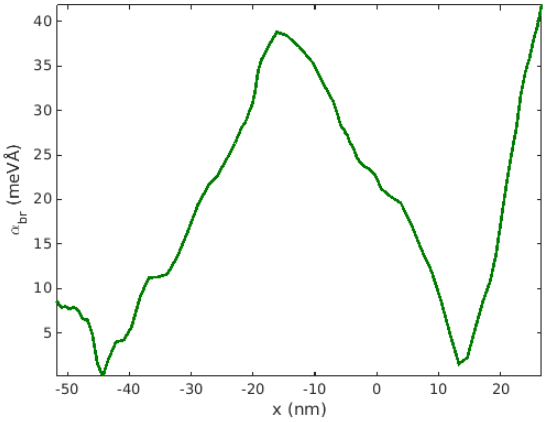

Figure 22: Plot of Rashba parameter α_{br} against position in the 2D channel.

To help visualise the rotation of the Bloch vector due to the spin-orbit coupling we will map the Bloch vector onto a new set of axes X', Y' and Z' and use spherical polar coordinates to describe the relative rotation of each injected state (see Figure 23). The injection direction is mapped to X' while the two orthogonal directions are mapped to Y' and Z' which in turn define the azimuth (θ) and elevation (ϕ) angles.

Figures 24a to 24c show how the average rotation angle for the S_x, S_y and S_z injection states vary with position. For the S_x injection case (Figure 24a) we can see an increase in the azimuth angle θ, indicating a rotation of the Bloch vector in the X'-Y' plane from 3.6° to maximum of 8.7° as we move across the channel (this corresponds to an increase in the S_y component and a decrease in S_x of the Bloch vector see Figure 23).

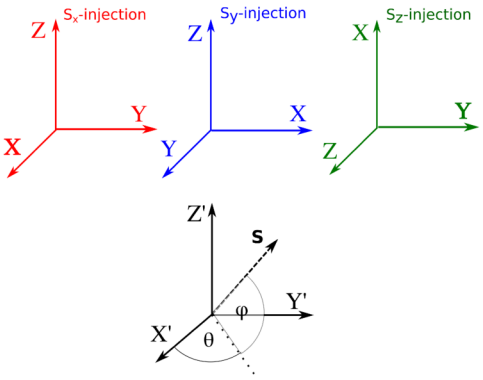

Figure 23: Diagram showing the azimuthal (θ) and elevation (ϕ) angles used for the rotational analysis (bottom black axes). The injection direction for each case is mapped to the X' axis, the result of this mapping for each case are shown in the three sets of axes at the top of the figure. With (moving from left to right) red for the x, blue for the y and green the z-injection cases.

The direction of this rotation is then reversed from around ($x = 10\,\text{nm}$) as the electrons approach the drain (corresponding to the recovery in magnetisation seen in Figure 21a) leading to a net rotation of 15° at the drain edge.

For the elevation angle ϕ (corresponding to a rotation out of the X'-Y' plane) the value initially decreases and then fluctuates around $-4°$. It then quickly rises as the electrons approach the left-hand side of the gate ($x = 26\,\text{nm}$) reaching a maximum value around the centre of the gate ($x = -10\,\text{nm}$) of 7.1°. The angle finally rapidly decreases as the electrons pass the right-hand side of the gate before eventually rising as the electrons approach the drain, leading to a net rotation of 2° at the drain edge.

For the S_y injection (Figure 24b) we see θ slowly increase from an value of 2.7° at the source ($x = -52\,\text{nm}$) to 9.8° at the left hand side of the gate ($x = -26\,\text{nm}$), again this is a rotation in the X'-Y' plane only in this injection case this corresponds to an increase in the S_x and a decrease in the S_y components of the Bloch vector. The angle then fluctuates around 10° before rapidly rising to a peak of 37.9° upon reaching the right-hand side of the gate ($x = 0\,\text{nm}$). The rotation then reverses direction, and the angle slowly decreases to reach a final net rotation of 12.9° at the drain edge.

For ϕ, however, the behaviour is very different. In this case, we see a steady rise from 3.6° at the source to 36.8° at the left-hand side of the gate (i.e. rotation out of the X'-Y' plane corresponding to an increase in S_z and decrease in S_y and S_x). This rise reaches a

peak of 60° around the right-hand side of the gate before rapidly decreasing to a low of −19° and before finally recovering slightly to a net rotation of −7.5° at the drain.

For the final case S_z (Figure 24c) we see θ steadily decrease from −8° at the source to a low of −89.1° at the right-hand side of the gate. This again a rotation in the X'-Y' plane, in this case corresponding to a decrease in both the S_z and S_y components of the Bloch vector. However, once the electrons cross the right-hand side of the gate at the rotation rapidly reveres direction, and θ rises to a maximum of 35.5° before finally decreasing to a net rotation of 12.1° at the drain. ϕ on the other hand slowly increases from 0.1° at the source to around 4° before decreasing to a low of −27.1° as the electrons pass the right-hand edge of the gate. The value then quickly recovers to a final net rotation −2.9° of at the drain edge.

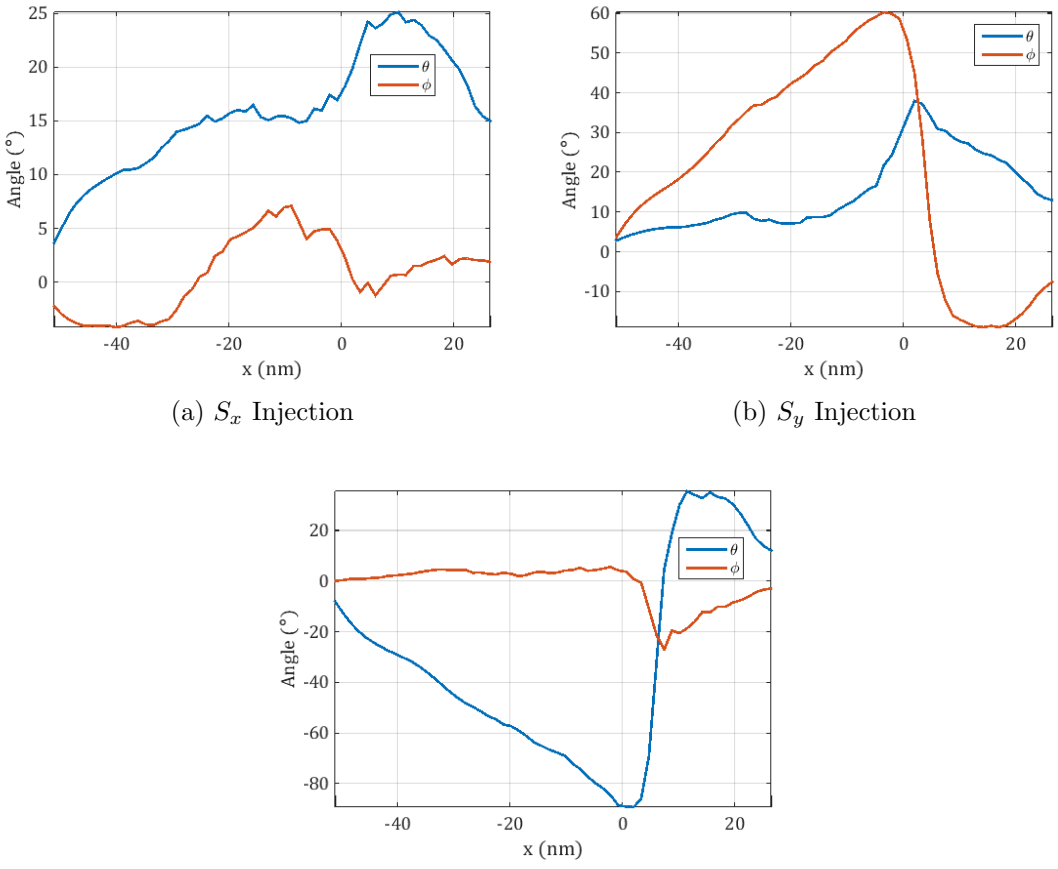

(a) S_x Injection

(b) S_y Injection

(c) S_z Injection

Figure 24: rotation angles θ and ϕ vs position in the channel for S_x, S_y and S_z injection.

To help explain the origin of this rotation further, we can calculate the components of the

Rasha and Dresselhaus spin-orbit coupling Hamiltonians for each electron n in the channel as:

$$\begin{aligned}
\boldsymbol{H}_R^{(n)} &= (\mathrm{Tr}(H_R\sigma_x), \mathrm{Tr}(H_R\sigma_y), \mathrm{Tr}(H_R\sigma_z)) \\
&= 2\alpha_{br}(k_z, 0, -k_x), \\
\boldsymbol{H}_D^{(n)} &= (\mathrm{Tr}(H_D\sigma_x), \mathrm{Tr}(H_D\sigma_y), \mathrm{Tr}(H_D\sigma_z)) \\
&= 2\gamma\langle k_y^2\rangle(-k_x, 0, k_z)
\end{aligned} \tag{138}$$

Figure 25 shows the Dresselhaus vectors $\boldsymbol{H}_D^{(n)}$ (as blue arrows) for all of the electrons at four different x-positions along the channel for one Monte Carlo run. The average value is also plotted as a red arrow. For $x = -55\,\mathrm{nm}$ the field vectors are randomly oriented. Thus we see a vanishing mean field and the electrons in the slice experience rotations due to spin-orbit coupling about a randomly oriented axis. For $x = -20\,\mathrm{nm}$ (corresponding to a region underneath the gate) there is less spread in the individual field vectors. This leads to on average a non-vanishing field vector, and thus the rotations are not completely random, and we instead see a net coherent rotation of the spin ensemble. This effect is further illustrated by Figure 26 which shows how the average spin-orbit coupling Hamiltonians vary across the different regions of the device channel. From this, we can see the strength of both Hamiltonians is lowest in the vicinity of the source and drain contacts. However, the strength of the Hamiltonians are significantly higher in the region underneath the gate and at the edges of the three electrodes (corresponding to the high fringe fields in these regions). This correlation strongly indicates that the amount of coherent rotation experienced is dependant upon the strength of the electric field.

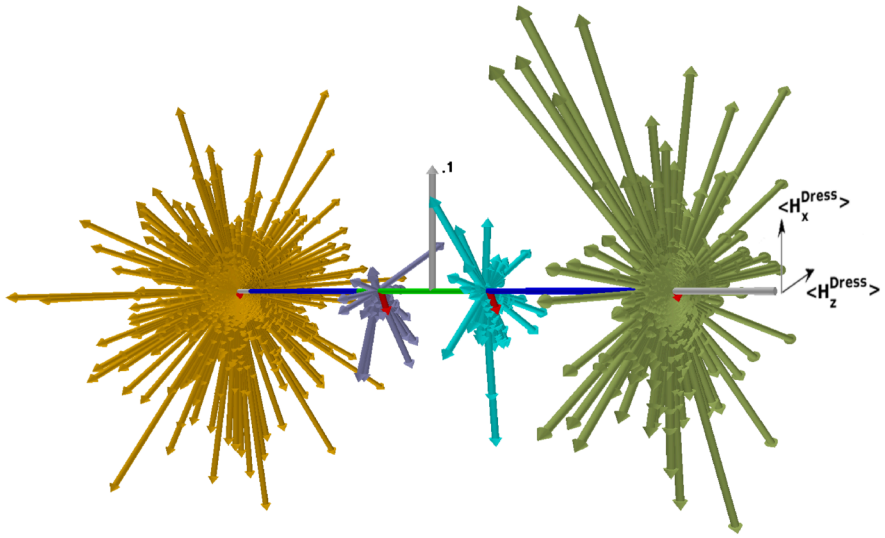

Figure 25: (a)Dresselhaus Hamiltonian vectors (in units of meV) of four electron ensembles corresponding to thin slices along the channel for a single Monte Carlo run ($V_{\mathrm{G}} = 0.9\,\mathrm{V}, V_{\mathrm{D}} = 0.5\,\mathrm{V}$) orange (far left) x=$-52$ nm, rich-blue (centre-left) x=-20 nm, cyan (centre right) x=0 nm, forest green (far right) x=26 nm. grey arrow show the scale whilst red arrows show the average.

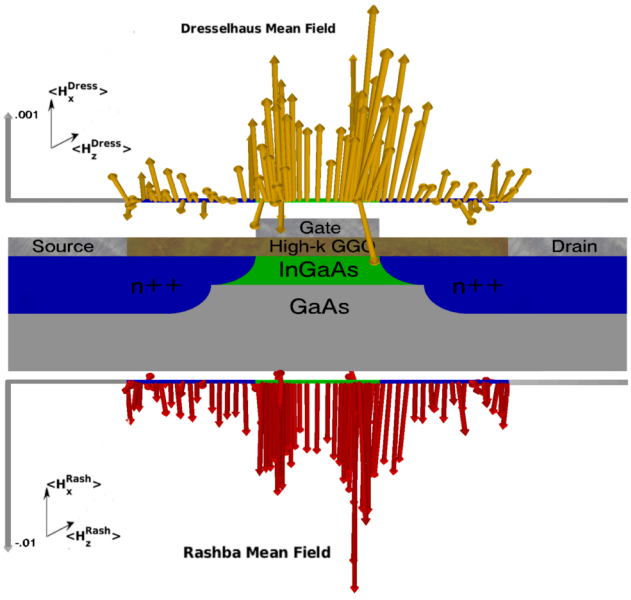

Figure 26: Rashba and Dresselhaus mean field vectors $\boldsymbol{H}_R$ and $\boldsymbol{H}_D$, obtained by averaging over all particles in thin slices across the channel for a single Monte Carlo run ($V_{\mathrm{G}} = 0.9\,\mathrm{V}, V_{\mathrm{D}} = 0.5\,\mathrm{V}$). The z-axis is in the plane perpendicular to the channel, but for the vector plots the axes have been rotated so that H_z is in the vertical direction for visual clarity.

5.4 Effects of Voltage variation

The next step in our investigation was to examine the effect on the spin of varying the applied gate (V_G) and source-drain (V_{SD}) Voltages. In theory, a higher gate voltage will lead to a higher electric field in the channel which will, in turn, increase the spin-orbit coupling strength in the channel leading to a larger rotation of the Bloch vector at the drain. Meanwhile, a higher source-drain voltage will affect the direction and length of the Bloch vector at the drain, since it will increase the x-velocity of the electrons as they move through the channel. This will indirectly affect the Bloch vector in two ways firstly the higher x-velocity will decrease the amount of time that the electrons are subjected to the field from the gate contact (thus reducing the amount of rotation experienced). It will also, however, have the effect of increasing the amount of scattering due to increased current flow. Thus the overall length of the Bloch vector will reduce due to the loss of coherence from the increased random scattering events.

Put together this means that the gate and source-drain voltages could be used as an easy method for controlling the amount and direction of the Magnetisation observed at the drain without the use of an external magnetic field.

Gate Voltage Dependence: Figure 27 shows a plot of the total magnetisation (averaged over ten runs) against the position in the channel for each of the three injection cases at gate voltages between 0.5 and 0.9 V. These were taken after a steady state had been reached at $t = 8$ ps with a fixed source-drain voltage of 0.9 V. For all three cases, we see that the initial rate of decay is is faster for lower gate voltages (with the S_x case showing the most pronounced difference). This decreased decay rate is likely due to the increased electric field produced by the higher gate voltages resulting in the electrons experiencing a higher acceleration. The electrons thus are spending less time travelling through the device channel and as such are experiencing fewer scattering events resulting in less spin dephasing as they travel through the channel. The recovery on the approach to the drain, however, is less straightforward to explain. For all three injection cases, we see that the amount of magnetisation recovery appears to have a small dependence on the applied gate voltage.

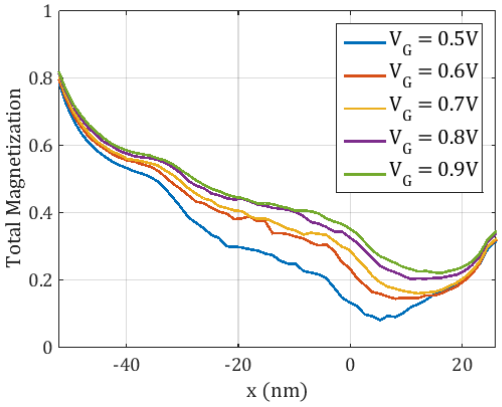

(a) S_x Injection

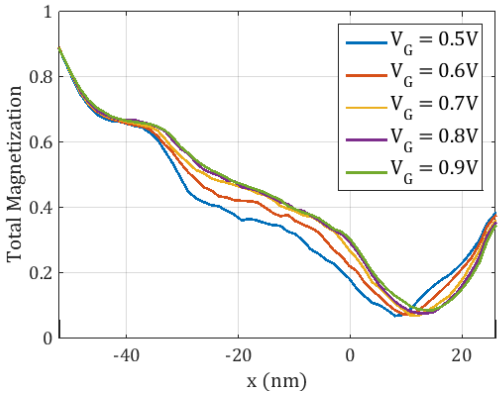

(b) S_y Injection

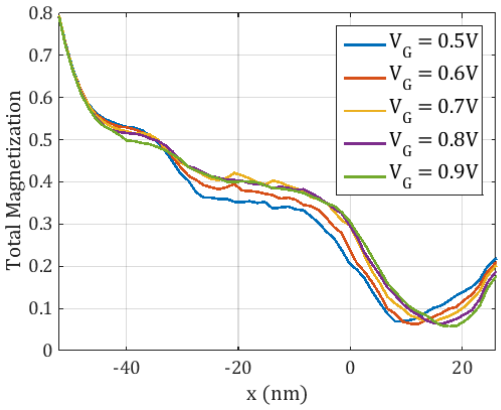

(c) S_z Injection

Figure 27: Total magnetization versus position along the channel after steady-state has been reached at different gate voltages (V_G) and a fixed source-drain voltage (V_D) of 0.9 V.

Figure 28 shows the total magnetisation vs position in the channel for two voltages $V_G = 0.5$ and $V_G = 0.9$ with error bars to indicate the standard deviation in the average over the ten simulation runs (in this case only two voltages were chosen to aid visual clarity). The standard deviation is generally quite low, indicating a low dispersion in the data from the mean value. However, the deviation is significantly higher in the centre of the channel. This increase is due to the electron density being much lower in the centre of the channel when compared to the left and right-hand sides (see Figure 18c).

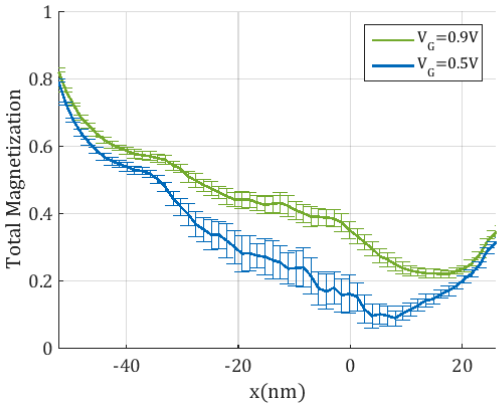

(a) S_x Injection

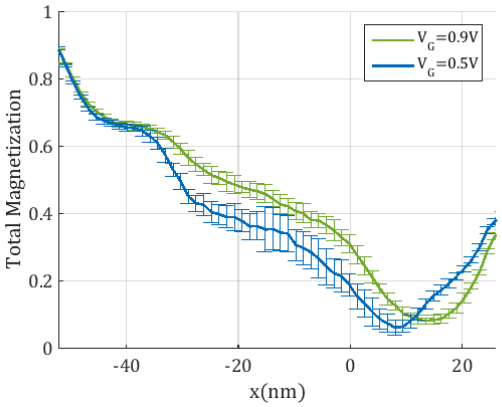

(b) S_y Injection

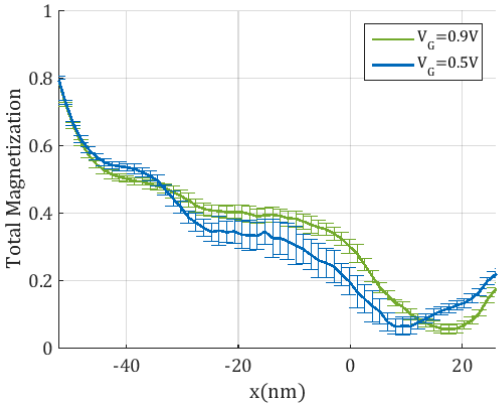

(c) S_z Injection

Figure 28: Total magnetization versus position along the channel for $V_G = 0.5$ and $0.9\,\mathrm{V}$ after steady-state has been reached for a fixed source-drain voltage (V_D) of $0.9\,\mathrm{V}$. The error bars show the standard deviation in the mean over 10 simulation runs.

The total magnetization at the drain edge ($x = -26\,\mathrm{nm}$), alongside the rotation angles θ and ϕ for each applied gate voltage are shown in Figure 29. For the S_x injection case we see that the magnetisation recovers to between $31-34\%$ of its initial value and that the recovery increases linearly with applied voltage. However, for the S_y and S_z case the magnetisation decreases linearly with V_G, reaching values of $34-38\%$ and $17-21\%$ respectively.

The rotation angles show much the same story whereby for the S_x injection case we see a linear increase in the azimuth angle (θ) indicating a voltage-dependence on the rotation of the Bloch vector in the X'-Y' plane (in this case we see an increase the S_y and corresponding decrease in the S_x components of the Bloch vector). We also see a minimal increase in the

elevation angle (ϕ) indicating a smaller voltage dependence on the out of plane Rotation (i.e. an increase in the S_z component). For S_y injection we see a similar increase in θ (again voltage dependant X'-Y' rotation but this time corresponding a to decrease in S_y and an increase in S_x). We also see a similarly small increase in ϕ (although the actual values at the drain are much lower indicating that the large out of plane rotation slightly decreases with applied gate voltage). Finally for the S_z injection we see a linear decrease in θ corresponding to a voltage-dependent rotation in the X'-Y' plane (increase in S_y with a decrease in S_z) alongside a similar linear decrease in ϕ indicating a voltage-dependent rotation out of the X'-Y' plane (in this case corresponding to a decrease in S_x). Fitting parameters and adjusted R^2 values for all the interpolation lines are given in Table 4 Appendix B.

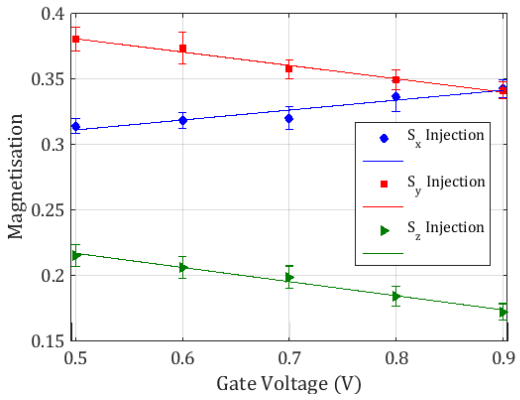

(a) Total magnetization ($|S|$)

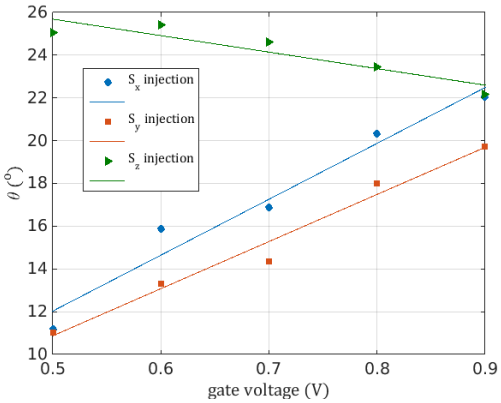

(b) Azimuth angle (θ)

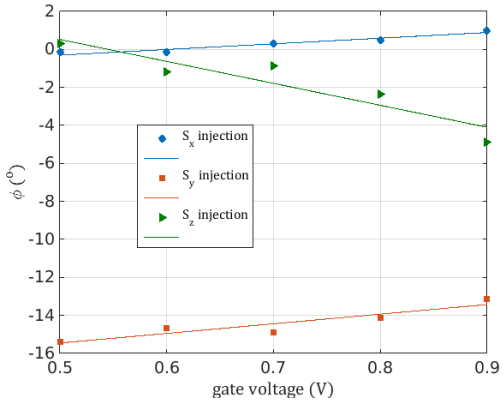

(c) Elevation angle (ϕ)

Figure 29: Total magnetization ($|S|$), azimuth angle (θ) and elevation angle (ϕ) at the drain edge ($x = 26\,\text{nm}$) as a function of applied gate voltage (V_G) for a fixed source-drain voltage (V_D) of 0.9 V.

The voltage dependence on the recovery can be attributed to the difference in the strength of the spin-orbit coupling experienced by the electrons in the channel due to the difference in the strength the electric field generated by the gate contact.

Figures 30 shows plots of the total electric field, its $x-y$ components and the estimated value of the Rashba parameter α_{br} respectively, with the applied gate voltage and position in a thin slice across the centre of the channel (located at $y = -11.5\,\text{nm}$). From these, we can see that the Electric field the left-hand side of the gate ($x = -26\,\text{nm}$) increases with increasing applied gate voltage as expected due to the increased contribution from the y-component (Figure 30c).

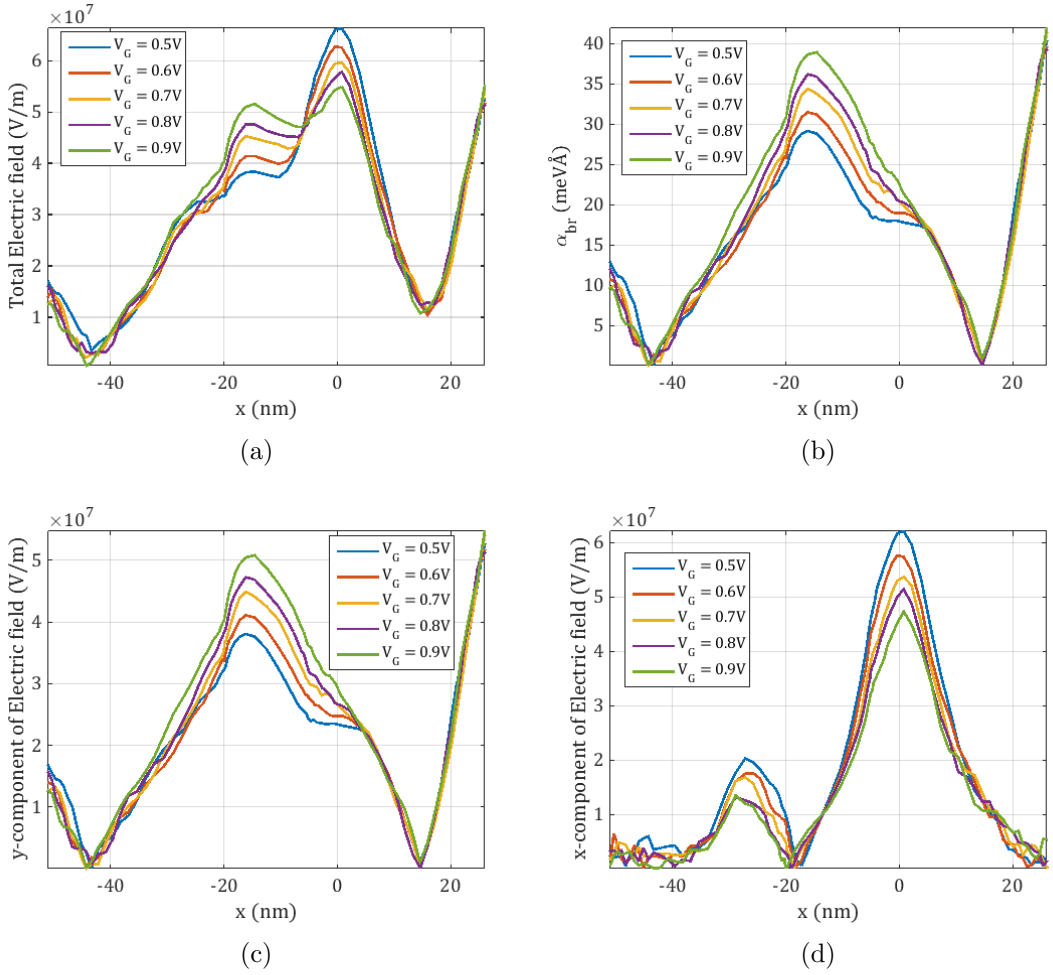

Figure 30: Electric field (a) and corresponding Rashba coefficient α_{br} across the device the channel for various applied gate voltage (V_G) for a fixed source-drain voltage (V_D) of 0.9 V.

The peak at the right-hand side of the gate, however, is more complicated. Due to the relatively high source-drain voltage of 0.9 V there is a high fringing field at the right-hand side of the gate this causes a massive peak in the x-component of the field for $V_G = 0.5\,\mathrm{V}$ of $6.6 \times 10^7\,\mathrm{V\,m^{-1}}$ which decreases with increasing gate bias.

Figure 31 shows the average electric field in the y-direction in the region underneath the gate this appears to increase linearly with the gate bias. Therefore electrons that pass underneath the gate will on average experience a higher field (and thus stronger spin-orbit coupling) for a more extended period at higher applied gate voltages.

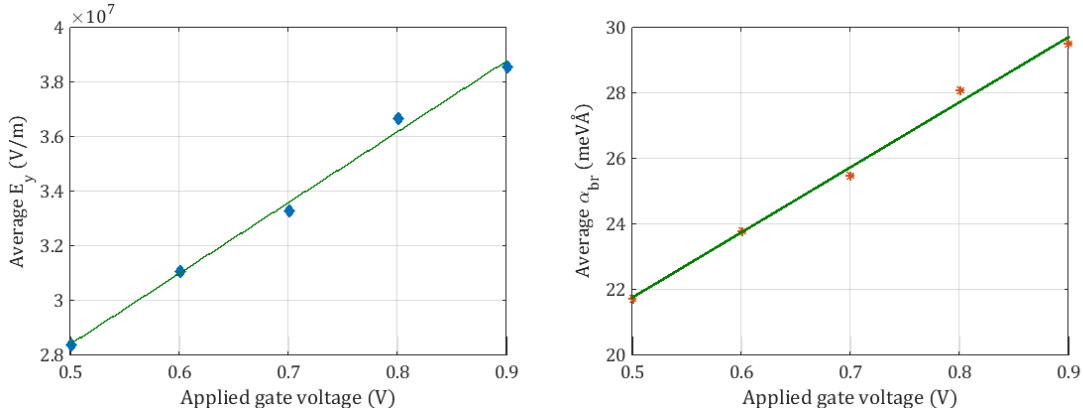

(a) (b)

Figure 31: Average electric field in the y-direction and corresponding Rashba coefficient (α_{br}) in the region of the channel underneath the gate as a function of applied gate voltage (V_G) for a fixed source-drain voltage (V_D) of 0.9 V.

Source-Drain Voltage Dependence: Figure 32 shows the magnetisation against the position in the channel for the three different injection cases. The source-drain voltage (V_D) was varied between 0.5 and 0.9 V whilst the gate voltage was kept fixed at 0.9 V.

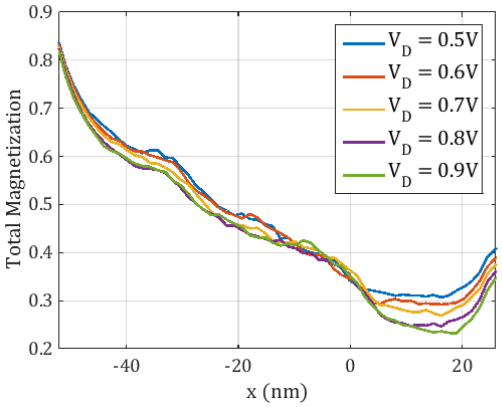

(a) S_x injection

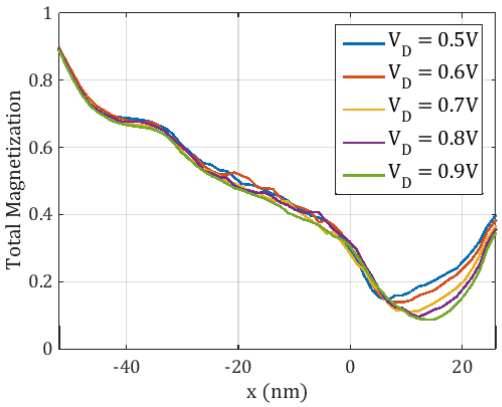

(b) S_y injection

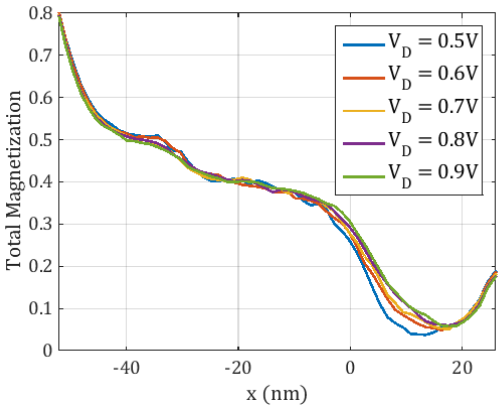

(c) S_z injection

Figure 32: Total magnetization versus position along the channel after steady-state has been reached for various source-drain voltages (V_D) with a fixed gate voltage (V_G) of 0.9 V.

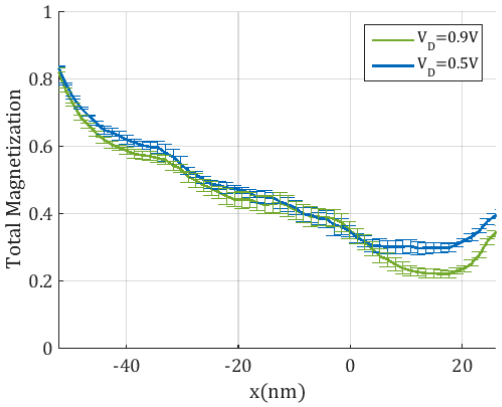

(a) S_x injection

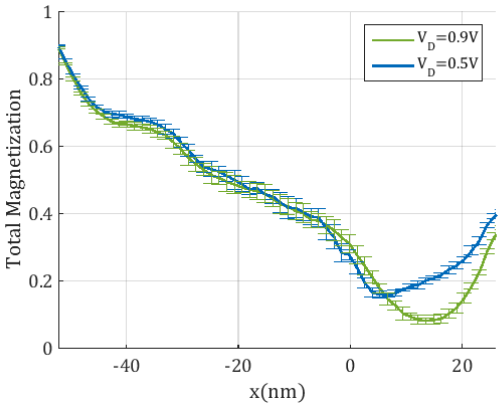

(b) S_y injection

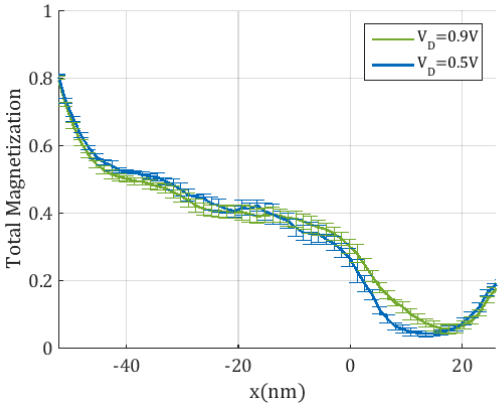

(c) S_z injection

Figure 33: Total magnetization versus position along the channel for $V_D = 0.5$ and 0.9 V for a fixed Gate voltage (V_G) of 0.9 V. The error bars show the standard deviation in the mean over 10 simulation runs.

For all three injection cases, we observe that the magnetization only significantly varies with applied V_D in the region between the gate and the drain (between $x = 0$ and 26 nm). This makes physical sense as the electric field experienced by the electrons will be far more significantly influenced by the source-drain voltage in the region near the drain.

For the S_x and S_y cases (Figures 32a and 32b) we observe a source-drain voltage dependence on both the rate of decay in the magnetisation in the drain region and the recovery at the drain edge. With higher applied V_D leading to faster decay and a lower drain-edge recovery. However, the S_z case appears to show no source-drain voltage dependence for the rate of decay or the final value at the drain.

Figure 33 shows the total magnetisation vs position in the channel for two voltages $V_D = 0.5\,\mathrm{V}$ and $V_D = 0.9\,\mathrm{V}$ with error bars to indicate the standard deviation in the average over the ten simulation runs (in this case only two voltages were chosen to aid visual clarity). The standard deviation is generally quite low, indicating a small dispersion in the data from the mean value. However, we can also see that the standard deviation is significantly higher in the centre of the channel. This increase is due to the electron density being much lower in the centre of the device channel when compared to the left and right-hand sides (see Figure 18c).

The total magnetisation at the drain edge ($x = 26\,\mathrm{nm}$), alongside the rotation angles θ and ϕ for each applied source-drain voltage, are shown in Figure 34a. For both the S_x and S_y cases we see that the magnetisation recovery decreases linearly with V_D, reaching between 41 and 34% of the initially injected value. Conversely, the S_z case shows no V_D dependence on the recovery with the final values fluctuating around 17% regardless of applied V_D.

The rotation angles (Figure 34b and 34c) also appear to show a similar dependence on V_D. The S_x and S_y cases show θ linearly decreasing from 23° to 22° and 21.5° to 19.7° respectively. ϕ also decreases linearly with applied voltage from 3.8° to 0.5° for S_x and $-10.1°$ to $-13.2°$ for S_y. The S_z case, however, indicates a small linear increase from $-6.1°$ to $-5.2°$ with applied voltage for ϕ and shows a highly non-linear voltage dependence for θ (with a very close fit obtained from a cubic polynomial). Fitting parameters and adjusted R^2 values for all the interpolation lines are given in Table 5 Appendix B.

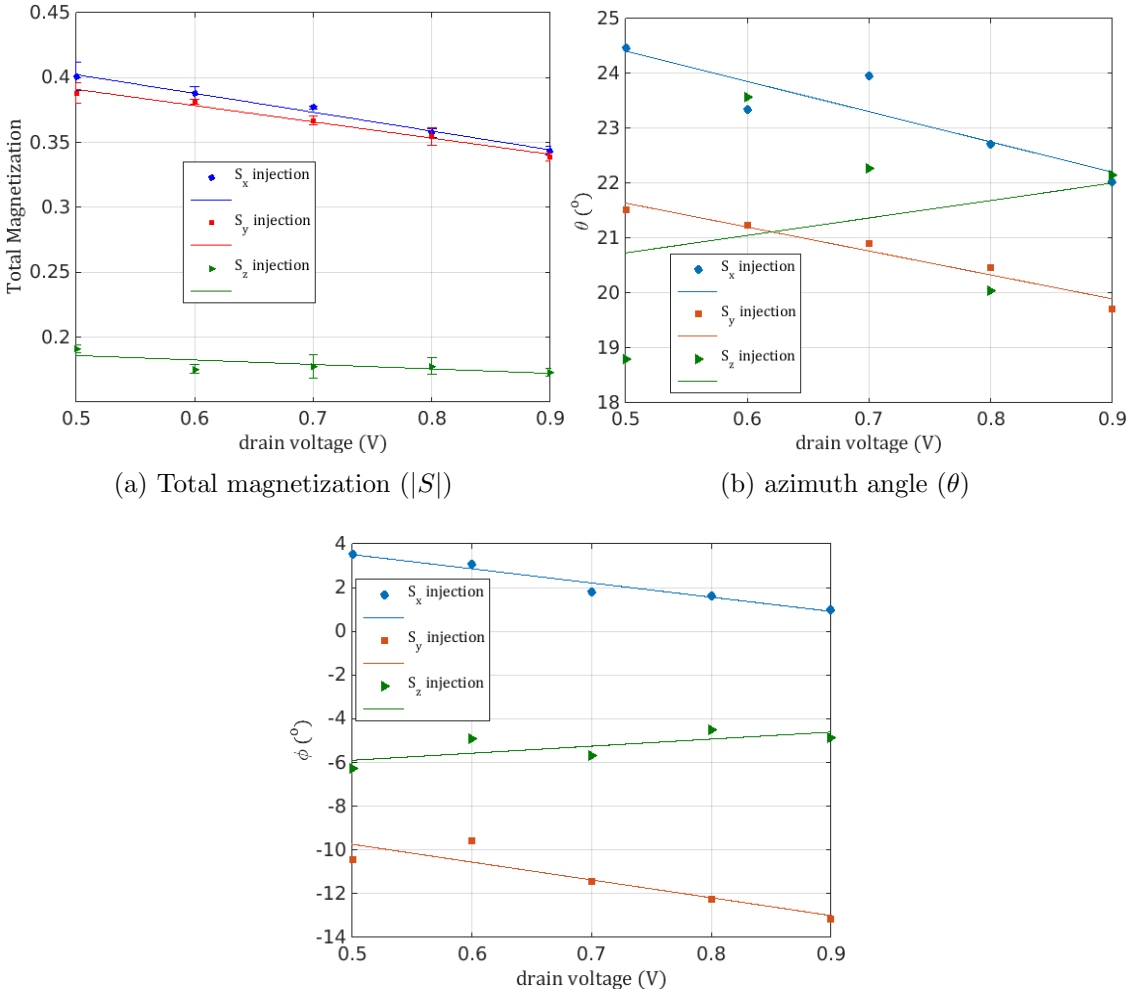

(a) Total magnetization ($|S|$)

(b) azimuth angle (θ)

(c) elevation angle (ϕ)

Figure 34: Total magnetization ($|S|$), azimuth angle (θ) and elevation angle (ϕ) at the drain edge ($x = 26\,\text{nm}$) as a function of applied gate voltage (V_G) for a fixed source-drain voltage (V_D) of 0.9 V.

Once again the voltage dependence on the recovery can be attributed to the difference in the strength of the spin-orbit coupling experienced by the electrons in the channel only this time due to the difference in the strength the electric field generated by the drain bias.

Figure 35 shows plots of the total electric field, its $x - y$ components and the estimated value of the Rashba parameter α_{br} respectively, with applied source-drain voltage and position in a thin slice across the centre of the channel. From these, we can see that the total Electric field rises slightly at the left-hand side of the gate with increasing V_D but then sharply decreases at the right-hand side. The decrease on the left-hand side is due to the

slight change in the height of the central peak in the y-component of the field (Figure 35c). Whilst the increase on the right-hand side is due to the increasing source-drain bias causing an increase in the right-hand peak of the x-component of the field (Figure 35d). The lower peak in the y-component also leads to a small decrease in both the average electric field and the corresponding Rashba coupling strength in the region underneath the gate as shown in Figures 36a and 36b.

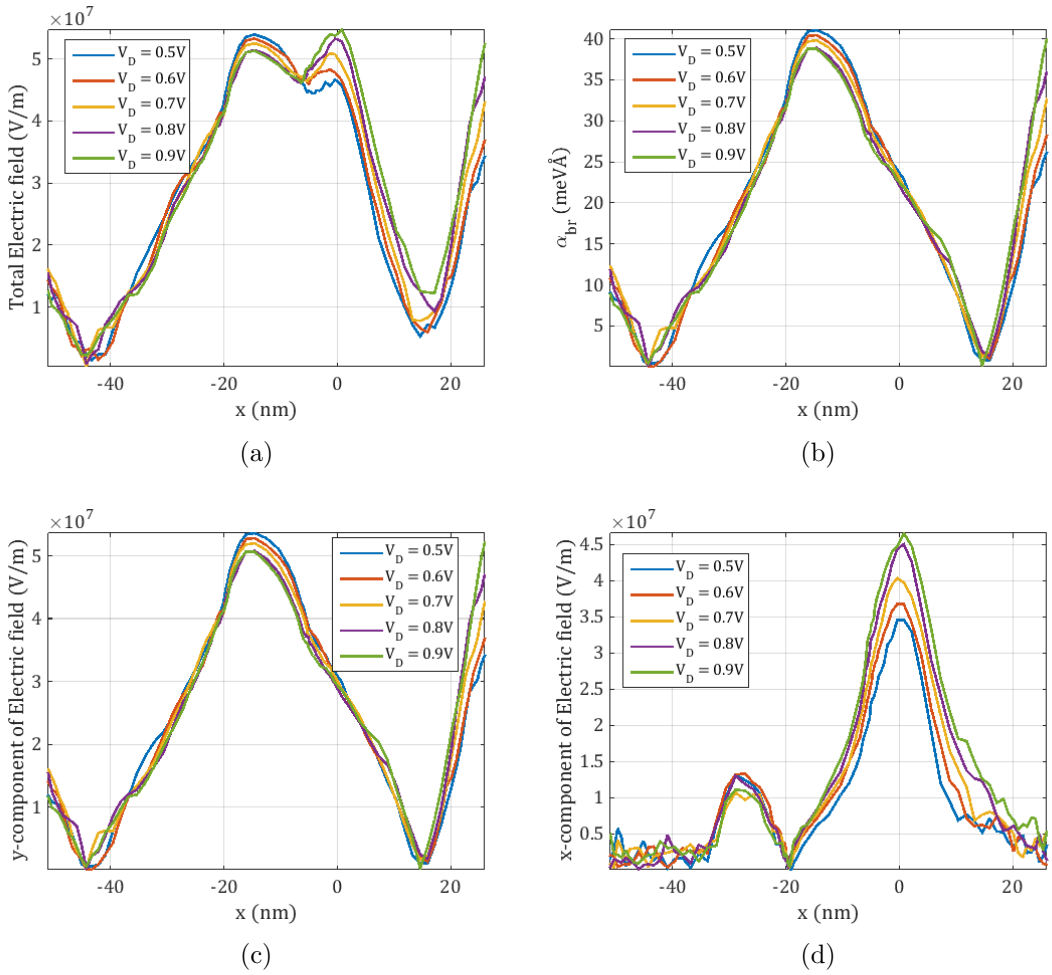

Figure 35: Total electric field, $x - y$ components and corresponding Rashba coefficient α_{br} across the device the channel for various applied source-drain voltages (V_D) for a fixed gate voltage (V_G) of 0.9 V.

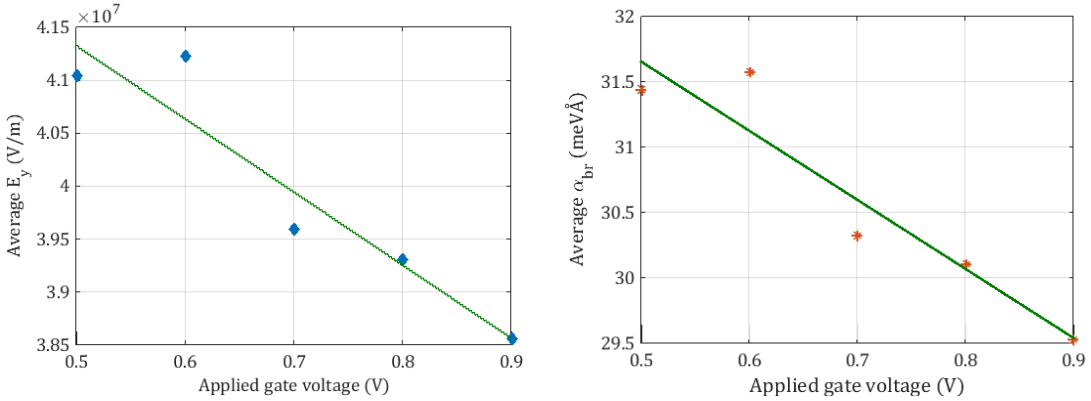

(a) (b)

Figure 36: Average electric field in the y-direction and corresponding Rashba coefficient (α_{br}) in the region of the channel underneath the gate as a function of applied source-drain voltage (V_D) for a fixed gate voltage (V_G) of 0.9 V.

6 Effects of Strain and Lattice Temperature

6.1 Strain Effects

We next investigated the effects of mechanical strain applied to the device channel. Strain alters both the symmetry of the bulk crystal and the interband energies E_0, E_1, Δ_0 and Δ_1 thus applied strain will alter the amount of both the Dresselhaus and Rashba coupling. Therefore, by carefully controlling both the amount and direction of the applied strain we have a potential means to control both the amount of spin-orbit coupling in the channel and the magnetisation observed at the drain.

Although we could in principle consider the effects of both tensile and compressive strain in our model, we will only consider the compressive strain. This is because tensile strain applied to the channel will reduce the electron mobility by increasing the effective mass in the X-valley and increasing the rate of electron scattering with phonons, interface roughness and ionised impurities [70, 74]. This will result in slower transport across the channel, and as such we would expect to see an increase in the spin relaxation suppressing the observed spin recovery.

To account for the effects of mechanical strain on the spin-orbit coupling, we will need

to modify our $\boldsymbol{k} \cdot \boldsymbol{p}$ approach outlined in chapter 2 to include the impact of compressive strain on the bandstructure (and ultimately the obtained values of α_0 and γ). To this end we follow the method laid out by Pikus and Bir [57] consisting of adding an extra term to each element of the unstrained Hamiltonian H_0, created by replacing $k_x k_y$ (and it's circular permutations) with the component of the strain tensor ϵ_{xy} and the Luttinger parameters with deformation potentials.

To obtain the strain tensor for compressive strain in the [001],[110] and [111] directions we first took a small change in the lattice spacing a_s of between 0% and 4% of the unstrained lattice constant a_0. The strain parallel ($e_\parallel$) and perpendicular ($e_\perp$) to the applied force can then be calculated as:

$$\begin{aligned} e_\parallel &= \tfrac{a_s}{a_0} - 1 \\ e_\perp &= -D_{[hkl]} e_\parallel, \end{aligned}$$

where h,k and l are miller indices for the direction of the strain. The co-efficient $D_{[hkl]}$ for the three considered directions is given by

$$D_{[001]} = \frac{2C_{12}}{C_{11}} \tag{139a}$$

$$D_{[110]} = \frac{C_{11} + 3C_{12} - 2C_{44}}{C_{11} + C_{12} + 2C_{44}} \tag{139b}$$

$$D_{[111]} = \frac{2C_{11} + 4C_{12} - 4C_{44}}{C_{11} + 2C_{12} + 4C_{44}}, \tag{139c}$$

where C_{11}, C_{12} and C_{44} are material dependant elastic constants.

This then allows us to calculate the 3×3 strain tensor $e_{[hkl]}$ as

$$\epsilon_{[001]} = \begin{pmatrix} e_1 & 0 & 0 \\ 0 & e_1 & 0 \\ 0 & 0 & e_1 \end{pmatrix}, \tag{140a}$$

$$\epsilon_{[111]} = \begin{pmatrix} e_2 & e_3 & e_3 \\ e_3 & e_2 & e_3 \\ e_3 & e_3 & e_2 \end{pmatrix}, \tag{140b}$$

$$\epsilon_{[110]} = \begin{pmatrix} e_4 & e_5 & 0 \\ e_5 & e_4 & 0 \\ 0 & 0 & e_1 \end{pmatrix}, \tag{140c}$$

where

$$e_1 = e_\parallel, \tag{141a}$$
$$e_2 = \tfrac{1}{3}(e_\perp + 2e_\parallel), \tag{141b}$$
$$e_3 = \tfrac{1}{3}(e_\perp - e_\parallel), \tag{141c}$$
$$e_4 = \tfrac{1}{2}(e_\perp + e_\parallel), \tag{141d}$$
$$e_5 = \tfrac{1}{2}(e_\perp - e_\parallel). \tag{141e}$$

Thus we can now finally calculate the total system Hamiltonian $H = H_0 + H_\epsilon$, where H_0 is the unstrained Hamiltonian for the 14 band extended Kane system described in section 3.4 and the corresponding strain Hamiltonian H_ϵ is given by [57, 75]

$$H_\epsilon = \begin{pmatrix} H_{c\epsilon} & H_{cv\epsilon} & 0_{2\times 6} \\ H_{vc\epsilon} & H_{v\epsilon} & 0_{6\times 6} \\ 0_{6\times 2} & 0_{6\times 6} & 0_{6\times 6} \end{pmatrix}, \tag{142}$$

where $H_{vc\epsilon} = H_{cv\epsilon}^\dagger$.

Setting

$$A_\epsilon = a_c(\epsilon_{xx} + \epsilon_{yy} + \epsilon_{zz}), \qquad D_\epsilon = -a_v(\epsilon_{xx} + \epsilon_{yy} + \epsilon_{zz}),$$
$$G_\epsilon = -b(\epsilon_{xx} + \epsilon_{yy} - 2\epsilon_{zz})/2, \qquad S_\epsilon = -d(\epsilon_{xz} - i\epsilon_{yz}),$$
$$R_\epsilon = \tfrac{\sqrt{3}}{2}b(\epsilon_{xx} - \epsilon_{yy}) - id\epsilon_{xy}, \qquad v = \tfrac{P_0}{\sqrt{6}}\sum_j(\epsilon_{xj} - i\epsilon_{yj}),$$
$$u = \tfrac{P_0}{\sqrt{3}}\sum_j \epsilon_{zj},$$

we have

$$H_{c\epsilon} = \begin{pmatrix} A_\epsilon & 0 \\ 0 & A_\epsilon \end{pmatrix}, \qquad H_{cv\epsilon} = \begin{pmatrix} \sqrt{3}v^\dagger & -\sqrt{2}u & -v & 0 & -u & -\sqrt{2}v \\ 0 & v^\dagger & -\sqrt{2}u & -\sqrt{3}v & \sqrt{2}v^\dagger & u \end{pmatrix}$$

$$H_{v\epsilon} = \begin{pmatrix} (D_\epsilon + G_\epsilon) & 0 & -S_\epsilon & R_\epsilon & -\frac{S_\epsilon}{\sqrt{2}} & \sqrt{2}R_\epsilon \\ 0 & (D_\epsilon + G_\epsilon) & R_\epsilon^\dagger & S_\epsilon^\dagger & -\sqrt{2}R_\epsilon^\dagger & -\frac{S_\epsilon^\dagger}{\sqrt{2}} \\ -S_\epsilon^\dagger & R_\epsilon & (D_\epsilon - G_\epsilon) & S_\epsilon & -\sqrt{2}G_\epsilon & \sqrt{\frac{3}{2}}S_\epsilon \\ R_\epsilon^\dagger & S_\epsilon & S_\epsilon^\dagger & (D_\epsilon - G_\epsilon) & \sqrt{\frac{3}{2}}S_\epsilon^\dagger & \sqrt{2}G_\epsilon \\ \frac{-S_\epsilon^\dagger}{\sqrt{2}} & -\sqrt{2}R_\epsilon & -\sqrt{2}G_\epsilon^\dagger & \sqrt{\frac{3}{2}}S_\epsilon & D_\epsilon - \Delta_0 & 0 \\ \sqrt{2}R_\epsilon & \frac{-S_\epsilon}{\sqrt{2}} & \sqrt{\frac{3}{2}}S_\epsilon^\dagger & \sqrt{2}G_\epsilon^\dagger & 0 & D_\epsilon - \Delta_0 \end{pmatrix}.$$

It should be noted however, that the influence of strain on the two highest p-type conduction bands (labelled Γ_{7c} and Γ_{8c} in our notation) is currently unknown. Thus the p-type conduction band hydrostatic deformation potential ($a_{\Gamma_{7c}}$ and $a_{\Gamma_{8c}}$) and p-type CB shear deformation potential ($b_{\Gamma_{7c}}$ and $b_{\Gamma_{8c}}$) have been neglected.

Figure 37 shows four plots near the Γ point for the: Γ_{6c}(conduction), Γ_{8v} (Light/Heavy hole) and Γ_{7v} (split off) bands at the bottom of the considered $In_{0.3}Ga_{0.7}As$ quantum well with compressive strain in the [001],[110] and [111] directions, equivalent to a 4% lattice mismatch. From this, we can see that all the bands shift with applied strain, with the amount begin dependant on the direction. Both the Γ_{7v} (Split-off) and the Γ_{6c} (conduction) bands decrease in energy while the Γ_{8v} doublet breaks its degeneracy at the Γ point, with the light hole band decreasing and the heavy hole band increasing in energy.

Using these calculations we extracted the new inter-band energies for the strained system E_0', E_1', Δ_0' and Δ_1'. Which we then substituted into equations (72) and (73) to calculate the spin-orbit parameters α_0 and γ as a function of applied strain. These were then finally used in the main Monte Carlo simulations to investigate the spin dynamics as a function of applied strain.

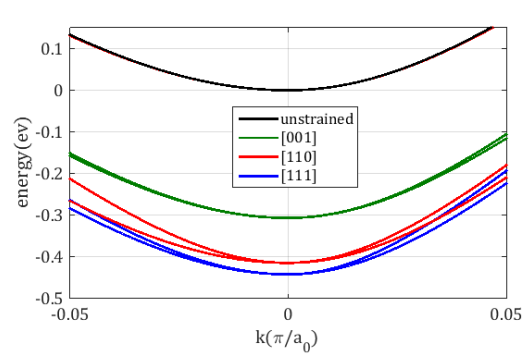

(a) Γ_{6c} (Conduction Band)

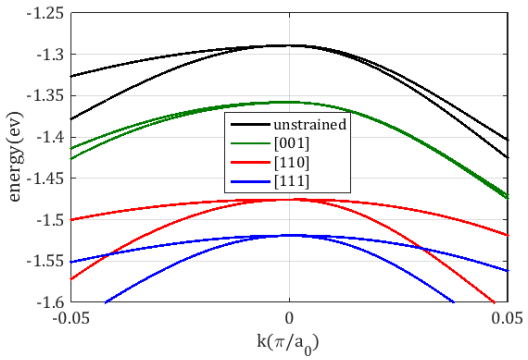

(b) Γ_{8v} (Light Hole)

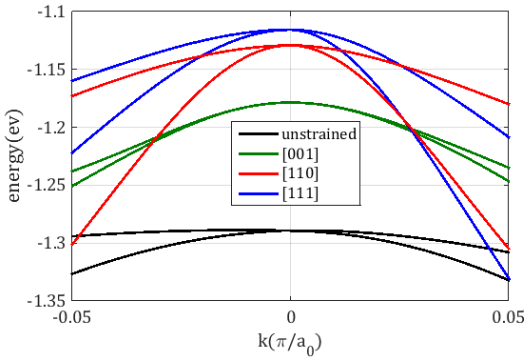

(c) Γ_{8v} (Heavy Hole)

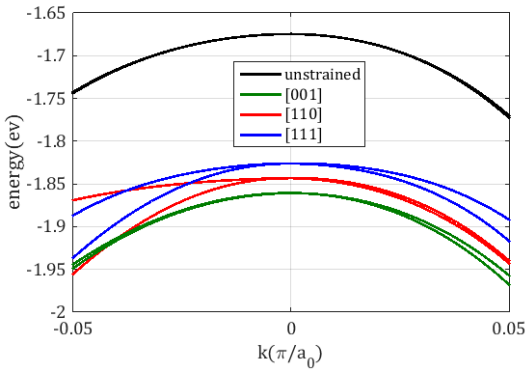

(d) Γ_{7v} (Split off)

Figure 37: Calculated band energies near the Γ point at the bottom of the considered $In_{0.3}Ga_{0.7}As$ quantum well with compressive strain in the [001],[110] and [111] directions equivalent to a 4% lattice mismatch.

The obtained values of γ and the average value of α_{br} as a function of applied strain in the [001],[110] and [111] directions are shown in Figures 38 for $V_G = 0.9V$ and $V_D = 0.9V$. As we can see the spin-orbit coupling coefficients both increase non-linearly with applied strain due to the change in the energy gap at the gamma point, E_0, between the Γ_{6c} and Γ_{7v} bands.

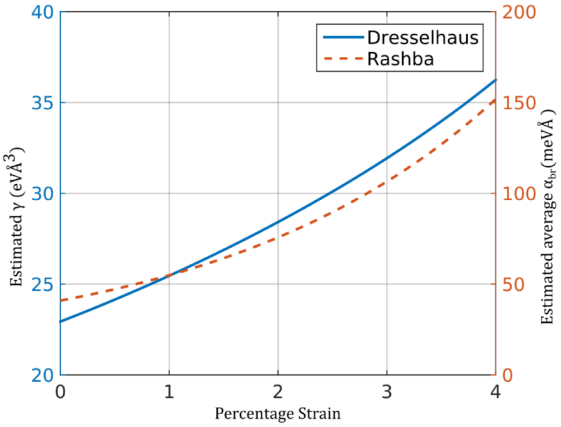

(a) Strain in [001] direction.

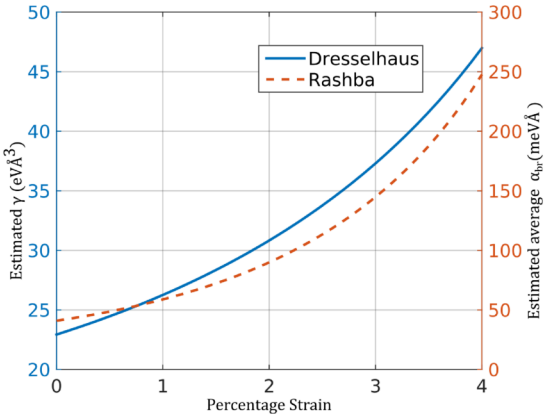

(b) Strain in [110] direction.

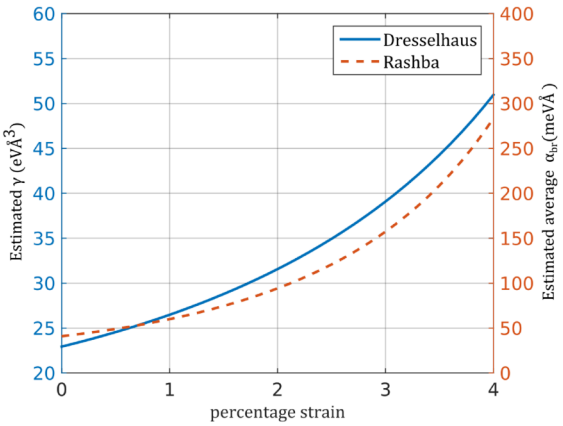

(c) Strain in [111] direction.

Figure 38: Spin-orbit coupling coefficients α_{br} and γ as a function of strain ranging from 0% to 4% for three different strain directions. α_{br} has been calculated using an electric field of $4.5 \times 10^7\,\mathrm{V\,m^{-1}}$ corresponding to the average field in region of the channel under the gate for $V_G = 0.7\,\mathrm{V}$, $V_D = 0.5\,\mathrm{V}V$.

Figure 39 shows how the total magnetisation vs position in the channel changes with applied strain. For strain in both the [001] and [110] directions we see a significant decrease in the magnetisation decay with increasing strain leading to a significantly higher magnetisation at the drain edge of 63.5% for [001] and 51% for [110] at 4% strain. Strain in the [111] direction, however, shows no significant change in the magnetisation decay or recovery at the drain. This is also shown in Figure 41 which shows the magnetisation, azimuthal (θ) and elevation (ϕ) angles at the drain edge. Figure 41a once again demonstrates the non-linear increase in the magnetisation for the [001] and [110] while the [111] direction shows

no significant dependence. Figure 41b shows a non-linear increase in the azimuthal angle θ with the applied strain in all three directions. Finally, Figure 41c shows the elevation angle only fluctuates around 1° for strain in all directions, suggesting ϕ is not significantly affected by strain.

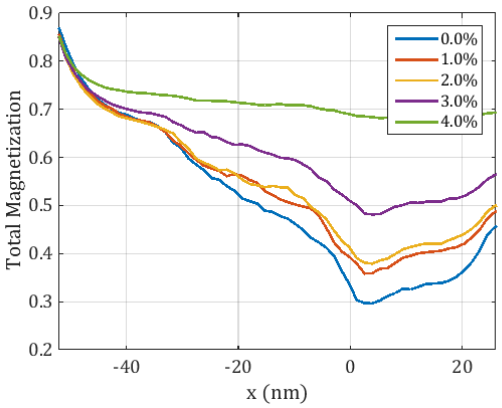

(a) Strain in [001] direction.

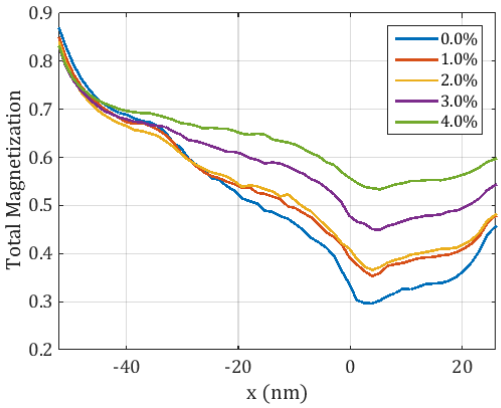

(b) Strain in [110] direction.

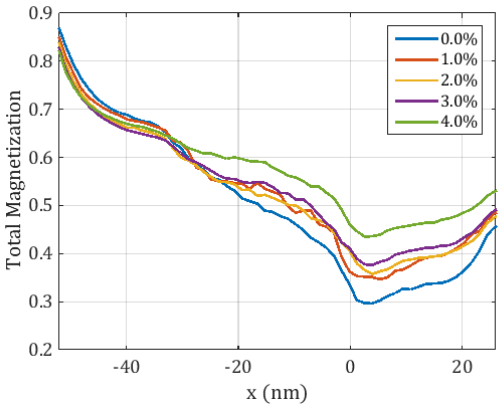

(c) Strain in [111] direction.

Figure 39: Magnetization along the device channel vs. strain ranging from $0 - 4\%$ for three different strain directions, taken after a steady state was reached at $t = 8\,\text{ps}$ for x-injection with $V_G = 0.7\,\text{V}, V_D = 0.5\,\text{V}$.

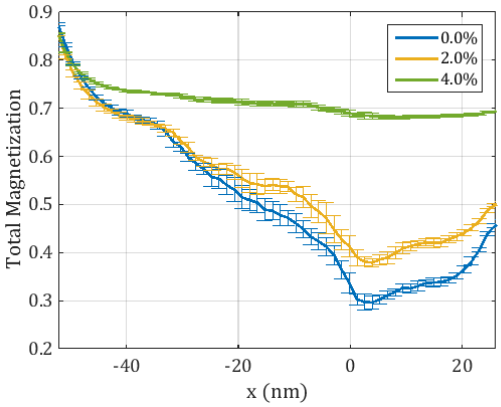

(a) Strain in [001] direction.

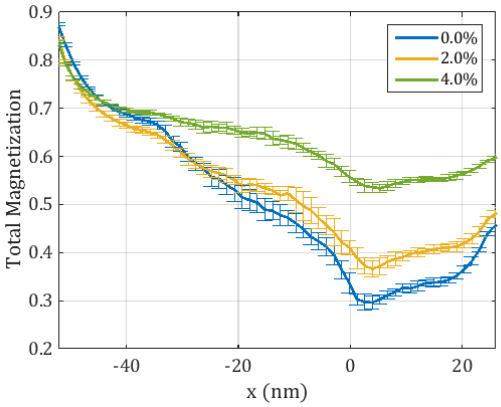

(b) Strain in [110] direction.

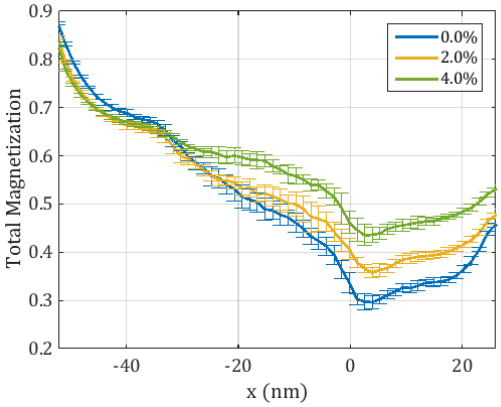

(c) Strain in [111] direction.

Figure 40: Magnetization along the device channel vs. strain equivalent to a lattice mismatch of 0%, 2% and 4% for three different strain directions, with $V_G = 0.7\,\mathrm{V}, V_D = 0.5\,\mathrm{V}$. The error bars indicate the standard deviation in the mean over 10 simulation runs.

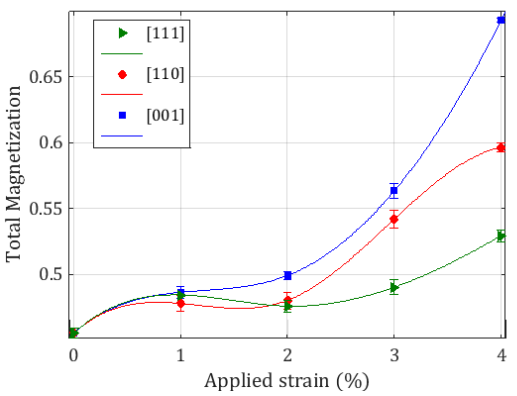

(a) Total Magnetization

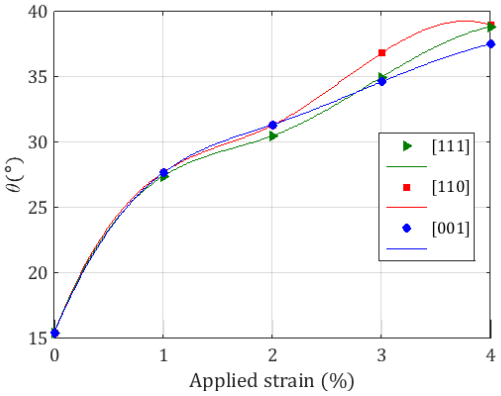

(b) Azimuthal angle

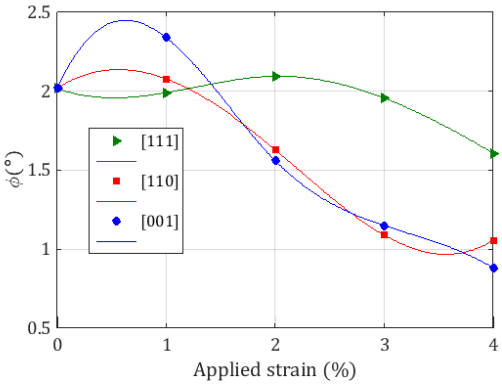

(c) Elevation angle

Figure 41: Steady state magnetization showing total magnetization (a), and azimuthal (b) and elevation angle (c) at drain as a function of strain along different axis (x-injection, $V_G = 0.7\,\mathrm{V}$,$V_D = 0.5\,\mathrm{V}$) with non-linear spline fits shown by lines to serve as a guide to the eye in elucidating trends in the data.

6.2 Temperature effects

The next step in our investigation was to study the effects of lowering the lattice temperature T. We expect the temperature to affect the magnetisation at the in two distinct ways. Firstly lowering the temperature will decrease the number of scattering events as the electrons travel through the channel, this will, in turn, decrease the amount of decay in the magnetisation leading to a higher net magnetisation at the drain. The second effect is due to both the Rashba and Dresselhaus coupling decreasing with temperature. This effect has been well studied for GaAs [76, 77] and is attributed to the temperature dependence of the lattice

constant a_0 leading to a increase in the band energies E_0, E_1, Δ_0 and Δ_1 with decreasing temperature, which leads to a change in the Dresselhaus and Rashba parameters α_{br} and γ. It should be noted at this stage however that due to a still unresolved bug in the Fermi-Dirac integral solver used in the main Monte Carlo engine we were unable to simulate lattice temperatures below 85 K reliably. Thus our work will focus on the spin-dynamics between 85 K and 300 K.

The temperature dependence of the band-gap energies for GaAs has been investigated experimentally [77, 78] from which the following generic functional relation for the temperature dependence of the band energies $E_g(T)$ has been proposed.

$$E_g(T) = E_{g0} - \alpha_B \left(1 + \frac{2}{e^{\frac{\theta}{T}} - 1}\right), \tag{143}$$

where T is the lattice temperature and the parameters E_{g0}, α_B and θ are obtained by fitting to experimental data. It was then latter shown by [77] that the Kane parameters P_0 P_1 also have a small temperature dependence of the same form as Equation (143).

The temperature dependence for InAs (and by extension InGaAs) however, is not as well documented in the literature with only limited experimental data for the fitting parameters θ and α_B being published for the inter-band energies [79, 80] and no data on the dependence of the Kane parameters P_0 and P_1. Thus more data will be needed to make more accurate predictions for low-temperature spin transport. However, our work is still useful for elucidating trends in the data and examining the general effects of temperature on the magnetisation. The fitting parameters used to calculate the band energy dependence are listed in Table 3 and for this work, we have assumed P_1 and P_0 to be temperature independent for InAs due to the lack as mentioned earlier of available data.

Figure 42 shows how the Dresselhaus (γ) and Rashba (α_{br}) coefficients vary with lattice temperature. From this, we can see that as expected both coefficients increase non-linearly due to the changes in the inter-band energies, with both varying cubically.

Parameter	GaAs[a]			InAs			$In_{0.3}Ga_{0.7}As$		
	E_{g0}(eV)	α_B(meV)	θ(K)	E_{g0}(eV)	α_B(meV)	θ(K)	E_{g0}(eV)	α_B(meV)	θ(K)
E_0	1.571	57	240	0.414[b]	28.10[b]	147[b]	1.224	48.30	212.10
E_1	4.456	59	323	4.453[c]	41.00[c]	262[c]	4.455	53.60	304.70
$E_0 + \Delta_0$	1.907	58	240	0.807[b,d]	28.10[b,d]	147[b,d]	1.577	49.03	212.10
$E_1 + \Delta_1$	4.659	59	323	4.936[e]	64.00[e]	159[e]	4.742	60.50	273.80
$2P_0^2/\hbar^2$	30.58	1040	240	-	-	-	-	-	-
$2P_1^2/\hbar^2$	8.84	1040	240	-	-	-	-	-	-

a. obtained from reference [77]

b. obtained from reference [80]

c. obtained from reference [81]

d. Due to lack of data this was assumed to have the same dependence as E_0

e. obtained from reference [79]

Table 3: Fitting parameters E_{g0}, θ, and α_B used to obtain the temperature dependant band energies and Kane parameters. Note: we have assumed that P_1 and P_0 are temperature independent for InAs and that $E_0 + \Delta$ has the same temperature dependence as E_0 due to the aforementioned lack of available data.

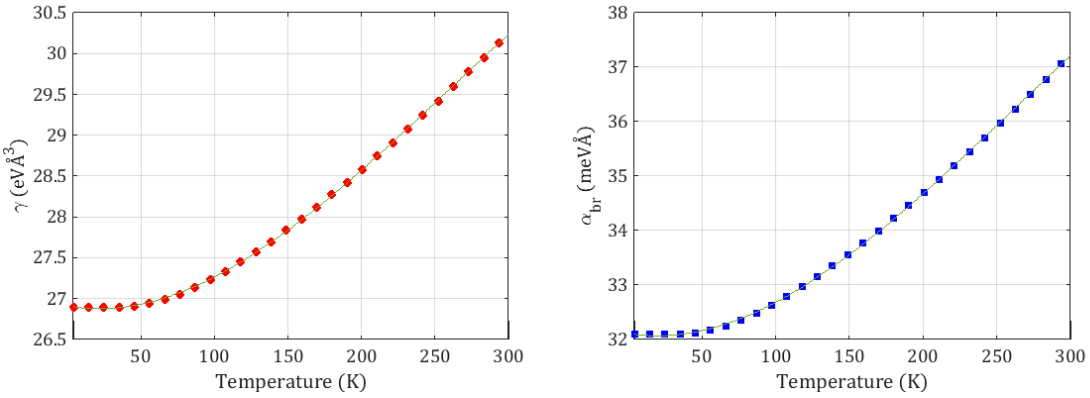

(a) Dresselhaus coupling

(b) Rashba coupling

Figure 42: Temperature dependence of Dresselhaus (γ) and Rashba (α_{br}) coefficients between 4 and 300 K. The Rashba coefficient was estimated using an average electric field of $4.219 \times 10^7\,\mathrm{V\,m^{-1}}$ corresponding to $V_G = 0.7\,\mathrm{V}, V_D = 0.5\,\mathrm{V}$. The dark green lines are cubic fits to the data.

Figure 43 shows the total magnetization against position in the device channel using

S_x, S_y and S_z injection for various lattice temperatures between 85 K and 300 K. For all three injection cases, we see as expected a higher rate spin of decay as the electrons move across the device due too the increased scattering rates and SOC coefficients. We also see a large decrease in the recovery at the drain edge with decreasing temperature, with all three injection directions losing approximately 13.1% of the total magnetisation over the temperature range considered.

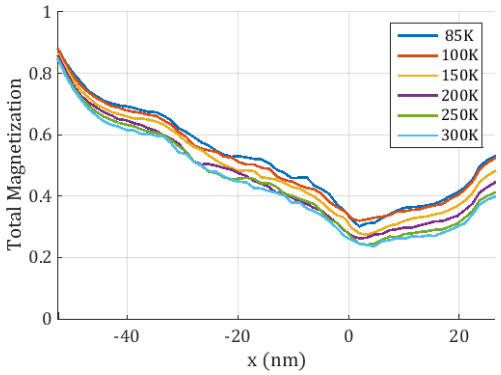

(a) S_x injection

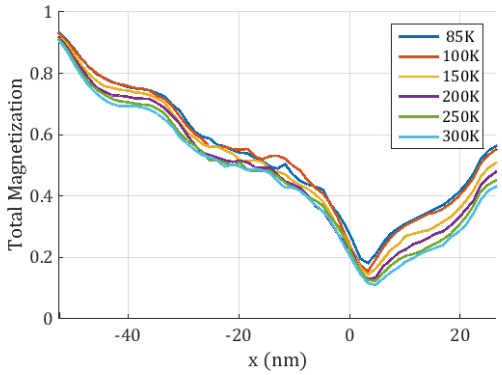

(b) S_y injection

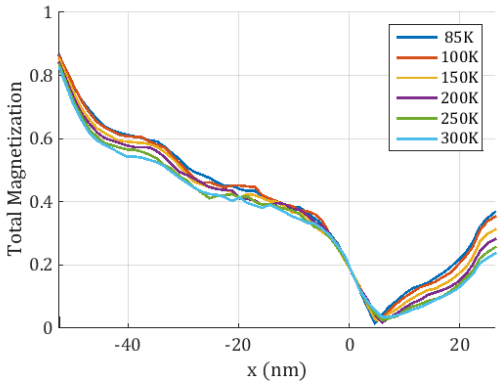

(c) S_z injection

Figure 43: Total magnetization versus position along the channel after steady-state has been reached for temperatures of 85 K to 300 K with $V_G = 0.7$ V and $V_D = 0.5$ V.

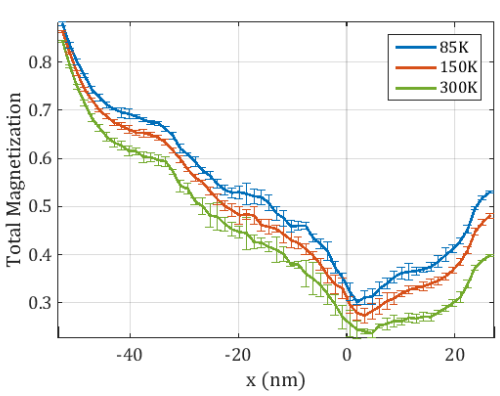

(a) S_x injection

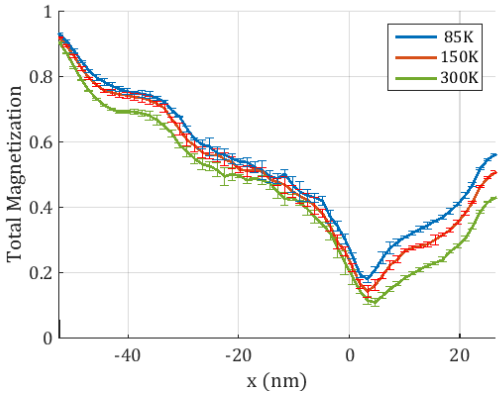

(b) S_y injection

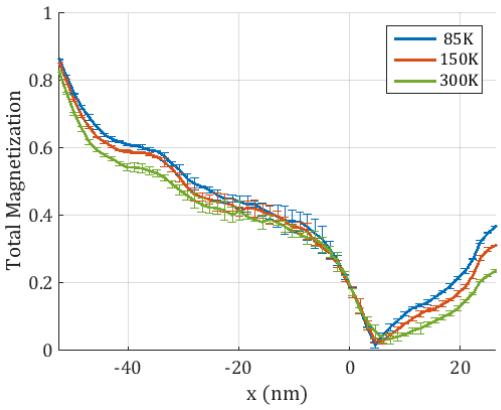

(c) S_z injection

Figure 44: Total magnetization versus position along the channel for T= 85, 150 and 300 K with $V_G = 0.7\,\mathrm{V}$ and $V_D = 0.5\,\mathrm{V}$. The error bars indicate the standard deviation over 10 simulation runs.

Figure 44 shows the total magnetization against position in the device channel for 85, 150 and 300 K once again we see that the standard deviation is generally quite low (indicating low dispersion from the mean) but rises in the centre of the channel due to the lower number of electrons in that region of the device.

Figure 45a shows the magnetisation at the drain for all three injection cases. From this, we can see the decrease appears linear and has a similar gradient for all three cases. This indicates that the change in scattering rate (which is the same for all three cases) may have more of an impact on the magnetization recovery than the change in the spin-orbit coupling strength, given that due to the nature of the Hamiltonian the effects of α_{br} and γ on Bloch

vector $\boldsymbol{S}$ depend upon the injection direction, and therefore one would expect to see a change with temperature that is different for each injection case.

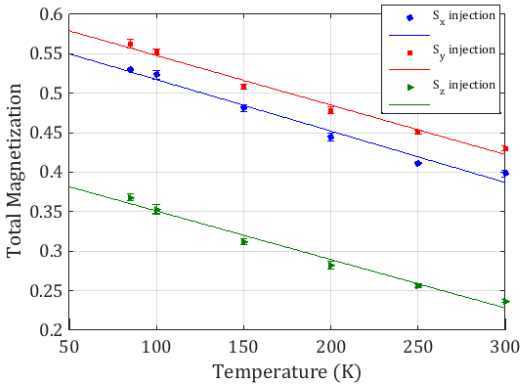

(a) Total Magnetization

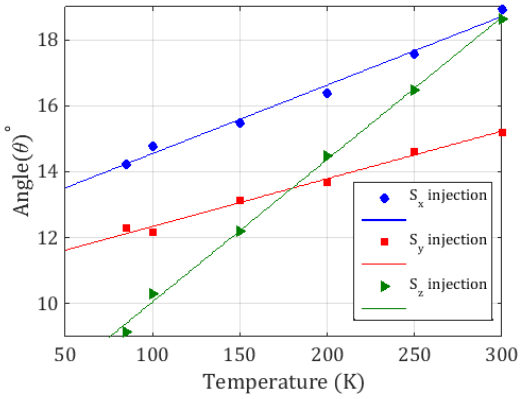

(b) Azimuthal angle

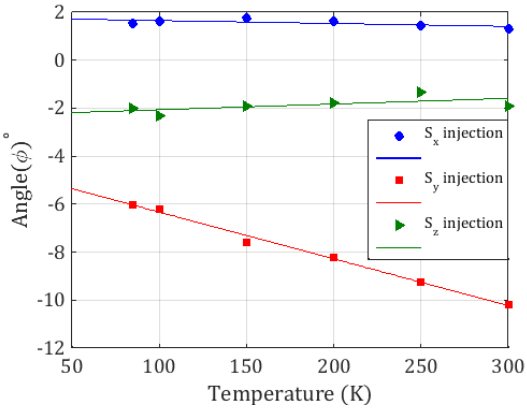

(c) Elevation angle

Figure 45: Steady state magnetisation showing total magnetisation (a), and azimuthal (b) and elevation angle (c) at drain as a function of temperature for $V_G = 0.7V$ and $V_D = 0.5V$ with linear regression fits to show trends in the data.

For all three injection cases we also a linear increase in the azimuth angle (θ) the change appears largest for S_z injection showing increased rotation in the $Z - Y$ plane from 9.14° at 85 K to 18.64° at 300 K, with the S_x and S_y cases showing much smaller increases of $14.22 - 18.92°$ and $12.29 - 15.23°$ respectively. The elevation angle ϕ however, behaves differently. For the S_y case we see a linear decrease from -6.03 to $-10.22°$ (a rotation into the $X - Y$ plane in the $+Z$ direction) whereas S_x and S_z show almost no change with temperature, hovering around 1.5° and $-1.99°$ respectively. Fitting parameters and adjusted

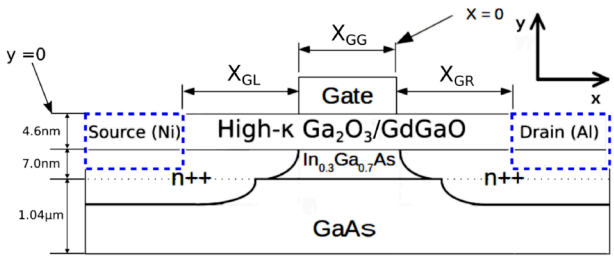

Figure 46: Cross section of the n-channel $In_{0.3}Ga_{0.7}As$ MOSFET. For each case the lengths X_{GG}, X_{GL} and X_{GR} were varied between 25 and 45 nm whilst the remaining two lengths were kept at 25 nm.

R^2 values for all the interpolation lines are once again given in Table 6 Appendix B.

7 Device Dimensions

The final aspect of our investigations into the $In_{0.3}Ga_{0.7}As$ MOSFET was the effect of the channel and gate length on the spin dynamics. The logic behind this was simple. By increasing the length of the channel before or after the gate, we can increase the amount of time the electrons spend travelling through the channel. This has the potential to increase the amount of recovery observed at the drain since the individual spins will have more time to rotate back into alignment. This, however, will only work to a certain extent since increasing the amount of time the electrons spend in the channel will increase the amount of scattering. This means that beyond a certain point we will see a diminishing return as the amount of magnetisation lost due to spin dephasing will outweigh the gains from any recovery effect.

Increasing the gate length may also affect the magnetisation recovery since a more extended gate region would mean the electrons are in the high field underneath the gate for longer and thus experience increased Rashba coupling over a more extended period. Once again, however, there will be a diminishing return as longer gate lengths will mean the electrons spend more time in the channel and thus will experience more random scattering events leading to increased spin dephasing.

Our method for investigating these effects consisted of varying three key lengths in the x-direction: The gate length (X_{GG}), the distance between the source and the gate (X_{GL}) and the distance between the drain and the gate (X_{GR}) (see Figure 46). For each case, the remaining two lengths were kept at 25 nm.

7.1 Gate Length (X_{GG})

Figure 47 shows how the total magnetization across the channel varies with gate length for S_x,S_y and S_z polarized spin injection. For all three cases the shape of the Magnetization decay appears similar although the centre of the curve around the region of the gate is elongated as expected. The Magnetization recovery also appears essentially unchanged with only minor variations which are within the variance between simulation runs.

Figure 48 shows the magnetisation curves for 25, 35 and 45 nm with error bars indicating the standard deviation in the mean over ten simulation runs. From this we can see that the standard deviation is highest in the centre of the channel and lower towards the left and right-hand sides due to the much higher electron densities around the source and drain contacts (see Figure 18c). Overall, however, the standard deviation is relatively small across the channel indicating that the dispersion from the mean is very low.

The magnetisation at the drain is shown Figure 49a. From this we can see that the variation in magnetization between 25 nm and 45 nm is very small with: S_y injection seeing a small linear increase from 47.6% at 25 nm to 49.7% at 45 nm, S_z increasing linearly from 28.4% to 30.3% and S_x remaining at 46.6%.

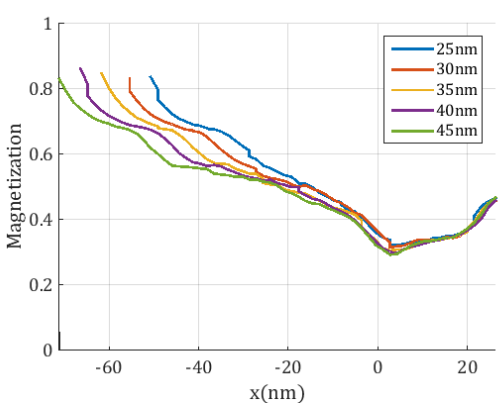

(a) S_x injection

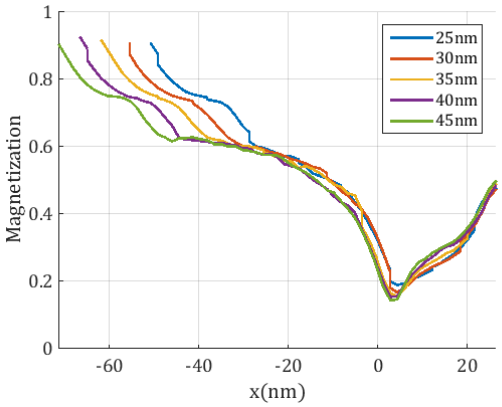

(b) S_y injection

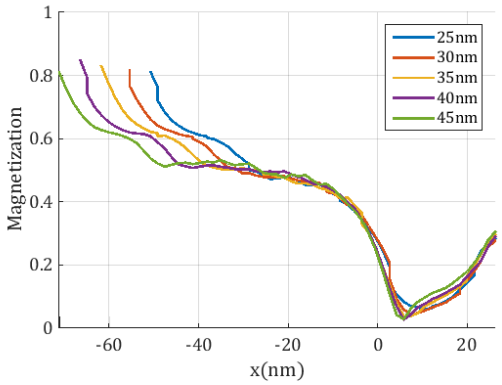

(c) S_z injection

Figure 47: Total magnetization versus position along the channel after steady-state has been reached for gate lengths of 25 nm to 45 nm with $V_G = 0.7\,\mathrm{V}$ and $V_D = 0.5\,\mathrm{V}$.

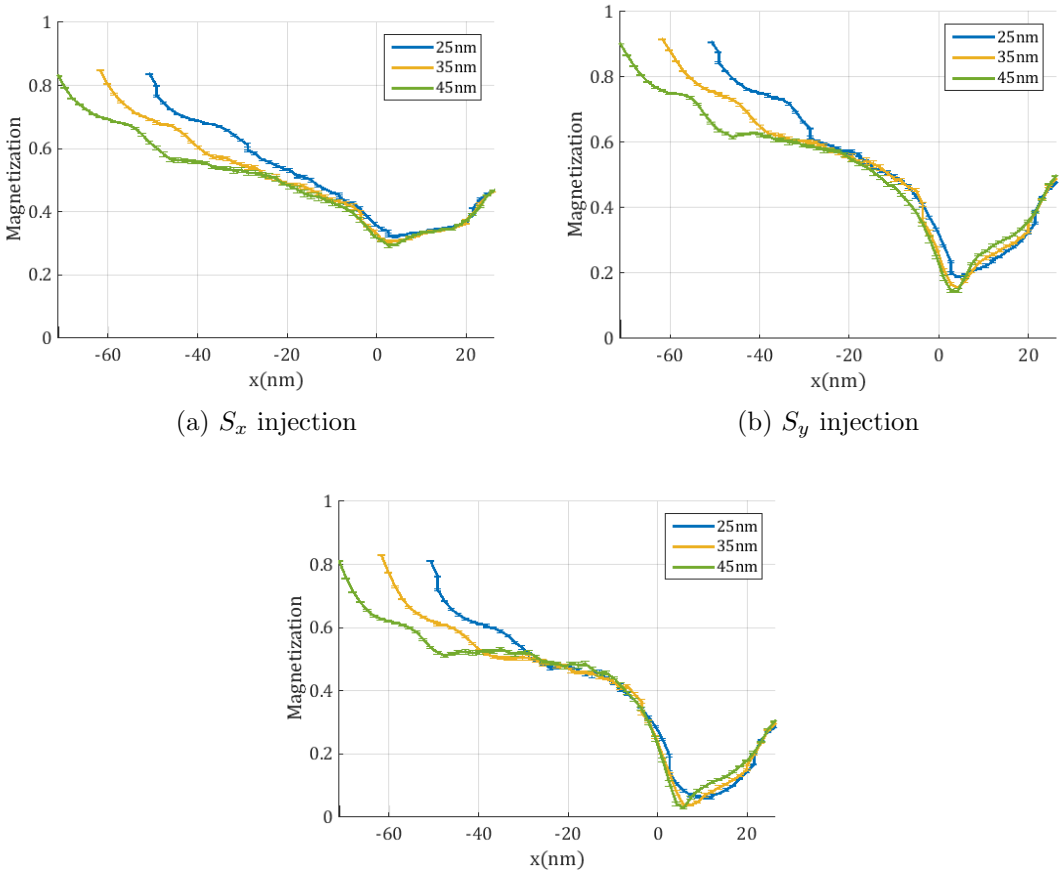

(a) S_x injection

(b) S_y injection

(c) S_z injection

Figure 48: Total magnetization versus position along the channel for $X_{GG} = 25$, 35 and 45 nm after steady-state has been reached with $V_G = 0.7\,\mathrm{V}$ and $V_D = 0.5\,\mathrm{V}$. The error bars show the standard deviation in the mean over 10 simulation runs.

In contrast however, the azimuth and elevation angles for the S_y and S_z cases do show some different behaviour. For S_y the elevation angle ϕ decreases linearly from $-6.08°$ to $-8.69°$ indicating a average decrease in the S_z component due to rotation out of the $X-Y$ plane in the $-Z$ direction. For S_z ϕ increases linearly from $-4.02°$ to $-2.57°$. In this case indicating an increase in the S_x component due to rotation out of the $Z-Y$ plane in the $+X$ direction. The azimuth angle however, only increases for S_z injection going from 9.8° to 14.1°. Fitting parameters and adjusted R^2 values for all the interpolation lines are given in Table 7 Appendix B.

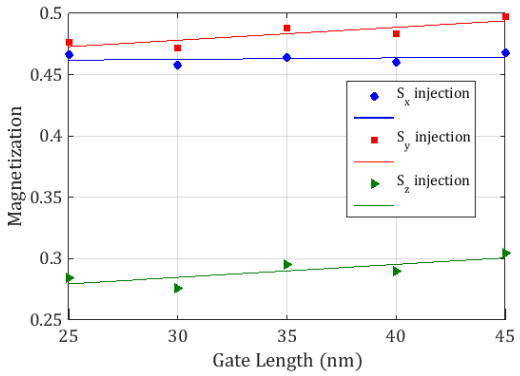

(a) Total Magnetization

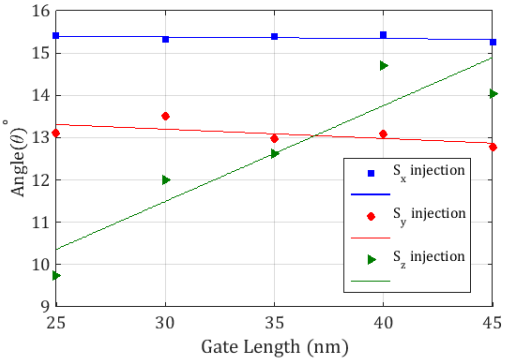

(b) Azimuthal angle

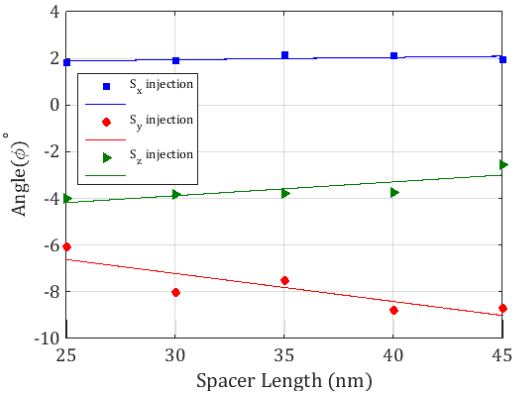

(c) Elevation angle

Figure 49: Steady state magnetization showing total magnetization (a), and azimuthal (b) and elevation angle (c) at drain as a function of gate length for $V_G = 0.7\,\mathrm{V}$ and $V_D = 0.5\,\mathrm{V}$ with linear regression fits to show trends in the data.

Figure 50 shows how the electric field and Rashba co-efficient α_{br} vary across the device channel. As expected the Electric field (and hence the strength of α_{br}) spreads out and reaches a higher maximum with increasing gate length. These two factors lead to an increase in the average Rashba coupling shown in Figure 51 which appears to fit well with a quadratic interpolation (magenta line) with an adjusted R^2 of 0.911.

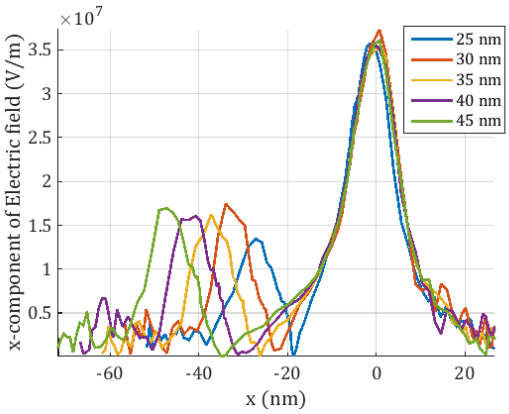

(a) x-component of electric field across the channel

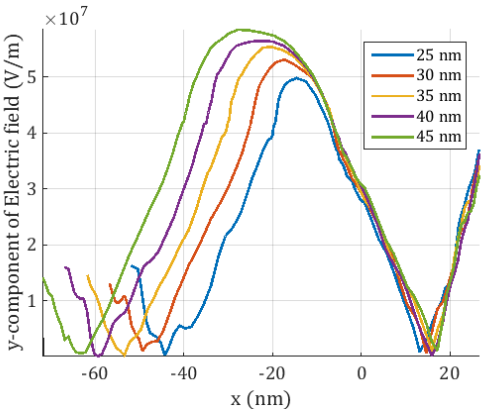

(b) y-component of electric field across the channel

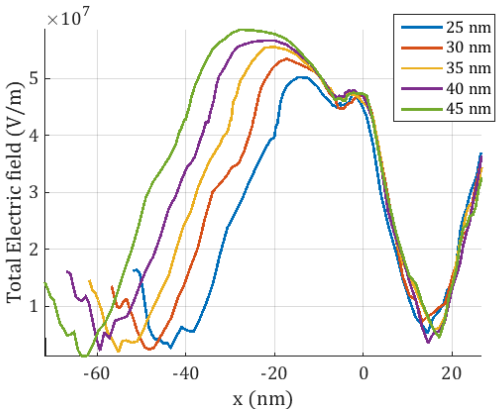

(c) Total electric field across the channel

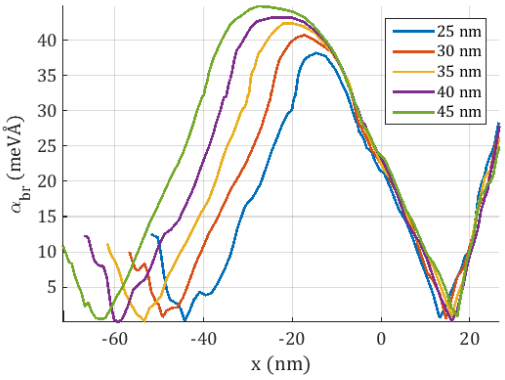

(d) Rashba Coefficient across the channel

Figure 50: Electric field and Rashba coefficient α_{br} versus position along the channel for Gate Lengths of 25 nm to 45 nm with $V_G = 0.7\,\mathrm{V}$ and $V_D = 0.5\,\mathrm{V}$.

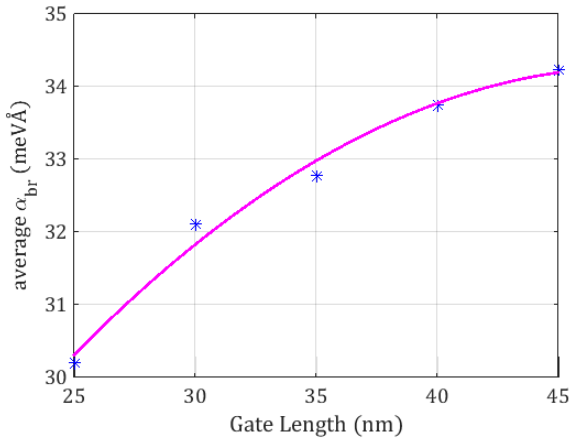

Figure 51: Average α_{br} in the region underneath the gate with increasing gate length the magenta line represents a quadratic interpolation.

Finally, Figure 52 shows the average velocity of the electrons in the x-direction with the position in the channel. As before we see two main asymmetric regions of acceleration corresponding to the two peaks in the x-component of the electric field at the left and right edges of the gate contact (see Figure 50a). As expected the distance between the acceleration peaks increases with increasing gate length, however, the maximum velocity decreases.

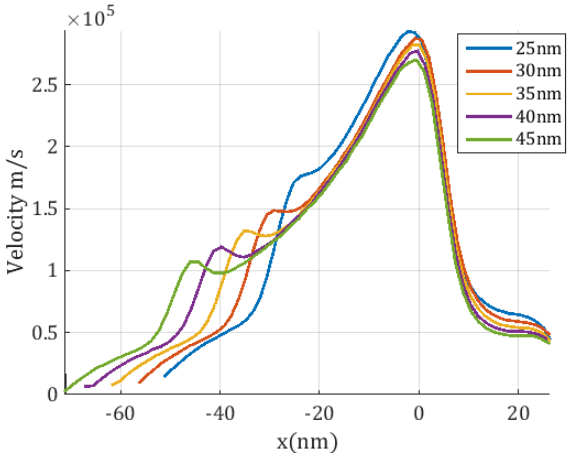

Figure 52: Average velocity of the electrons in the x direction with position in the channel for gate lengths of 25 nm to 45 nm. For $V_G = 0.7V$ and $V_D = 0.5V$

7.2 Left Spacer Length (X_{GL})

Figure 53 shows how the total magnetisation varies across the device channel for three different injection directions. From this, we can see that the amount of decay slightly increases in the region between the source and the gate with increasing X_{GL} for all three injection cases. This is not unexpected since the electrons are spending more time in the channel and thus experiencing more scattering events which will lead to increased spin dephasing. We also see the magnetisation at the drain edge increase with X_{GL} for all three injection cases. Figure 54 shows three curves for 25,35 and 45 nm (chosen to aid visual clarity) with error-bars representing the standard deviation in the mean over 10 simulation runs. Like in all previous cases the standard deviation is minimal in the regions of the source and drain indicating a low dispersion from the mean in these regions. However, the standard deviation increases as we move through the centre of the channel due to the lower electron concentration in this region during the time slice (see Figure 18c).

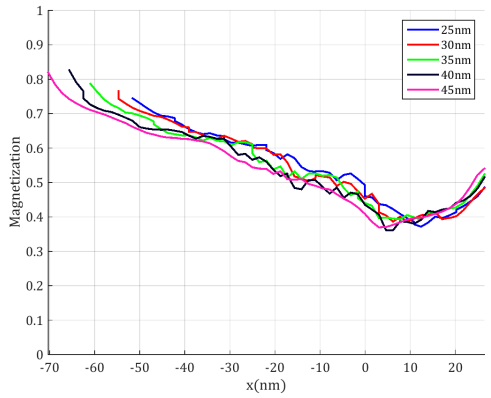

(a) S_x injection

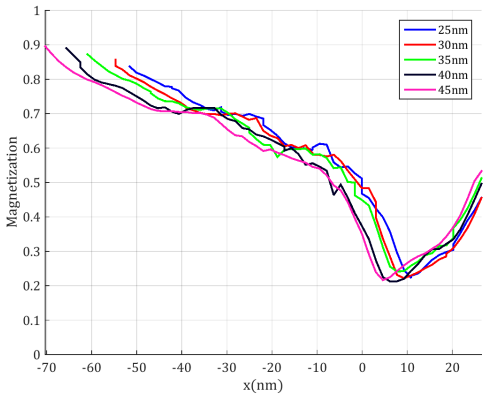

(b) S_y injection

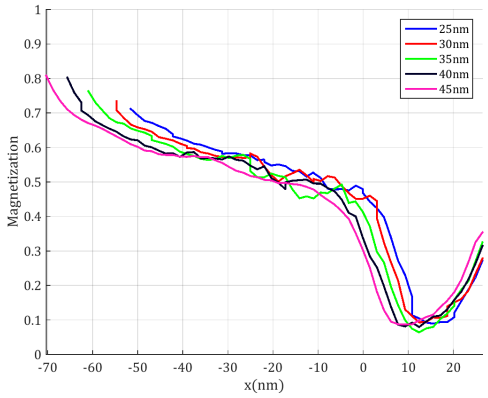

(c) S_z injection

Figure 53: Total magnetization versus position along the channel after steady-state has been reached for X_{GL} between 25 nm to 45 nm with $V_G = 0.7\,\mathrm{V}$ and $V_D = 0.5\,\mathrm{V}$.

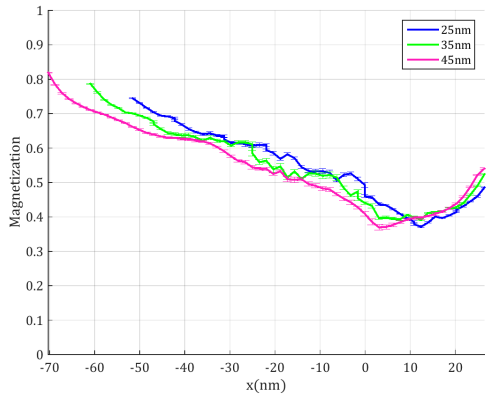

(a) S_x injection

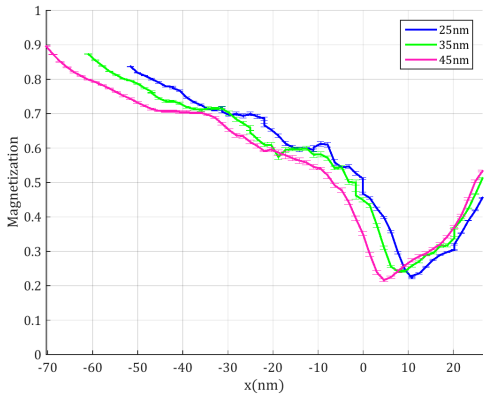

(b) S_y injection

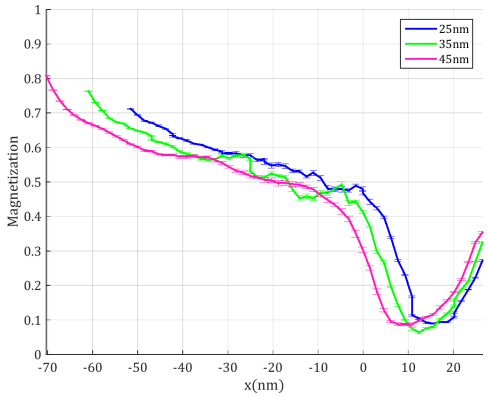

(c) S_z injection

Figure 54: Total magnetization versus position along the channel for select values of X_{GL} after steady-state has been reached with $V_G = 0.7\,\mathrm{V}$ and $V_D = 0.5\,\mathrm{V}$. The error bars indicate the standard deviation over 10 simulation runs.

Figure 55a shows the magnetisation at the drain. For all three injection cases, we see an increase in Magnetisation with X_{GL} which fit nicely with linear regression. The S_x and S_z cases increase from 46.6% to 54.1% and 28.5% to 35.4% respectively with the same gradient of 0.0036. The S_y injection meanwhile increases from 47.7% to 53.3% with a slightingly lower gradient of 0.0027.

The Azimuthal(θ) and elevation (ϕ) at the drain are shown in Figures 55b and 55c. For θ we see a linear decrease with increasing X_{GL} for all three injection cases with: S_x going from 15.41° to 12.57° (rotation from Y to X), S_y going from 13.11° to 11.12° (rotation from X to Y) and S_z going from 9.74° to 8.17° (rotation from Y to Z). ϕ however, shows no

significant change with increasing X_{GL} with: S_x staying at around 2°, S_y at around $-5.8°$ and S_z at around $-4°$.

The individual adjusted R^2 values and parameters used for the fitted lines in Figure 54 are given in Table 8 in Appendix B.

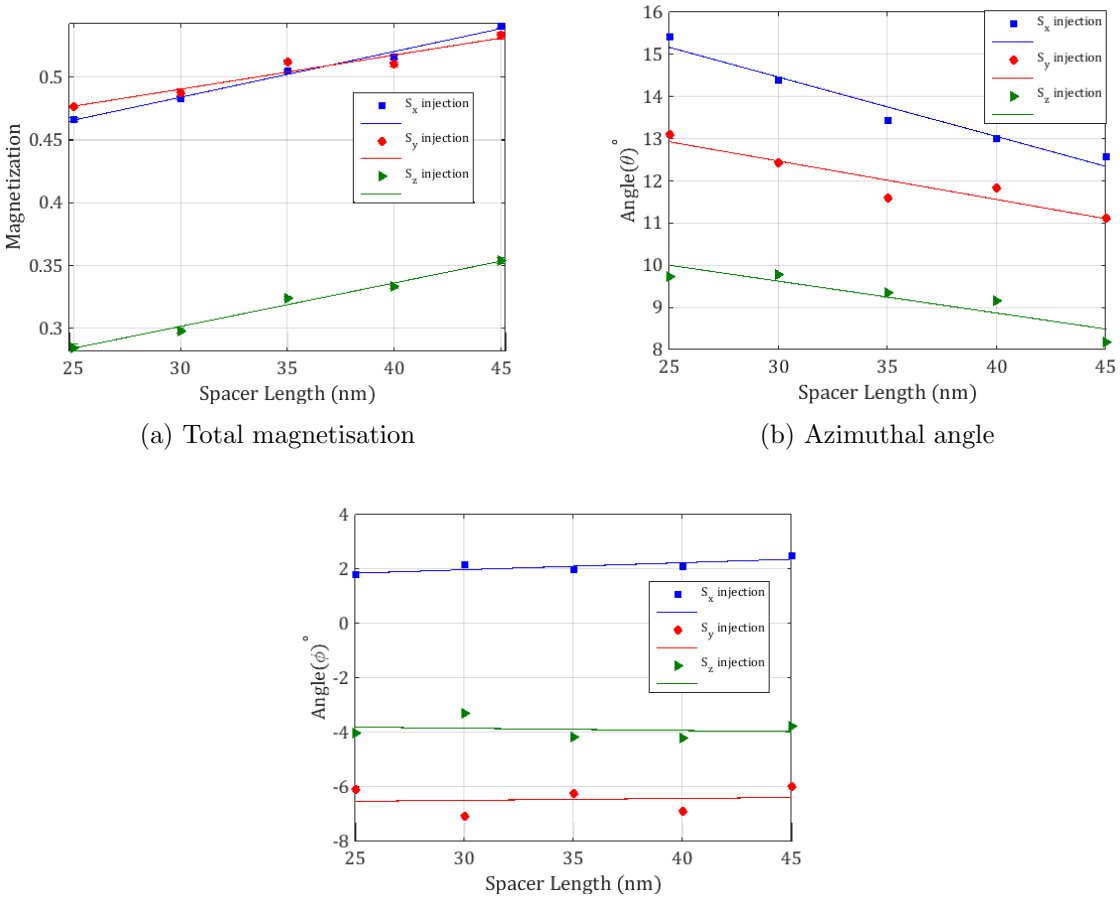

(a) Total magnetisation

(b) Azimuthal angle

(c) Elevation angle

Figure 55: Steady state magnetisation showing total magnetisation (a), and azimuthal (b) and elevation angle (c) at drain as a function of X_{GL} for $V_G = 0.7V$ and $V_D = 0.5V$ with linear regression fits to show trends in the data.

Finally, Figure 56 shows a plot of the average x-velocity of the electrons against the position in the channel. Once again we see two main regions of acceleration corresponding to the two peaks in the x-component of the electric field at the left and right-hand sides of the gate contact. The maximum velocity at the right-hand edge of the gate ($x = 0$) increases with increasing X_{GL}. This is because the electrons will accelerate faster in the

shorter distance between the source and the gate and as a result, will gain kinetic energy more quickly. However, this will cause increased phonon emission which will cause the electrons to lose kinetic energy resulting in a reduction in the maximum velocity.

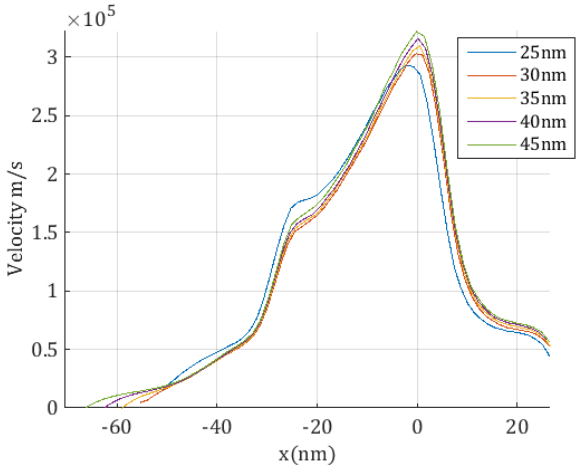

Figure 56: Average velocity of the electrons in the x direction with position in the channel for left spacer lengths (X_{GL}) of 25 nm to 45 nm with $V_G = 0.7\,\text{V}$ and $V_D = 0.5\,\text{V}$.

7.3 Right Spacer Length (X_{GR})

Figure 57 shows how the total magnetisation across the device varies with right spacer length (X_{GR}) for three different injection directions. As expected we initially see similar amounts of decay as the electrons move from the source ($x = -42\,\text{nm}$) towards the left-hand side of the gate ($x = -26\,\text{nm}$). For all three injection cases, however, we see a decreased amount of decay as the electrons travel across the gate followed by an increased amount of recovery at the drain with increasing X_{GR}. Figure 58 shows three selected curves (once again chosen to aid visual clarity) representing the 25, 35 and 45 nm spacer lengths with the corresponding standard deviation in the mean over ten simulation runs. Like in all previous cases the standard deviation is minimal in the regions of the source and drain indicating a low dispersion from the mean in these regions. However, the standard deviation increases as we move through the centre of the channel due to the lower electron concentration in this region during the time slice (see Figure 18c).

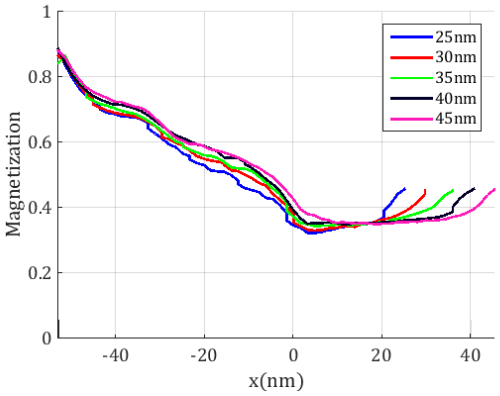

(a) S_x injection

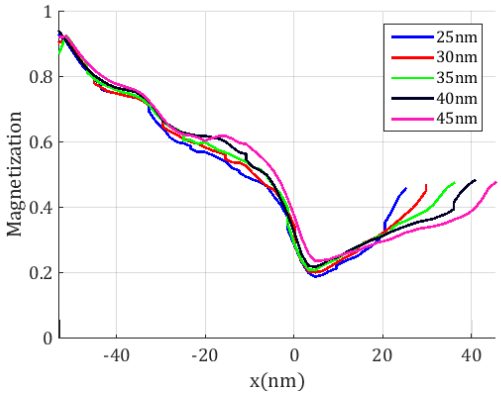

(b) S_y injection

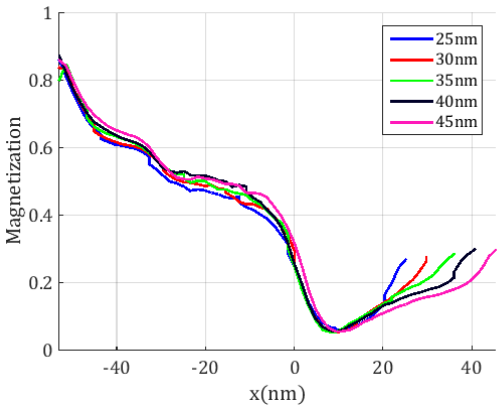

(c) S_z injection

Figure 57: Total magnetization versus position along the channel after steady-state has been reached for X_{GR} between 25 nm to 45 nm with $V_G = 0.7\,\mathrm{V}$ and $V_D = 0.5\,\mathrm{V}$.

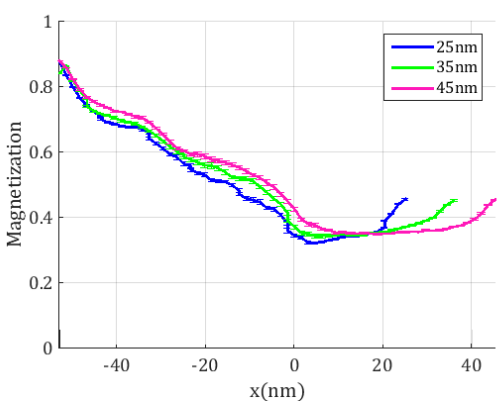

(a) S_x injection

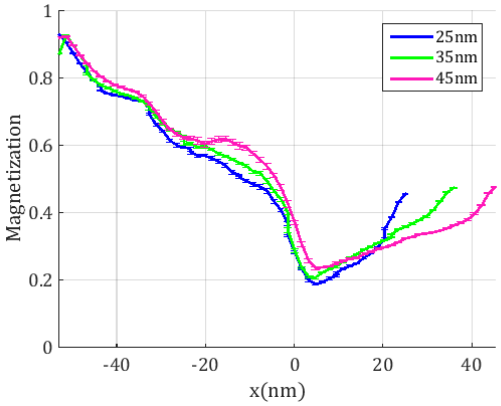

(b) S_y injection

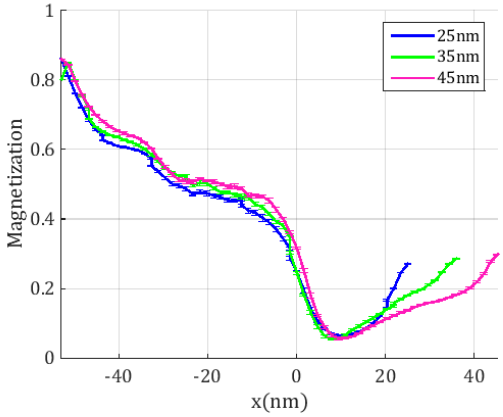

(c) S_z injection

Figure 58: Total magnetization versus position along the channel for select values of X_{GR} after steady-state has been reached with $V_G = 0.7\,\mathrm{V}$ and $V_D = 0.5\,\mathrm{V}$. The error bars indicate the standard deviation over 10 simulation runs.

Figure 59a shows the magnetisation at the drain edge for each injection case. For the case of S_x-injection, we see virtually no increase with increasing X_{GR}, with the magnetisation hovering around 45.5%. We do, however, see small linear increases for both the S_y and S_z, from 45.7% to 47.7% and 26.9% to 29.8%.

Figures 59b and 59c show the azimuth and elevation angles at the drain. For θ we see virtually no change for S_x injection with the value staying around 16°. S_y injection shows a small linear decrease from 13.79° to 12.29° (indicating rotation from X to Y) while the S_z injection shows a linear increase from 11.26° to 13.72° (indicating rotation from Z to Y).

ϕ shows a small linear increase for all three injection cases from 1.99° to 3.76° for S_x

(rotation out of the $X-Y$ plane in the $+Z$ direction), $-7.28°$ to $-5.87°$ for S_y (rotation into the $Y-X$ plane in the $+Z$ direction) and $-4.41°$ to $-2.28°$ for S_z(rotation into the $Z-Y$ plane in the $+X$ direction). Fitting parameters and adjusted R^2 values for all the interpolation lines used in Figure 59 are given in Table 9 Appendix B.

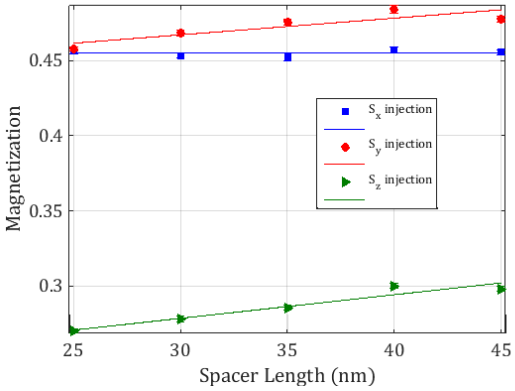

(a) Total Magnetization

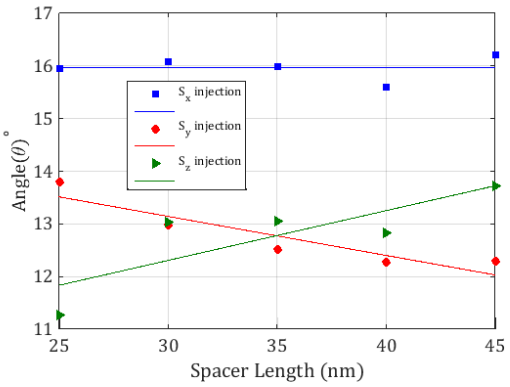

(b) Azimuthal angle

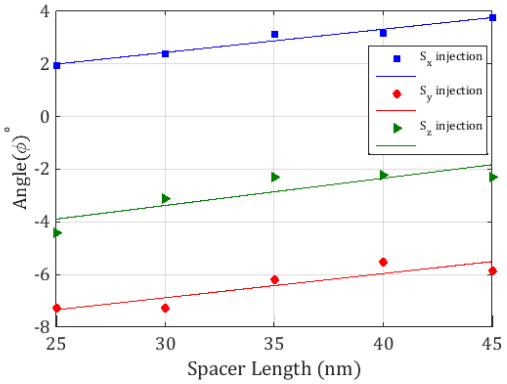

(c) Elevation angle

Figure 59: Steady state magnetization showing total magnetization (a), and azimuthal (b) and elevation angle (c) at drain as a function of X_{GR} for $V_G = 0.7V$ and $V_D = 0.5V$ with linear regression fits to show trends in the data.

Finally, Figure 60 shows a plot of the average x-velocity of the electrons against the position in the channel. Much like the previous cases we see two main regions of acceleration corresponding to the two peaks in the x-component of the electric field at the edges of the gate. The final velocity at the drain, however, is more complex to explain. This velocity is highest for 25 nm and decreases for 30 nm but then slightly increases for 35, 40 and 45 nm.

This effect due to the acceleration of the electrons as they approach the drain. Initially,

the electrons decelerate due to scattering, the rate of which increases with increasing X_{GR}. They then begin to accelerate as they approach the drain. However, because the electrons will accelerate faster when the distance between the gate and drain is shorter, they will gain kinetic energy more quickly. As a consequence, however, the rate of phonon emission will increase causing the electrons to lose kinetic energy resulting in a reduced the maximum velocity. This effect is not noticeable in the 25 and 30 nm cases since the initial deceleration rate was lower and therefore the electrons had a higher velocity when they began to accelerate and thus a higher velocity at the drain edge.

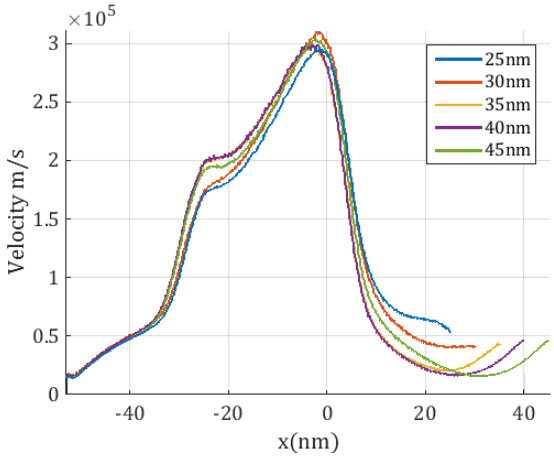

Figure 60: Average velocity of the electrons in the x direction with position in the channel for right spacer lengths (X_{GR}) of 25 nm to 45 nm with $V_G = 0.7\,\text{V}$ and $V_D = 0.5\,\text{V}$.

8 Conclusion

Our ensemble Monte Carlo device simulations of electron spin transport through a realistic 25 nm gate length $In_{0.3}Ga_{0.7}As$ MOSFET show that the total magnetization and its orientation, represented by the length and direction of the Bloch vector associated with the spin degrees of freedom can be controlled via the applied gate bias (and to a lesser extent the source-drain bias). With higher applied gate voltages leading to increased magnetisation decay and a stronger coherent rotation of the Bloch vector from its initial state.

Previous work in this area has been based on micron-sized devices [17, 18, 19, 20, 16]. Although the range of observed rotation angles is much lower when compared to these devices, we can still see significant magnetisation dependent modulations in the drain current which are potentially observable at room temperature. Furthermore, we have observed an unreported recovery of the magnetisation in the region between the gate and drain contacts. This effect appears to be a spin-refocusing effect (similar to that which occurs in nuclear magnetic resonance) caused by the high field in the region underneath the gate. If observed experimentally, this effect could be exploited by future devices to mitigate some of the loses in magnetization over long distances due to decay.

Our investigations into the effects of mechanical strain show that the amount of applied mechanical strain does influence the spin transport. Increasing the amount of strain leads to a decrease in the magnetisation decay across the channel, with the amount being dependent upon the direction in which the strain is applied. We also observe a coherent rotation in the magnetisation vector due to spin-orbit coupling. In this case, the azimuthal rotation angle exhibits a non-linear increase with strain for all strain directions.

We next studied the effect of the lattice temperature. As expected we saw a decrease in the magnetisation decay across the device channel as a result of both the reduced rate of electron scattering and the reduced strength of the Dresselhaus and Rashba coefficients. We also saw an increase in the magnetisation at the drain edge, with decreasing temperature which was constant regardless of the injection direction.

However, our work was limited, this time due to technical issues caused by an as yet unresolved bug in the Fermi-Dirac integral solver which prevented reliable device simulations below 85 K. These problems, however, are much less of a concern since information in the literature on how the bandstructure changes with temperature for many semiconductors is still lacking (most notably in our case InAs). Thus our ability to make accurate predictions

at these temperatures is limited.

Finally we investigated the impact of channel length on the spin, Specifically varying the length of the gate region X_{GG}, the distance between the source contact and the gate X_{GL} and the distance between the gate and drain contact X_{GR}.

Varying the gate length showed as expected an increased rate of decay in the region of the gate but only a small dependence for the magnetisation recovery at the drain edge in the S_y and S_z injection cases, with no change seen for the S_x injection.

The rotation angles also show a similar story with S_y and S_z injection cases indicating a small net rotation from z to y and the S_x injection showing no significant net rotation.

Changing the length of the left spacer led to a slightly increased magnetisation decay across the device channel, with the effect being more significant for the S_y and S_z injection cases. All three injection cases also showed a linear increase in the magnetisation at the drain and a linear decrease in the azimuthal angle θ.

Changing the length of the right spacer showed no significant changes to the decay across the device and only small increases to the magnetisation at the drain for the S_y and S_z injection cases.

Overall our simulation results for changing the channel lengths are somewhat unexpected and confusing. Given we would expect to see a decay in the magnetisation at the drain edge, in particular for the gate length due to the increased area within the high Electric field. However, our results seem to show the length has little to no effect. These types of simulation, however, a quite complex (in particular the various scattering mechanisms that are incorporated). Thus more work will be needed to gather more data and understand the precise mechanisms at play.

In conclusion, we have augmented an advanced 2D, finite element, Monte Carlo simulation of a 25 nm gate length $In_{0.3}Ga_{0.7}As$ MOSFET. We observe a significant and previously unreported magnetisation recovery in the region of the channel between the gate and drain. We demonstrated the potential to control the spin degrees of freedom via the applied gate bias (and to a lesser extent the source-drain bias) and showed how the magnetisation decay (and recovery) varies with lattice temperature, compressive strain and channel length.

Future work could potentially look into the role of spin-injection and detection which were absent from this work since we did not wish to limit the scope of the simulation results

by considering specific injection and detection mechanisms. However, in practice, these issues play an essential role. In particular, the possibility of room temperature operation will depend on whether we can achieve sufficiently high injection and detection efficiencies to measure the predicted changes, which may be challenging if these changes are small.

One could also look into different transistor architectures (e.g. HEMT's) or materials with alternative spin properties such as Si, in which the spin-orbit coupling is much weaker such that the Elliott-Yafet mechanism is the dominant form of spin relaxation at room temperature. Si is also a material that has seen much attention for spintronics in recent years [82] due to its extensive use in conventional semiconductor technology making it an attractive option for future commercial applications. Alternatively, one could look into GaN which has higher mobility, a higher density of states and lower spin-orbit interaction when compared to GaAs and is predicted to have a spin lifetime that is about three orders of magnitude longer than GaAs [83].

Another exciting avenue would be investigating single spins trapped in quantum dots and the potential to measure control the precise spin-state of such electrons to gain a greater understanding of the core physics involved. There is also the potential to continue the work on the low-temperature dependence by investigating the effects of ultra-low temperatures (less than 4 K) a regime very different to room temperature in which could lead to some exciting new physics.

References

[1] S. Datta and B. Das, "Electronic analog of the electro-optic modulator," *Applied Physics Letters*, vol. 56, no. 7, pp. 665–667, 1990.

[2] S. Sugahara and M. Tanaka, "A spin metal–oxide–semiconductor field-effect transistor using half-metallic-ferromagnet contacts for the source and drain," *Aplied Physics Letters*, vol. 84, no. 13, pp. 2307–2309, 2004.

[3] W. Y. Choi, H. Kim, J. Chang, S. H. Han, H. C. Koo, and M. Johnson, "Electrical detection of coherent spin precession using the ballistic intrinsic spin hall effect," *Nat Nano*, vol. 10, no. 8, pp. 666–670, 2015.

[4] S. Bandyopadhyay and M. Cahay, "Alternate spintronic analog of the electro-optic modulator," *Applied Physics Letters*, vol. 85, no. 10, p. 1814, 2004.

[5] J. Wunderlich, A. C. Irvine, and J. Sinova, "Spin-injection hall effect in a planar photovoltaic cell," *Nature Physics*, vol. 5, p. 675, 2009.

[6] J. Wunderlich, B. Park, A. C. Irvine, L. P. Zarbo, E. Rozkotova, P. Nemec, V. Novak, J. Sinova, and T. Jungwirth, "Spin hall effect transistor," *Science*, vol. 330, p. 1801, 2010.

[7] K. Kalna, N. Seoane, A. J. García-Loureiro, I. G. Thayne, and A. Asenov, "Benchmarking of scaled InGaAs implant-free nanoMOSFETs," *IEEE Trans. Electron Devices*, vol. 55, pp. 2297–2306, September 2008.

[8] J. Fabian and A. Matos-Abiague, "Semiconductor spintronics," *acta physica slovaca*, vol. 57, no. 4 & 5, pp. 565–907, 2007.

[9] J. M. Jancu and R. Schlotz, "Atomistic spin-orbit coupling and $\boldsymbol{k} \cdot \boldsymbol{p}$ parameters in III − V semiconductors," *Physical Review B*, vol. 72, p. 193201, 2005.

[10] S. Bandyopadhyay and M. Cahay, *Introduction to spintronics*. Taylor and Francis Group, CRC Press, 2008.

[11] R. P. Feynman, R. B. Leighton, and M. Sands, *The Feynman lectures on physics: Vol. 3, Quantum mechannics.* Addison-Wesley, 1965.

[12] L. D. Landau and E. M. Lifshitz, *Quantum mechanics : non-relativistic theory*. Oxford : Pergamon, 1965.

[13] J. Schliemann, J. C. Egues, and D. Loss, "Nonballistic spin-field-effect transistor," *Physical Review Letters*, vol. 90, p. 146801, Apr 2003.

[14] N. Seoane, M. Aldegunde, D. Nagy, M. A. Elmessary, G. Indalecio, A. J. García-Loureiro, and K. Kalna, "Simulation study of scaled $In_{0.53}Ga_{0.47}As$ and Si FinFETs for sub-16 nm technology nodes," *Semiconductor Science and Technology*, vol. 31, no. 7, p. 075005, 2016.

[15] B. Thorpe, K. Kalna, F. Langbein, and S. Schirmer, "Monte carlo simulations of spin transport in a strained nanoscale InGaAs field effect transistor," *Journal of Applied Physics*, vol. 122, p. 223903, 2018.

[16] M. Shen, S. Saikin, M.-C. Cheng, and V. Privman, "Monte Carlo modeling of spinFETs controlled by spin–orbit interaction," *Mathematics and Computers in Simulation*, vol. 65, pp. 351–363, 2004.

[17] A. Bournel, P. Dollfus, P. Bruno, and P. Hesto, "Gate-induced spin precession in an ingaas two dimensional electron gas," *Eur. Phys. J. AP*, vol. 4, pp. 1–4, 1998.

[18] A. Bournel, P. Dollfus, S. Galdin, F. Musalem, and P. Hesto, "Modelling of gate-induced spin precession in a striped channel high electron mobility transistor," *Solid State Communications*, vol. 104, no. 2, pp. 85–89, 1997.

[19] A. Bournel, P. Dollfus, E. Cassan, and P. Hesto, "Monte carlo study of spin relaxation in algaas/gaas quantum wells," *Applied Physics Letters*, vol. 77, p. 2346, 2000.

[20] A. Bournel, V. Delmouly, P. Dollfus, G. Tremblay, and P. Hesto, "Theoretical and experimental considerations on the spin field effect transistor," *Physica E*, vol. 10, pp. 86–90, 2001.

[21] S. Bandyopadhyay and M. Cahay, "Reexamination of some spintronic field-effect device concepts," *Applied Physics Letters*, vol. 85, no. 8, pp. 1433–1435, 2004.

[22] R. Landauer, "Spatial variation of currents and fields due to localized scatterers in metallic conduction," *IBM Journal of Research and Development*, vol. 1, no. 3, pp. 223–231, 1957.

[23] X. Cartoixa, Y. Ting, and Y. Chang, "A resonant spin lifetime transistor," *Applied Physics Letters*, vol. 83, no. 7, pp. 1462–1464, 2003.

[24] E. Shafir, M. Shen, and S. Saikin, "Modulation of spin dynamics in a channel of a nonballistic spin field effect transistor," *Physical Review B*, vol. 70, p. 241302, 2004.

[25] E. H. Hall, "On a new action of the magnet on electric currents," *American Journal of Mathematics*, vol. 2, p. 287, 1879.

[26] L. Berger and G. Bergmann, *The Hall Effect and Its Applications*, ch. The Hall Effect of Ferromagnets., pp. 55–76. Springer, Boston, MA, 1980.

[27] J. E. Hirsch, "Spin hall effect," *Physical Review Letters*, vol. 83, no. 9, p. 1834, 1999.

[28] Y. K. Kato, R. C. Myers, A. C. Gossard, and D. D. Awschalom, "Observation of the spin hall effect in semiconductors," *Science*, vol. 306, no. 5703, pp. 1910–1913, 2004.

[29] J. Wunderlich, B. Kaestner, J. Sinova, and T. Jungwirth, "Experimental observation of the spin-hall effect in a two-dimensional spin-orbit coupled semiconductor system," *Physical Review Letters*, vol. 94, p. 047204, 2005.

[30] D. McMahon, *Quantum Computing Explained*. Wiley-IEEE Press, 2008.

[31] K. Hannabuss, *An Introduction to Quantum Theory*. Oxford University Press, 2004.

[32] H.-P. Breuer and F. Petruccione, *The Theory of Open Quantum Systems*. Oxford University Press, 2002.

[33] F. Schwabl, *Statistical Mechanics*. Springer Science & Business Media, 2002.

[34] H. J. W. George B. Arfken and F. E. Harris, *Mathematical Methods for physicists: A Comprehensive guide*. Elsevier Academic press, 2013.

[35] F. Bloch, "Nuclear induction," *Phys Rev*, vol. 70, no. 7, p. 460, 1946.

[36] J. J. Sakurai, *Advanced Quantum Mechanics*. Addison-Wesley, 1963.

[37] A. Davydov, *Quantum Mechanics*. Pergamon Press, 1976.

[38] J. D. Jackson, *Classical Electrodynamics*. Willey, 3rd ed., 1998.

[39] L. H. Thomas, "The motion of the spining electron," *Nature*, vol. 117, p. 514, 1926.

[40] P. F. Weller, *Solid State Chemistry and Physics*. Marcel Dekker Inc. , New York, 1973.

[41] J. Fabian and S. D. Sarma, "Spin relaxation in conduction electrons," *J. Vac. Sci. Technol. B*, vol. 17, no. 4, 1999.

[42] R. J. Elliott, "Theory of the effect of spin-orbit coupling on magnetic resonance in some semiconductors," *Physical Review*, vol. 96, no. 2, p. 266, 1954.

[43] J. L. Cheng, M. W. Wu, and J. Fabian, "Theory of the spin relaxation of conduction electrons in silicon," *Physical Review Letters*, vol. 104, p. 016601, 2010.

[44] A. W. Overhauser, "Paramagnetic relaxation in metals," *Physical Review*, vol. 89, no. 4, p. 689, 1953.

[45] Y. Yafet, "g factors and spin-lattice relaxation of conduction electrons," in *Solid State Physics* (F. Seitz and D. Turnbull, eds.), vol. 14, pp. 1–98, Academic, New York, 1963.

[46] P. Monod and F. Beuneu, "Conduction-electron spin flip by phonons in metals: Analysis of experimental data," *Physical Review B*, vol. 19, no. 2, p. 911, 1979.

[47] M. I. D'yakonov and V. I. Perel, "Spin orientation of electrons associated with the interband absorption of light in semiconductors," *Soviet Physics JETP*, 1971.

[48] G. L. Bir, A. G. Aronov, and G. E. Pikus, "Spin relaxation of electrons due to scattering by holes," *Sov. Phys. JETP*, vol. 42, no. 4, p. 705, 1975.

[49] G. E. Pikus and A. N. Titkov, "Optical orientation," in *Modern Problems in Condensed Matter Science,* (F. Meier and B. P. Zakharchenya, eds.), vol. 8, p. 73, North-Holland, Amsterdam, 1984.

[50] G. Bastard, *Wave Mechanics Applied to Semiconductor Heterostructures.* Les editions de physique, 1998.

[51] C. Kittel, *Introduction to Solid State Physics.* John Willey and Sons Inc., 8 ed., 2005.

[52] E. O. Kane, "Band structure of indium antimonide," *J. Phys. Chem. Solids*, vol. 1, pp. 249–261, January 1957.

[53] R. Winkler, *Spin–Orbit Coupling Effects in Two-Dimensional Electron and Hole Systems.* Springer Berlin, 2003.

[54] P. Pfeffer and W. Zawadzki, "Five-level $\boldsymbol{k} \cdot \boldsymbol{p}$ model for the conduction and valence bands of GaAs and InP," *Physical review B*, vol. 53, no. 19, p. 12813, 1996.

[55] J. M. Luttinger and W. Kohn, "Motion of electrons and holes in perturbed periodic fields," *Physical Review*, vol. 97, no. 4, p. 869, 1955.

[56] J. M. Luttinger, "Quantum theory of cyclotron resonance in semiconductors: General theory," *Physical Review*, vol. 102, no. 4, p. 1030, 1956.

[57] S. L. Chuang, *Physics of Optoelectronic Devices*. John Wiley & Sons Inc., 1995.

[58] I. Vurgaftman, J. R. Meyer, , and L. R. Ram-Mohan, "Band parameters for III–V compound semiconductors and their alloys," *Journal of Applied Physics*, vol. 89, no. 11, p. 5815, 2001.

[59] G. Bastard, "Superlattice band structure in the envelope-function approximation," *Physical Review B*, vol. 24, no. 10, p. 5693, 1981.

[60] R. S. Calsaverini, E. Bernardes, J. C. Egues, and D. Loss, "Intersubband-induced spin-orbit interaction in quantum wells," *Physical Review B*, vol. 78, p. 155313, 2008.

[61] C. Jacoboni and P. Lugli, *The Monte Carlo Method for Semiconductor Device Simulation*. Springer-Verlag Wien New York, 1989.

[62] K. Tomizawa, *Numerical Simulation of Submicron Semiconductor Devices*. Artech House Inc., 1993.

[63] B. K. Ridley, *Quantum Processes in Semiconductors*. Oxford: London, 1982.

[64] J. W. Harrison and J. R. Hauser, "Alloy scattering in ternary $\mathrm{III}-\mathrm{V}$ compounds," *Physical Review B*, vol. 13, no. 12, p. 5347, 1976.

[65] J. R. Hauser, M. A. Littlejohn, and T. H. Glisson, "Velocity-field relationship of inas-inp alloys including the effects of alloy scattering," *Applied Physics Letters*, vol. 28, p. 458, April 1976.

[66] A. Valavanis, Z. Ikonic, and R. W. Kelsall, "Intersubband carrier scattering in $\mathrm{n}-$ and $\mathrm{p}-\mathrm{Si/SiGe}$ quantum wells with diffuse interfaces," *Physical Review B*, vol. 77, p. 075312, 2008.

[67] H. Sakaki, T. Noda, K. Hirakawa, M. Tanaka, and T. Matsusue, "Interface roughness scattering in GaAs/AlAs quantum wells," *Applied Physics Letters*, vol. 51, p. 1934, 1987.

[68] M. Newman, *Computational Physics*. CreateSpace Independent Publishing Platform, 2012.

[69] I. Žutić and S. D. Sarma, "Spintronics: Fundamentals and applications," *Reviews of Modern Physics*, vol. 76, p. 323, 2004.

[70] A. Islam, B. Benbakhti, and K. Kalna, "Monte carlo study of ultimate channel scaling in Si and $In_{0.3}Ga_{0.7}As$ bulk MOSFETs," *IEEE Trans. Nanotechnology*, vol. 10, pp. 1424–1432, November 2011.

[71] K. Kalna, S. Roy, A. Asenov, K. Elgaid, and I. Thayne, "Scaling of pseudomorphic high electron mobility transistors to decanano dimensions," *Solid-St. Electron.*, vol. 46, no. 5, pp. 331–338, 2002.

[72] D. A. J. Moran, K. Kalna, E. Boyd, F. McEwan, H. McLelland, L. Zhuang, C. R. Stanley, A. Asenov, and I. Thayne, "Self-aligned 0.12 μm t-gate $In_{0.53}Ga_{0.47}As/In_{0.52}Ga_{0.48}As$ HEMT technology utilising a non-annealed ohmic contact strategy," in *Proc. 29th ESSDERC*, pp. 315–318, 2003.

[73] K. Kalna, K. Elgaid, I. Thayne, and A. Asenov, "Modelling of InP HEMTs with high indium content channels," in *Proc. 17th Indium Phosphide Related Materials*, pp. 61–65, 2005.

[74] S. Krivec, M. Poljak, and T. Suligojand, "Band-structure of ultra-thin ingaas channels: Impact of biaxial strain and thickness scaling," in *Proc. 40th Int. Convention on Information and Communication Technology*, pp. 66–71, 2017.

[75] T. B. Bahder, "Eight-band $\boldsymbol{k}\cdot\boldsymbol{p}$ model of strained zinc-blende crystals," *Physical Review B*, vol. 41, p. 11992, 1990.

[76] W. Wang and J. Fu, "Temperature dependence of the rashba and dresselhaus spin–orbit interactions in GaAs wells," *Physica B: Condensed Matter*, vol. 482, pp. 14–18, 2016.

[77] J. Hubner, S. Dohrmann, D. Hagele, and M. Oestreich, "Temperature dependent electron landé g-factor and interband matrix element in GaAs," *Phys.Rev. B*, vol. 79, p. 193307, 2009.

[78] P. Lautenschlager, M. Garriga, S. Logothetidis, and M. Cardona, "Interband critical points of GaAs and their temperature dependence," *Phys. Rev. B*, vol. 35, no. 17, p. 9174, 1987.

[79] T. J. Kim, S. Y. Hwang, J. S. Byun, N. S.Barange, J. Y. Kim, and Y. D. Kim, "Temperature dependence of the dielectric function and critical-point energies of InAs," *Journal of the Korean Physical Society*, vol. 61, no. 1, pp. 97–101, 2012.

[80] R. Passler, "Temperature dependence of fundamental band gaps in group IV, III–V, and II–VI materials via a two-oscillator model," *Journal of Applied Physics*, vol. 89, no. 11, p. 6235, 2001.

[81] T. J. Kim, S. Y. Hwang, J. Byun, M. S. Diware, J. Y. Kim, and Y. D. Kim, "Parametric model dielectric functions of InAs for temperatures from 22 to 675 k," *Journal of the Korean Physical Society, V*, vol. 61, no. 11, p. 1821, 2012.

[82] V. Sverdlov and S. Selberherr, "Silicon spintronics: Progress and challenges," *Physics Reports*, vol. 585, pp. 1–40, 2015.

[83] S. Krishnamurthy, M. van Schilfgaarde, and N. Newman, "Spin lifetimes of electrons injected into GaAs and GaN," *Applied Physics Letters*, vol. 83, no. 9, p. 1761, 2003.

Appendices

A 8×8 and 14×14 Kane Hamiltonians

This appendix contains the explicit forms of the matrix blocks used to create the $H_{8\times8}$ and $H_{14\times14}$ bulk matrix Hamiltonians used in the Kane and extended Kane models discussed in sections 3.1 and 3.2 of the main text. Where $H_{8\times8}$ and $H_{14\times14}$ are defined as

$$H_{8\times8} = \begin{pmatrix} H_c & H_{cv} \\ H_{vc} & H_v \end{pmatrix} \qquad H_{14\times14} = \begin{pmatrix} H_c & H_{cv} & H_{cc'} \\ H_{vc} & H_v & H_{vc'} \\ H_{c'c} & H_{c'v} & H_{c'} \end{pmatrix}$$

with:

$$H_c = \begin{pmatrix} \frac{\hbar^2k^2}{2m_0} & 0 \\ 0 & \frac{\hbar^2k^2}{2m_0} \end{pmatrix}, \qquad H_{vc} = \frac{1}{\sqrt{6}} \begin{pmatrix} -\sqrt{3}Pk_- & 0 \\ -2iPk_z & -Pk_- \\ Pk_+ & -2iPk_z \\ 0 & \sqrt{3}Pk_+ \\ i\sqrt{2}Pk_z & -\sqrt{2}Pk_- \\ -\sqrt{2}Pk_+ & -i\sqrt{2}Pk_z \end{pmatrix},$$

$$H_{cv} = \begin{pmatrix} -\frac{1}{\sqrt{2}}Pk_+ & -i\sqrt{\frac{2}{3}}Pk_z & \frac{1}{\sqrt{6}}Pk_- & 0 & -\frac{i}{\sqrt{3}}Pk_z & -\frac{1}{\sqrt{3}}Pk_- \\ 0 & -\frac{1}{\sqrt{6}}Pk_+ & -i\sqrt{\frac{2}{3}}Pk_z & \frac{1}{\sqrt{2}}Pk_- & -\frac{1}{\sqrt{3}}Pk_+ & \frac{i}{\sqrt{3}}Pk_z \end{pmatrix},$$

$$H_v = \begin{pmatrix} \frac{\hbar^2k^2}{2m_0} - E_0 & 0 & 0 & 0 & 0 & 0 \\ 0 & \frac{\hbar^2k^2}{2m_0} - E_0 & 0 & 0 & 0 & 0 \\ 0 & 0 & \frac{\hbar^2k^2}{2m_0} - E_0 & 0 & 0 & 0 \\ 0 & 0 & 0 & \frac{\hbar^2k^2}{2m_0} - E_0 & 0 & 0 \\ 0 & 0 & 0 & 0 & \frac{\hbar^2k^2}{2m_0} - E_0 - \Delta_0 & 0 \\ 0 & 0 & 0 & 0 & 0 & \frac{\hbar^2k^2}{2m_0} - E_0 - \Delta_0 \end{pmatrix},$$

$$H_{cc'} = \begin{pmatrix} -\frac{i}{\sqrt{2}}P_1 k_+ & i\sqrt{\frac{2}{3}}P_1 k_z & \frac{i}{\sqrt{6}}P_1 k_- & 0 & -\frac{i}{\sqrt{3}}P_1 k_z & -\frac{i}{\sqrt{3}}P_1 k_- \\ 0 & -\frac{i}{\sqrt{6}}P_1 k_+ & i\sqrt{\frac{2}{3}}P_1 k_z & \frac{i}{\sqrt{2}}P_1 k_- & -\frac{i}{\sqrt{3}}P_1 k_+ & \frac{i}{\sqrt{3}}P_1 k_z \end{pmatrix},$$

$$H'_c = \begin{pmatrix} \frac{\hbar^2 k^2}{2m_0} + E_1 + \Delta_1 & 0 & 0 & 0 & 0 & 0 \\ 0 & \frac{\hbar^2 k^2}{2m_0} + E_1 + \Delta_1 & 0 & 0 & 0 & 0 \\ 0 & 0 & \frac{\hbar^2 k^2}{2m_0} + E_1 + \Delta_1 & 0 & 0 & 0 \\ 0 & 0 & 0 & \frac{\hbar^2 k^2}{2m_0} + E_1 + \Delta_1 & 0 & 0 \\ 0 & 0 & 0 & 0 & \frac{\hbar^2 k^2}{2m_0} + E_1 & 0 \\ 0 & 0 & 0 & 0 & 0 & \frac{\hbar^2 k^2}{2m_0} + E_1 \end{pmatrix},$$

$$H_{vc'} = \begin{pmatrix} \frac{i}{3}\Delta^- & \frac{i}{\sqrt{3}}Qk_+ & \frac{i}{\sqrt{3}}Qk_z & 0 & -\frac{i}{\sqrt{6}}Qk_+ & -i\sqrt{\frac{2}{3}}Qk_z \\ -\frac{i}{\sqrt{3}}Qk_- & \frac{i}{3}\Delta^- & 0 & \frac{i}{\sqrt{3}}Qk_z & 0 & \frac{i}{\sqrt{2}}Qk_+ \\ -\frac{i}{\sqrt{3}}Qk_z & 0 & \frac{i}{3}\Delta^- & -\frac{i}{\sqrt{3}}Qk_+ & -\frac{i}{\sqrt{2}}Qk_- & 0 \\ 0 & -\frac{i}{\sqrt{3}}Qk_z & \frac{i}{\sqrt{3}}Qk_- & \frac{i}{3}\Delta_- & -i\sqrt{\frac{2}{3}}Qk_z & \frac{i}{\sqrt{6}}Qk_- \\ \frac{i}{\sqrt{6}}Qk_- & 0 & \frac{i}{\sqrt{2}}Qk_+ & i\sqrt{\frac{2}{3}}Qk_z & -\frac{2i}{3}\Delta^- & 0 \\ i\sqrt{\frac{2}{3}}Qk_z & -\frac{i}{\sqrt{2}}Qk_- & 0 & -\frac{i}{\sqrt{6}}Qk_+ & 0 & -\frac{2i}{3}\Delta^- \end{pmatrix}$$

and $k_\pm = k_x \pm ik_y$.

The Kane parameters P, P_1, Q and Δ^- are defined in sections 3.1 and 3.2 whilst the Energies E_0, E_1, Δ_0 and Δ_1 are defined in table 1 of section 3.2. Finally $H_{c'c}$ and $H_{c'v}$ are obtained by the transposition of $H_{cc'}$ and $H_{vc'}$, respectively, with the following substitutions: $k_\pm \to k_\mp$, $P_1 \to -P_1$, $Q \to -Q$ and $\Delta^- \to -\Delta^-$

B Fitting Parameters for "drain edge" plots

This appendix contains the fitting parameters for the plots of the polar angles (θ and ϕ) and the Total Magnetisation ($|S|$) at the left hand side of the drain contact. These plots were used throughout chapter 5 and cover the effects of varying: The gate voltage (V_G), source-drain voltage (V_D), lattice temperature (T), the Gate length (X_{GG}) and the Left/right spacer lengths (X_{GL} and X_{GR}). All the parameters were obtained using the `Matlab` curve fitting tool box.

B.1 Gate Voltage (V_G)

	Injection	P_1	P_2	R^2	Adjusted R^2
$\|S\|$	S_x	-0.4349 (-0.06122, -0.02576)	0.3834 (0.3707, 0.396)	0.9531	0.9375
	S_y	-0.09915 (-0.1179, -0.08042)	0.4274 (0.4141, 0.4408)	0.9895	0.9861
	S_z	-0.1137 (-0.1315, -0.096)	0.2762 (0.2635, 0.2888)	0.9928	0.9905
θ	S_x	26.15 (16.58, 35.72)	-1.047 (-7.882, 5.788)	0.9618	0.9491
	S_y	22.04 (15.68, 28.41)	-0.152 (-4.696, 4.392)	0.9759	0.9679
	S_z	-7.723 (-13.75, -1.698)	29.55 (25.24, 33.85)	0.8473	0.7963
ϕ	S_x	2.977 (1.499, 4.456)	-1.791 (-2.847, -0.7355)	0.9319	0.9092
	S_y	5.062 (1.506, 8.618)	-17.98 (-20.52, -15.45)	0.8725	0.8299
	S_z	-11.56 (-20.16, -2.952)	6.303 (0.1575, 12.45)	0.8589	0.8119

Table 4: Fitting parameters for figure 29 from Chapter 5, containing plots of the Total Magnetisation ($|S|$) and polar angles (θ and ϕ) at the left hand side of the drain contact against applied Gate Voltage (V_G). All the curves are fit to a linear polynomial model with $y = P_1x + P_2$. The values in brackets are the 95% confidence bounds for the specified parameter.

B.2 Source-Drain Voltage (V_D)

	Injection	P_1	P_2	R^2	Adjusted R^2
$\|S\|$	S_x	-0.1449 (-0.1703, -0.1195)	0.4748 (0.4567, 0.4929)	0.991	0.988
	S_y	-0.1252 (-0.1525, -0.09783)	0.4536 (0.4341, 0.4731)	0.9861	0.9814
	S_z	-0.04425 (-0.08532, -0.003176)	0.212 (0.1816, 0.2424)	0.9148	0.8723
θ	S_x	-5.512 (-10.41, -0.6124)	27.16 (23.66, 30.66)	0.8103	0.7471
	S_y	-4.361 (-6.046, -2.675)	23.82 (22.62, 25.02)	0.9576	0.9435
	S_z	-	-	-	-
ϕ	S_x	-6.496 (-9.329, -3.664)	6.758 (4.735, 8.78)	0.9467	0.9289
	S_y	-8.152 (-15.24, -1.063)	-5.665 (-10.73, -0.603)	0.817	0.756
	S_z	5.569 (-23.49, 34.63)	-9.201 (-28.91, 10.51)	0.8577	0.7113

Table 5: Fitting parameters for figure 34 from Chapter 5, containing plots of the Total Magnetisation ($|S|$) and polar angles (θ and ϕ) at the left hand side of the drain contact against applied Source-Drain Voltage (V_D). The curves are fit to a linear polynomial model with $y = P_1x + P_2$. The values in brackets are the 95% confidence bounds for the specified parameter. It should be noted that the S_z values for θ did not fit to a polynomial curve and a cubic spline fit was used instead, thus these values have been excluded from this table.

B.3 Lattice Temperature

	Injection	P_1	P_2	R^2	Adjusted R^2
$\|S\|$	S_x	-0.0006517 (-0.0007819, -0.0005216)	0.5826 (0.557, 0.6082)	0.9797	0.9747
	S_y	-0.0006269 (-0.0007354, -0.0005184)	0.6106 (0.5892, 0.6319)	0.9847	0.9809
	S_z	-0.0006144 (-0.0007355, -0.0004933)	0.4124 (0.3886, 0.4363)	0.9802	0.9753
θ	S_x	0.02079 (0.01763, 0.02395)	12.47 (11.85, 13.09)	0.9881	0.9852
	S_y	0.01445 (0.01233, 0.01657)	10.9 (10.48, 11.32)	0.9889	0.9862
	S_z	0.04315 (0.04026, 0.04604)	5.74 (5.171, 6.308)	0.9977	0.9971
ϕ	S_x	-0.001839 (-0.004099, 0.0004208)	1.924 (1.445, 2.403)	0.691	0.588
	S_y	-0.01947 (-0.02173, -0.0172)	-4.385 (-4.831, -3.938)	0.993	0.9912
	S_z	0.003897 (-0.001934, 0.009727)	-2.42 (-3.48, -1.36)	0.8053	0.7079

Table 6: Fitting parameters for figure 45 from Chapter 5, containing plots of the Total Magnetisation ($|S|$) and polar angles (θ and ϕ) at the left hand side of the drain contact against Lattice Temperature. The curves are fit to a linear polynomial model with $y = P_1 x + P_2$. The values in brackets are the 95% confidence bounds for the specified parameter.

B.4 Gate Length (X_{GG})

	Injection	P_1	P_2	R^2	Adjusted R^2
$\|S\|$	S_x	0.0001215 (-0.0008518, 0.001095)	0.4588 (0.4241, 0.4936)	0.04998	-0.2667
	S_y	0.001049 (-0.0001846, 0.002282)	0.4466 (0.4026, 0.4907)	0.7094	0.6125
	S_z	0.001059 (-0.0005044, 0.002623)	0.253 (0.1971, 0.3088)	0.6077	0.477
θ	S_x	-0.007367 (-0.05275, 0.03802)	15.61 (13.98, 17.24)	0.8097	0.194
	S_y	-0.01301 (-0.04872, 0.02269)	13.46 (12.14, 14.78)	0.5515	0.3273
	S_z	0.2266 (0.05173, 0.4014)	4.694 (-1.549, 10.94)	0.8501	0.8001
ϕ	S_x	0.01029 (-0.01831, 0.0389)	1.63 (0.6087, 2.651)	0.8718	0.7435
	S_y	-0.1424 (-0.2654, -0.01938)	-2.606 (-7.157, 1.945)	0.9254	0.8881
	S_z	0.07222 (-0.008551, 0.153)	-5.984 (-8.775, -3.193)	0.881	0.8214

Table 7: Fitting parameters for figure 29 from Chapter 5, containing plots of the Total Magnetisation ($|S|$) and polar angles (θ and ϕ) at the left hand side of the drain contact against Gate Length (X_{GG}). The curves are fit to a linear polynomial model with $y = P_1x + P_2$. The values in brackets are the 95% confidence bounds for the specified parameter.

B.5 Left Spacer Length (X_{GL})

	Injection	P_1	P_2	R^2	Adjusted R^2
$\|S\|$	S_x	0.003642 (0.002985, 0.0043)	0.3747 (0.3512, 0.3981)	0.9904	0.9873
	S_y	0.002716 (0.00139, 0.004041)	0.4089 (0.3616, 0.4562)	0.9341	0.9121
	S_z	0.003465 (0.002639, 0.004291)	0.1977 (0.1682, 0.2272)	0.9834	0.9779
θ	S_x	-0.1411 (-0.1967, -0.08548)	18.69 (16.71, 20.68)	0.956	0.9414
	S_y	-0.09117 (-0.1542, -0.02814)	15.21 (12.95, 17.46)	0.876	0.8346
	S_z	-0.07558 (-0.1386, -0.01259)	11.89 (9.639, 14.14)	0.8294	0.7725
ϕ	S_x	0.0644 (-0.3723, 0.5011)	-8.789 (-25.03, 7.453)	0.7783	0.5566
	S_y	-0.1424 (-0.2654, -0.01938)	-2.606 (-7.157, 1.945)	0.9254	0.8881
	S_z	-0.008257 (-0.0931, 0.07659)	-3.595 (-6.625, -0.5654)	0.03098	-0.292

Table 8: Fitting parameters for figure 55 from Chapter 5, containing plots of the Total Magnetisation ($|S|$) and polar angles (θ and ϕ) at the left hand side of the drain contact against Left Spacer Length (X_{GL}). The curves are fit to a linear polynomial model with $y = P_1 x + P_2$. The values in brackets are the 95% confidence bounds for the specified parameter.

B.6 Right Spacer Length (X_{GR})

	Injection	P_1	P_2	R^2	Adjusted R^2
$\|S\|$	S_x	2.052e-05 (-0.0004561, 0.0004972)	0.4542 (0.4372, 0.4712)	0.006216	-0.325
	S_y	0.001112 (-1.539e-05, 0.00224)	0.4337 (0.3934, 0.4739)	0.7666	0.6888
	S_z	0.00157 (0.0007451, 0.002395)	0.2313 (0.2019, 0.2608)	0.9244	0.8992
θ	S_x	0.01142 (-0.01101, 0.03386)	15.67 (14.9, 16.45)	0.7059	0. 0.5589
	S_y	-0.07413 (-0.1323, -0.01597)	15.37 (13.29, 17.44)	0.8458	0.7944
	S_z	0.09448 (-0.02743, 0.2164)	9.472 (5.119, 13.83)	0.6697	0.5596
ϕ	S_x	0.09169 (0.005842, 0.1775)	-9.632 (-12.7, -6.567)	0.7939	0.7252
	S_y	0.09169 (0.005842, 0.1775)	-9.632 (-12.7, -6.567)	0.7939	0.7252
	S_z	0.1034 (-0.006197, 0.2131)	-6.48 (-10.4, -2.565)	0.7503	0.6671

Table 9: Fitting parameters for figure 59 from Chapter 5, containing plots of the Total Magnetisation ($|S|$) and polar angles (θ and ϕ) at the left hand side of the drain contact against Right Spacer Length (X_{GR}). The curves are fit to a linear polynomial model with $y = P_1x + P_2$. The values in brackets are the 95% confidence bounds for the specified parameter.